FACULDADE DE ENGENHARIA DA UNIVERSIDADE DO PORTO

Effects of Co-Location of FOWTs and WECs on Mooring Cable Fatigue

Margarida José Quintal Santos

Master in Mechanical Engineering: Fluids and Energy

Supervisor: Paulo Avilez-Valente

Second Supervisor: Guilherme Paredes

22 July 2025

Effects of Co-Location of FOWTs and WECs on Mooring Cable Fatigue

Margarida José Quintal Santos

Master in Mechanical Engineering: Fluids and Energy

22 July 2025

“Life is worth living.”

Justin Bieber

Abstract

The co-location of Floating Offshore Wind Turbines (FOWTs) and Wave Energy Converters (WECs) is a promising approach to optimise spatial use and reduce wave-induced loads in the FOWT, potentially reducing fatigue. This dissertation investigates how the co-location of WECs affects the fatigue behaviour of FOWT mooring cables—an essential component for maintaining platform stability under dynamic environmental loads. The main objective is to assess whether co-location can reduce fatigue damage and extend the operational life of mooring lines, and which parameters have more influence.

A comprehensive methodology was employed, beginning with the generation of 30 realistic sea states using ERA5 reanalysis data modelled through a Gaussian copula and Monte Carlo sampling. The wave field was simulated with SWAN to account for the shadowing effects of WECs. WEC-Sim was used to model the dynamic response of the FOWT platform, and MooDy simulated mooring line dynamics. Fatigue analysis was carried out using WAFO, employing rainflow counting and Miner's Rule. A Taguchi Design of Experiments (DoE) approach was applied to investigate the effects of WEC array configuration on fatigue performance.

Results indicate that the presence and configuration of WECs can significantly alter mooring-fatigue response. The optimal configuration achieved a fatigue reduction of 23% in one of the cables. In Cable 1, the cable lifespan was extended by more than three years. The parameters exerting the greatest influence were the number of WECs, the angle of alignment of the WEC array with FOWT, and minimum distance between devices. These findings underscore the importance of array design in enhancing the durability and robustness of co-located offshore renewable-energy systems.

Keywords: Fatigue, Mooring Lines, FOWT, Co-Location, SWAN, WEC-Sim, MooDy, WAFO, DoE.

Resumo

A co-localização de turbinas eólicas flutuantes offshore (FOWTs) e conversores de energia das ondas (WECs) surge como uma abordagem promissora para otimizar a utilização do espaço marítimo e reduzir as cargas induzidas pelas ondas nas FOWTs, com potencial para mitigar a fadiga. Esta dissertação investiga de que forma a co-localização de WECs influencia o comportamento da fadiga dos cabos de amarração das FOWTs — um componente essencial para garantir a estabilidade da plataforma sob condições ambientais dinâmicas. O principal objectivo é avaliar se a co-localização pode reduzir os danos por fadiga e prolongar a vida útil dos cabos de amarração, identificando os parâmetros com maior influência para esse fim.

A metodologia deste estudou começou pela geração de 30 estados de mar, utilizando dados de reanálise ERA5 modelados através de uma função de Cópula Gaussiana e amostragem de Monte Carlo. O campo de ondas foi simulado com o modelo SWAN para considerar o efeito de sombra induzido pelos WECs. A resposta dinâmica da plataforma FOWT foi modelada com o WEC-Sim, enquanto o comportamento dos cabos de amarração foi simulado com o MooDy. A análise de fadiga foi realizada com recurso ao WAFO, recorrendo ao método *Rainflow* e à aplicação da regra de Miner. Foi ainda utilizada uma abordagem baseada no *Design of Experiments* (DoE) de *Taguchi* para investigar o impacto das configurações de WECs no desempenho à fadiga.

Os resultados indicam que a presença e configuração dos WECs podem alterar significativamente a resposta à fadiga dos cabos de amarração. A configuração ótima permitiu uma redução da fadiga de 23% no Cabo 1 e de 13% nos Cabos 2 e 3. No caso do Cabo 1, a vida útil foi prolongada em mais de três anos. Os parâmetros que exerceram maior influência foram um maior número de WECs, melhor alinhamento do conjunto de WECs com FOWT e minimização da distância entre os dispositivos. Estes resultados evidenciam a importância do design do array para melhorar a durabilidade e robustez dos sistemas offshore de energias renováveis em regime de co-localização.

Palavras-chave: Fadiga, Cabos de Amarração, FOWT, Co-Localização, SWAN, WEC-Sim, MooDy, WAFO, DoE.

Acknowledgments

This dissertation would not have been possible without the support and encouragement of many people, to whom I would like to express my deepest gratitude.

First and foremost, I would like to thank my supervisor, Dr. Eng. Paulo Avilez-Valente, and my co-supervisor, Dr. Eng. Guilherme Paredes. Your unwavering guidance, expertise, and constant support throughout this journey have been more than I could have hoped for. I am truly grateful for your patience, insight, and encouragement that helped bring this work to completion.

To my beloved family — Pecas, Cata, Mom, and Dad — thank you. Without even realizing it, you were the reason I had the strength to overcome this challenge. Your unconditional love and belief in me have always been my anchor and my inspiration. You will always be my reason to keep chasing my dreams.

To my friends, from high school through my time at FEUP, thank you for filling my days with joy, laughter, and lightness. Your presence helped ease the stress without needing to say a word. A special thank you to the incredible girls I shared a home with at the residence — may our friendship last a lifetime.

And to my boyfriend — my biggest fan, no matter the subject — thank you for believing in me, especially when I didn't believe in myself. You always knew when I needed a break, taking me everywhere and nowhere just at the right time. Your love and support meant everything.

To all those mentioned above, I wholeheartedly dedicate this thesis.

Margarida Santos

Contents

List of Figures

List of Tables

List of Symbols

a	Fatigue strength coefficient
$A(\omega)$	Added-mass matrix
C	Hydrostatic stiffness matrix
C_e	Energy capture coefficient
Co	Copula matrix
d_i	Rank difference
D	Accumulated fatigue damage
E	Total wave energy per unit surface
F	F-statistics
$F_B(t)$	Buoyancy restoring force
$F_{ex}(t)$	Wave excitation force
$F_{md}(t)$	Mean drift force
$F_m(t)$	Morison element force
$F_{pto}(t)$	Power take-off force
$F_{rad}(t)$	Radiation force
$F_v(t)$	Damping force
f	Wave frequency (linear)
f_{env}	Environmental force
f_p	Peak frequency
g	Gravitational acceleration
H	Wave height
$H_{1/3}$	Observed significant wave height
H_{m0}	Spectral significant wave height
H_s	Significant wave height (generic)
k	Wave number
m	Fatigue exponent
m_{-1}, m_0, m_2	Spectral moments
n	Number of stress cycles experienced
n_{seas}	Number of sea states
N	Number of cycles to failure
$N(\sigma, \theta)$	Wave action density
p	Number of observations
p_j	Probability of occurrence
P	Absorbed wave power
r	Cable position
s	Directional spreading parameter and Lagrangian coordinate
S	Spectral density
S_J	JONSWAP spectral density

S_{PM}	Pierson-Moscowitz spectral density
T	Wave period and Cable internal tension
T_e	Energy period
T_p	Peak wave period
T_z	Mean zero-crossing period
T_{m10}	Mean period based on m_{-1}/m_0
u	Marginal probability
$\mathbf{u}$	Current velocity
x	Horizontal coordinate
$\mathbf{x}(\omega)$	Amplitude of the response
α	Phillips constant
β	Spectral decay constant
ε	Wave phase
η	Sea surface elevation
γ	Peak enhancement factor (JONSWAP spectrum)
λ	Wavelength
ϕ	Velocity potential
ρ	Water density
ρ_s	Spearman correlation coefficient
σ	Stress and realtive angular frequency
σ_θ	Directional spread
θ	Wave direction
θ_0	Mean wave direction
θ_{wind}	Wind direction
κ	Spectral width
ω	Wave angular frequency
Φ^{-1}	Inverse cumulative distribution function of the standard normal distribution
Φ_R	Cumulative distribution function of the multivariate normal distribution

Abbreviations

ALS	Accidental Limit State
ANOVA	Analysis of Variance
BEM	Boundary Element Method
DoE	Design of Experiments
DNV	Det Norske Veritas
EA	Axial Stiffness
ECMWF	European Centre for Medium-Range Weather Forecasts
FLS	Fatigue Limit State
FOWT	Floating Offshore Wind Turbine
LDG	Local Discontinuous Galerkin
LCoE	Levelized Cost of Energy
OC4/OC5	Offshore Code Comparison Collaboration Projects
O&M	Operation and Maintenance
PDF	Probability Density Function
PM	Pierson-Moskowitz (spectrum)
PTO	Power Take-Off
RAO	Response Amplitude Operator
RMS	Root Mean Square
SLS	Serviceability Limit State
S/N	Signal-to-Noise
S-N	Stress-Number of Cycles
SWAN	Simulating WAves Nearshore
TLP	Tension Leg Platform
T-N	Tension-Number of Cycles
ULS	Ultimate Limit State
WAFO	Wave Analysis for Fatigue and Oceanography
WAB	Wave Activated Body
WAMIT	Wave Analysis MIT
WEC	Wave Energy Converter
WEC-Sim	Wave Energy Converter Simulator
WWIII	WaveWatch III

Glossary

Added Mass	Apparent increase in inertia due to displaced water around a moving body.
Bathymetry	Sea floor topography.
Resonance	Amplification of motion when wave frequency matches natural frequency of the structure.

Chapter 1

Introduction

1.1 Background

The accelerating impacts of climate change and the global commitment to decarbonisation have intensified the demand for reliable, low-carbon energy sources. Within the portfolio of renewables, the oceans provide an extensive and largely untapped resource base that combines persistent winds with high-energy waves.

Offshore wind technology has attained commercial maturity. Global installed capacity totalled 75.2GW at the end of 2023—an increase of 24% over the previous year—with China contributing 6.3 GW and thus 71% of the annual additions (Cagatay, 2024; Williams and Zhao, 2024). In Europe, total wind capacity reached 285 GW in 2025, of which 37 GW is deployed offshore (Costanzo et al., 2025). Continued growth is anticipated as developers move farther from shore to exploit stronger and more consistent wind regimes.

Floating offshore wind turbines (FOWTs) extend this reach into deep-water sites where bottom -fixed foundations are not feasible (DNVGL-OS-E301, 2018). Yet FOWTs presently exhibit comparatively high levelised costs of energy (LCoE): in 2025, the LCoE was estimated at 92€/MWh, compared with 60€/MWh for bottom-fixed turbines and approximately 35€/MWh for onshore wind (Fuchs et al., 2024).

A critical factor influencing the economic viability of FOWTs is the cost of the mooring system, which accounts for approximately 5–10% of their total LCoE (Bjørni et al., 2023). A large share of this cost is attributed to operation and maintenance (O&M) activities, especially as mooring cables are subject to fatigue deterioration over time. Reducing the fatigue loads experienced by these cables could therefore significantly lower O&M requirements and extend their service life, resulting in a meaningful reduction in overall LCoE.

One promising strategy to address this challenge is the co-location of FOWTs with Wave Energy Converters (WECs). Co-location refers to deploying both technologies within the same leased ocean space. WECs have been shown to produce a shadowing effect by attenuating incoming wave energy. When placed optimally in front of FOWTs, they can reduce the wave load acting on the floating platform and its mooring lines, thereby decreasing fatigue damage (Perez-Collazo et al., 2014).

Beyond structural benefits, co-location offers broader advantages, including increased spatial efficiency, smoother combined power output, and shared electrical and support infrastructure potential (Ramos et al., 2022). While wave energy remains at an earlier stage of technological maturity, ongoing advancements and pilot deployments have demonstrated the feasibility of several WEC architectures (Ramos et al., 2022). These developments reinforce the relevance of co-located systems in achieving a more integrated, resilient, and cost-effective offshore renewable energy sector.

1.2 Problem Statement

While the benefits of co-location of FOWTs and WECs are increasingly recognised, the impact of the co-location strategy on mooring line fatigue has not been extensively explored. Clark and Paredes (2018) studied the fatigue of mooring lines using one WEC. Due to time limitations, parameters like a wide range of numbers of WECs, different alignments, and distances between devices were not studied. Therefore, this study focuses on analysing the influence of such parameters in the configuration of co-located wind and wave energy systems and quantifying the resulting mooring line fatigue.

1.3 Objectives

This thesis aims to evaluate the effects of co-locating WECs with FOWTs on the fatigue behaviour of mooring cables. The specific objectives are:

- Model realistic sea states using statistical and probabilistic techniques;
- Simulate the hydrodynamic interaction between FOWTs and WECs using advanced numerical tools such as SWAN, WEC-Sim, and MooDy;
- Assess the influence of WEC array configurations on mooring line fatigue performance;
- Identify co-location strategies that reduce fatigue damage and extend the lifespan of mooring systems.

1.4 Structure of the Thesis

The outline of this thesis comprises eight chapters that provide both theoretical background and a detailed account of the methodology applied to evaluate mooring line fatigue in a co-located system. The chapters are organised as follows:

In the present chapter, a brief introduction to the thesis topic is given, followed by the problem statement, objectives, and the structure of the dissertation.

Chapter 2 presents a literature review covering the current state of research on the main topics addressed. It places particular emphasis on the co-location of marine renewable energies, sea state generation methods, the modelling tools employed (SWAN, WEC-Sim, MooDy), fatigue analysis in FOWTs and mooring systems, and the application of Design of Experiments (DoE) and statistical analysis.

Chapters 3, 4, and 5 constitute the theoretical foundation for the study. Chapter 3 reviews fundamental concepts of wave theory, including regular and irregular wave modelling and spectral analysis. Chapter 4 discusses marine renewable energy technologies, with a particular focus on Floating Offshore Wind Turbines (FOWTs) and Wave Energy Converters (WECs), as well as the benefits and challenges of their co-location. Chapter 5 describes the numerical modelling tools used in this research, detailing their capabilities and how they are applied within the simulation workflow.

Chapter 6 outlines the methodology adopted in this study, addressing the selected site and data collection process, the definition of representative sea states using joint probability distributions, and the configuration of the simulation scenarios using Design of Experiments. The simulation workflow is described in detail, including how each modelling tool was used. Finally, the statistical analysis methods applied to assess fatigue results are presented.

Chapter 7 presents and analyses the results obtained from the simulations. It discusses the effects of co-location on the wave field, platform motions, mooring line responses, and fatigue damage. The influence of WEC layout parameters is evaluated, and statistical tools are used to identify the most impactful factors and optimal configurations.

Finally, Chapter 8 summarises the study's main conclusions and outlines potential directions for future research.

Chapter 2

Literature Review

The main purposes for conducting this literature review are:

1. Assess the current knowledge regarding the fatigue analysis of Floating Offshore Wind Turbines with Co-Location of Wave Energy Converters;
2. Identify outcome variables and physical factors to seed the brainstorming for the simulation phase.

To achieve the objectives of this chapter, a wide range of books, articles, and established norms were consulted across the relevant subject areas. The research prioritises using recent and technologically up-to-date sources, with a general cutoff of 15 years to ensure relevance and accuracy. However, older sources were incorporated to provide necessary foundational insights in cases where contemporary literature was insufficient, particularly concerning WAFO (Wave Analysis for Fatigue and Oceanography).

2.1 Co-Location of Marine Renewable Energy

The co-location of WECs and FOWTs has been increasingly recognised as a more efficient strategy for marine renewable energy exploitation. According to Perez-Collazo et al. (2014), co-location offers a unique opportunity to share infrastructure, reduce overall deployment costs, and potentially mitigate mechanical loading due to wave field interactions. In this context, Clark and Paredes (2018) investigated the co-location of a single WEC and FOWT in the North Sea, finding that the presence of the WEC led to an 8.3% reduction in fatigue damage caused by first-order wave loads over 20 years. From an economic standpoint, Ramos et al. (2022) calculated the Levelized Cost of Energy (LCoE) for both isolated and co-located configurations, reporting a notable decrease in LCoE and a 44% reduction in operation and maintenance costs due to shared infrastructure.

Subsequent research has extensively examined the performance and spatial arrangement of WECs, both in isolation and when co-located. Perez-Collazo et al. (2014), Astariz et al. (2015), and Iglesias and Carballo (2014) focused on the WaveCat device, demonstrating the effectiveness of multi-row and alternative configurations in attenuating wave energy (Figure 2.1). Astariz et al.

(2015) further observed that closely spaced WEC arrays can significantly reduce wave height, potentially diminishing the energy output of downstream devices. This suggests that the strategic placement of WECs near FOWTs could influence mechanical loading through wave height attenuation. To this end, Carballo and Iglesias (2013) recommended a minimum spacing of 2.2 times the device diameter between WaveCats to mitigate such effects.

Traditionally, layout decisions are guided by the predominant wave direction and commercial feasibility. However, Teixeira-Duarte et al. (2025) introduced an innovative approach by integrating a genetic algorithm with the SWAN model to optimise WEC array layouts. This methodology achieved an 87% increase in absorbed wave power and a 46% reduction in wave height compared to non-optimised configurations.

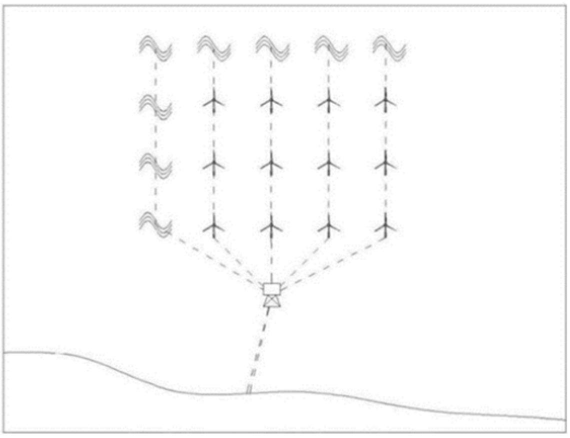

Figure 2.1: Example of a co-location system (Perez-Collazo et al., 2014).

2.2 Generation of sea states

Many approaches can be used to pass on to the generation of the sea states parameters. Fernandez et al. (2012) chose two sea states according to the power conversion of the device in order to have results to compare. In this case, the variation of the angle of attack of the WEC was the dominant factor in the simulation.

For instance, Teixeira-Duarte et al. (2025) applied statistical analysis and machine learning, specifically k-means clustering, to extract representative sea states from large metocean datasets based on significant wave height (H_s), peak period (T_p), and wave direction (θ). Additionally, Barrera et al. (2020) used a maximum dissimilarity technique to ensure diversity in the selected sea states, while Ladeira et al. (2022) employed joint probability distributions between H_s and T_p to maintain statistical coherence.

Maintaining the same methodology, Clark and Paredes (2018), following Li et al. (2013) 's methodology of using a joint probability distribution, defined a fixed set of 40 sea states. Established standards, such as DNVGL-OS-E301 (2018), recommend using 10–50 sea states for fatigue analysis and emphasise using joint probability distributions for their definition. Meanwhile, Monteiro (2017) selected four high-energy sea states (using scatter diagrams) and introduced wave direction as a three-level categorical variable (N, NW, W). Finally, Pecher and Kofoed (2016) recommended using scatter diagrams and iso-probability contour lines to guide sea state selection, either through frequency weighting or along lines of equal probability. This evolution reflects a shift toward more nuanced and computationally intensive methods for capturing real ocean variability.

While there are many ways of defining sea states, there is a lack of studies considering the influence of the wind field on these and other variables and their correlation with the definition of the wave climate.

2.3 Modelling Tools

2.3.1 Simulating WAves Nearshore (SWAN)

In order to analyse the phenomena associated with wave climate, like the effect of WECs in the wave field and potential shadow effect for the FOWT, wave modelling tools play a crucial role. The SWAN model has been widely adopted in this context due to its ability to simulate spatially varying wave fields concerning bathymetry and directional wave spectra. Carballo and Iglesias (2013) used SWAN to examine single and double row layouts of WECs and their effect on the shoreline. Their results indicated substantial spatial variation in wave energy due to bathymetric effects. They showed that while WECs reduced wave energy, diffraction could restore a significant portion of the downstream wave power.

Additionally, SWAN was used by Perez-Collazo et al. (2014) where the co-location of wave and offshore wind farms was studied, studying the shadow effect. This research used a multi-row WEC system in one direction, and it was possible to reduce between 13.08% and 25.74% of the wave height. The higher values of reduction correspond to a smaller distance between WECs and FOWT. Perez-Collazo et al. (2014) did not have the opportunity to study the wind-wave interaction, and it should be part of future work. Lastly, Amarouche et al. (2023) compared SWAN and WaveWatch III (WWIII) in their performance to simulate the directional wave spectra, comparing a buoy. Both performed well, but SWAN showed a higher accuracy in estimating the spectral energy and spectral mean directions. In contrast, WWIII performed better at lower frequencies.

In all these studies, wave simulations were conducted under stationary conditions, typically using a JONSWAP spectrum with a fixed peak enhancement factor ($\gamma = 3.3$). While this is a common practice, it is possible to compute γ based on observed correlations among sea state parameters for more accurate spectral characterisation.

2.3.2 WEC-Sim and Moody

The accurate simulation of mooring dynamics under co-location scenarios increasingly relies on coupled time-domain simulations (Barrera et al., 2020). Tools like MooDy, used by Palm (2014) and Yang et al. (2016), have proven especially useful due to their ability to capture high-frequency dynamic effects such as snap loads. Also, Palm (2014) stated that the end-point of the mooring line is the one that suffers most fatigue, and it is common only to study this point - as Clark and Paredes (2018) did. Palm's research consisted of 3 papers: a study on the convergence of the discretisation for a hanging catenary shape; dynamic convergence verification for a standing wave; and a validation study where the end-point force is compared with experimental data. The results presented a clear dependence on wave height in the resonance region of the cylinder, and lowered tension force due to inaccurate motion results in surge.

Meanwhile, Yang's comparison between coupled and decoupled modelling approaches showed that while both methods yield similar static responses, only the coupled models accurately capture the interactions between WECs, mooring lines, and seabed friction, particularly under irregular wave loading. Clark and Paredes (2018) used a coupled approach using Moody and WEC-Sim in a 3-hour simulation as DNVGL-OS-E301 (2018) recommends. They found a correlation between the surge and pitch motions, and between the heave motion and the tension.

Regarding the simulation setup in these tools, few studies were found using a discretised wave spectrum as input; most assume a predefined JONSWAP spectrum. However, the present dissertation will use a discretised spectrum derived from SWAN outputs to reflect site-specific conditions better.

2.4 Fatigue analysis

Investiganting the fatigue analysis of mooring systems is crucial, particularly when subjected to irregular sea states and dynamic loads. The approaches to analyse fatigue must follow guidelines set by standards such as DNVGL-OS-E301 (2018). These guidelines consider several states of fatigue such as: Ultimate (ULS), Accidental (ALS), Fatigue (FLS) and Service (SLS). These limit states contribute to properly ensuring the resistance of the mooring and its service criteria. In DNVGL-OS-E301 (2018), a methodology is presented for both frequency domain and time domain analysis. The choice of using frequency or time domain analysis is typically taken according to the wave climate to be analysed and the computational effort that can be taken. Authors usually use a frequency domain analysis when using SWAN (Carballo and Iglesias, 2013; Teixeira-Duarte et al., 2025; Astariz et al., 2015) and a time domain analysis when using WEC-Sim and Moody (Clark and Paredes, 2018; Palm, 2014; Yang et al., 2016).

Moreover, Barrera et al. (2020) advocated for a methodology for assessing floating offshore wind turbine mooring system fatigue considering the whole lifetime of the structure. The method integrates the impact of the life cycle metocean conditions over the dynamic performance of the platform thanks to coupled numerical models selection, non-linear data interpolation techniques and commonly accepted fatigue approaches. This approach eliminates the uncertainties due to selecting a reduced set of sea states. It was compared with the conventional method, and there were differences between 13% and 49% depending on the S-N curves used, with the conventional one being more conservative. Meanwhile, Li et al. (2013) introduced long-term joint probability models to represent environmental conditions, stressing the importance of probabilistic modelling for both wind and wave loads.

Finally, the most common way to compute the accumulated fatigue analysis is by the Miner's Rule used by Clark and Paredes (2018), Barrera et al. (2020), Yang et al. (2016), and validated by DNVGL-OS-E301 (2018). In this study, the same methodology will be used and follow Clark and Paredes (2018) to compute the fatigue using WAFO that performs rain flow counting.

2.5 Design of Experiments and Statistical Analysis

When many design variables and levels must be considered in experiments, running a full factorial set of simulations becomes computationally infeasible. In such cases, Design of Experiments (DoE) methods offer structured approaches to sample the design space efficiently. As noted by Ingram et al. (2011), DoE enhances the signal-to-noise ratio by amplifying causal relationships through factorial and Taguchi designs or minimising extraneous variability using randomisation and blocking. These approaches are widely used when computational resources are limited and full factorial becomes unfeasible.

Though validated by Ingram et al. (2011), not many researchers in marine renewable energy have used this method to specify the simulation scenarios. Nevertheless, studies such as Jani et al. (2016) show how Taguchi designs and Analysis of Variance (ANOVA) effectively identify dominant factors and enhance robustness in fatigue analyses. ANOVA will help quantify the relative importance of the studied variables on fatigue of the mooring lines. The S/N ratio will support assessing performance robustness against sea state variability, helping to balance efficiency and resilience. Figure 2.2 represents the working principle of using the Taguchi method.

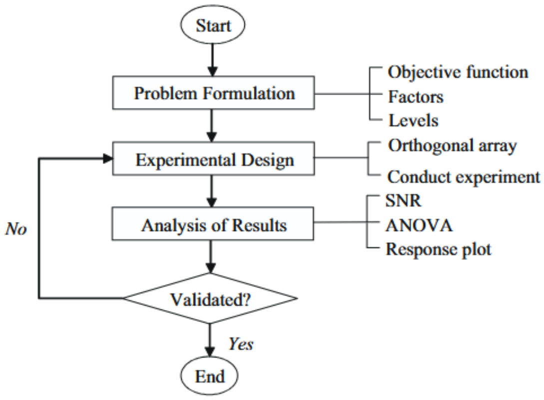

Figure 2.2: Flow diagram of Taguchi working principle.

Overall, these studies demonstrate significant progress in modelling wave energy extraction, co-location performance, and mooring dynamics. Nonetheless, few works account for wind fields and more than one direction in the sea states to study. This might be due to the fact that the wave and wind farms are located nearshore, not having more than one predominant direction of waves. Moreover, the definition of sea states commonly depends on only significant height and peak period, without trying to correlate the other parameters.

This research aims to address these gaps by:

- Correlating sea state parameters to create realistic input conditions;
- Including wind fields, calculation of peak enhancement factors (for JONSWAP spectra), mean direction, and directional spread;
- Using Design of Experiments (DoE) for WEC layout simulations;
- Applying ANOVA and signal-to-noise analysis to quantify factor influence and response robustness.

Chapter 3

Wave Theory

Understanding the local wave climate is essential for marine structures' design, performance assessment, and survivability. It plays a vital role in evaluating the dynamic response of these systems and is crucial for accurately predicting fatigue and assessing energy potential. The wave climate at a given location is typically described using statistical and spectral parameters derived from long-term observational datasets, numerical hindcasts, or satellite altimetry (DNVGL-OS-E301, 2018; Pecher and Kofoed, 2016).

Ocean surface waves are primarily generated by wind, although other sources such as tides and seismic activity can also contribute. Wind-generated waves result from transferring momentum from the atmosphere to the ocean surface, producing oscillatory motion that can propagate over long distances. These waves are generally classified into wind waves, formed locally by wind, and swell waves, which originate from distant weather systems and persist after the wind has subsided (Dhanak and Xiros, 2016).

3.1 Regular Waves

A typical ocean wave is often simplified as a sinusoidal oscillation (Figure 3.1), characterised by a wave height H (the vertical distance between crest and trough), wavelength λ (the horizontal distance between successive crests or troughs), and wave period T (the time interval between successive wave crests passing a fixed point) (Pecher and Kofoed, 2016).

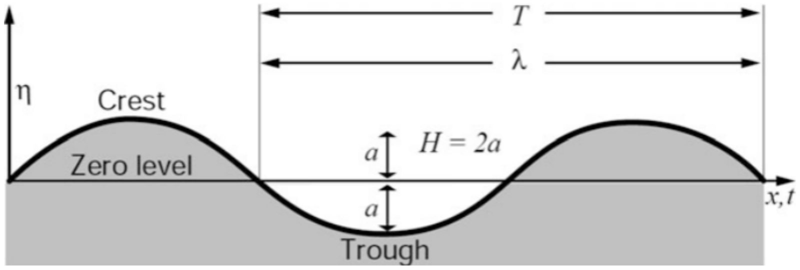

Figure 3.1: Representation of wave parameters of a sinusoidal wave (Pecher and Kofoed, 2016).

From these main parameters, it is possible to define others, such as the wave number defined as:

$$k = \frac{2\pi}{\lambda} \tag{3.1}$$

and the wave frequency defined as:

$$\omega = \frac{2\pi}{T} \tag{3.2}$$

Furthermore, wave theories were developed, approximations to reality that aim to describe wave phenomenon. However, they only apply under certain conditions that satisfy the assumptions made when the theory was created.

3.1.1 Linear Wave Theory

Linear wave theory, or Airy wave theory, provides the fundamental framework for analysing ocean surface waves. It assumes that wave amplitudes are small relative to their wavelengths and water depth, which allows the governing equations to be linearised. This theory is particularly valid for moderate sea states in deep water, where wave steepness is low (Pecher and Kofoed, 2016).

One of the key advantages of linear theory is the principle of superposition. Because the governing equations are linear, the total response of the system can be obtained by summing the individual contributions of each wave component. This means that when two or more waves with different heights and periods overlap, the total free surface elevation is simply the sum of the elevations of each wave. The same principle applies to wave-induced quantities such as pressure, velocity, acceleration, and particle displacement (Monteiro, 2017).

Therefore, the waves' free surface elevation, that is, the elevation of the water surface relative to the still water level, is given by:

$$\eta = \frac{H}{2} \cos\left(kx - \omega t + \varepsilon\right) \tag{3.3}$$

where t is the time, x is the horizontal coordinate, and ε is the phase.

Despite its usefulness, linear theory has limitations. In extreme sea states or shallow water conditions, nonlinear effects become significant, and the simplified assumptions of linear theory may lead to inaccurate results. Higher-order or fully nonlinear models are required for more precise analysis in such cases (Pecher and Kofoed, 2016).

3.2 Irregular Waves

In the open ocean, wave fields are inherently irregular. They are characterised by a complex, naturally occurring ocean wave pattern composed of a superposition of multiple sinusoidal wave components (Figure 3.2), each with different frequencies, amplitudes, and directions. Considering

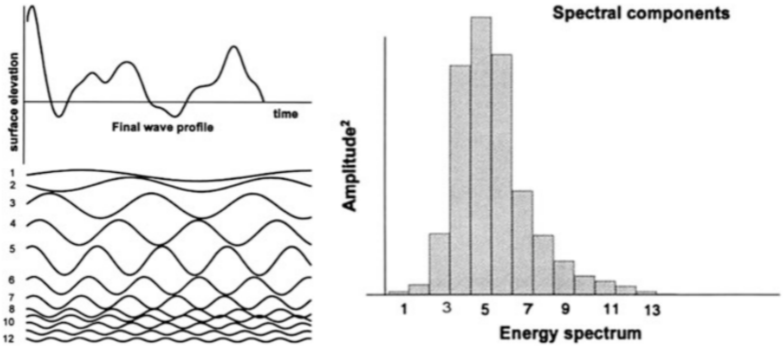

Figure 3.2: Super-positioning of waves (corresponding to spectral components) to create water surface elevation (left) and the resulting spectrum (right) (Pecher and Kofoed, 2016).

the linear waves theory, the sea surface elevation $\eta(t)$ at a fixed point can be modelled as a sum of sinusoidal components (Gomes, 2018; Pecher and Kofoed, 2016).

In irregular wave analysis, an individual wave is typically defined as the portion of the sea surface elevation between two consecutive zero-crossings with the same direction. A down-crossing zero is the point at which the surface elevation crosses the mean water level from positive to negative values. Conversely, an up-crossing zero occurs when the surface elevation crosses negative to positive values.

The energy distribution of these components is described by the wave energy spectrum $S(\omega)$, which quantifies the variance of the sea surface elevation per unit frequency (Pecher and Kofoed, 2016):

$$\int_0^\infty S(f)\,df = \frac{1}{2}\langle \eta^2(t) \rangle \tag{3.4}$$

The total wave energy per unit surface area is given by (Pecher and Kofoed, 2016):

$$E = \frac{1}{16}\rho g H_s^2 = \rho g \int_0^\infty S(f)\,df \tag{3.5}$$

where H_s is the significant wave height, ρ the water density, and g the gravitational acceleration.

3.2.1 Spectral Models

The most common model used is the Pierson-Moscowitz (PM) spectrum (Equation 3.6). This one assumes a fully developed sea where wave energy is in equilibrium with the wind and depends only on wind speed (Pecher and Kofoed, 2016).

$$S_{PM}(f) = \frac{\alpha g^2}{f^5} \exp\left(-\beta \left(\frac{f_p}{f}\right)^4\right) \tag{3.6}$$

where $S_{PM}(f)$ is the spectral density (m^2/Hz), f is wave frequency defined by the inverse of time period (Hz), g is acceleration due to gravity ($9.81 m/s^2$), α is the Phillips constant (approximately $8.1 \cdot 10^{-3}$), β is the spectral decay constant (1.25) and f_p is the peak frequency (Hz).

Joint North Sea Wave Observation Project (JONSWAP) spectrum is derived from the PM spectrum and includes fetch-limited seas by introducing a peak enhancement factor, γ. JONSWAP and PM spectra are identical when the peak enhancement factor of the JONSWAP spectrum is equal to 1.0 (Pecher and Kofoed, 2016). The JONSWAP spectrum is defined by:

$$S_J(f) = \frac{\alpha g^2}{f^5} \exp\left(-\frac{5}{4}\left(\frac{f_p}{f}\right)^4\right) \gamma^{\exp\left(-\frac{(f-f_p)^2}{2\kappa^2 f_p^2}\right)} \tag{3.7}$$

where γ is the peak enhancement factor and κ is the spectral width.

According to (Ruehl et al., 2024), the peak-enhacement factor can be estimated as:

$$\gamma = \begin{cases} 5 & \text{for } \dfrac{T_p}{\sqrt{H_s}} \leq 3.6 \\ \exp\left(5.75 - 1.15\dfrac{T_p}{\sqrt{H_s}}\right) & \text{for } 3.6 < \dfrac{T_p}{\sqrt{H_s}} \leq 5 \\ 1 & \text{for } \dfrac{T_p}{\sqrt{H_s}} > 5 \end{cases} \tag{3.8}$$

Both spectra assume sea states that are generated by a single wind source. When the case cannot be applied, typically for two distinct sources of waves, then the sea state is called bimodal and has two peaks with different peak directions and frequencies (Pecher and Kofoed, 2016) (Figure 3.3.

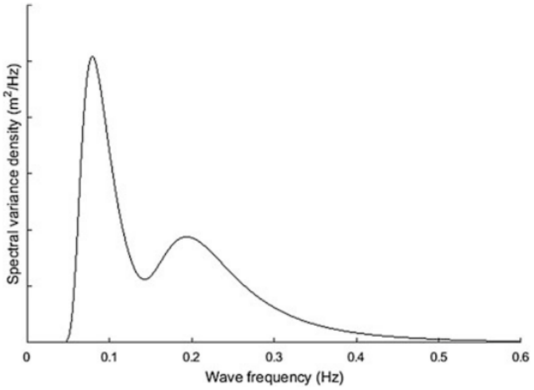

Figure 3.3: Bimodal spectrum (Pecher and Kofoed, 2016).

3.2.2 Wave Parameters

Several statistical and spectral parameters are used to characterise a sea state. These parameters can be derived from time-domain analysis (e.g., zero-crossing methods) or frequency-domain analysis using wave spectra.

The most widely used measure of wave height is the Significant Wave Height, which can be defined in two main ways:

- In the time domain, it is denoted as $H_{1/3}$ and represents the average height of the highest one-third of waves in a record;
- In the frequency domain, it is denoted as H_{m0} and is derived from the zeroth spectral moment m_0:

$$H_{m0} = 4\sqrt{m_0} \tag{3.9}$$

where

$$m_n = \int_0^{+\infty} f^n S(f) df \tag{3.10}$$

This spectral definition is preferred in wave energy applications because it directly relates to the total energy content of the sea state. However, for practical reasons, Significant Height is denoted as H_s, and it is not possible to know how this parameter was calculated from the notation unless it is stated.

In terms of wave period, various definitions exist on the context,

- Mean zero-crossing period (T_z): the average time between successive zero-crossings (up-crossing or down-crossing) in the time series. Spectrally, it can be estimated as (Pecher and Kofoed, 2016):

$$T_z \approx T_{m02} = \sqrt{\frac{m_0}{m_2}} \tag{3.11}$$

- Energy period (T_e): a spectral period that emphasises the energy-carrying components of the spectrum (Pecher and Kofoed, 2016):

$$T_e \approx T_{m10} = \frac{m_{-1}}{m_0} \tag{3.12}$$

- Peak Period (T_p): the period corresponding to the peak of the wave spectrum, i.e., the most energetic frequency component (Pecher and Kofoed, 2016):

$$T_p = 1/f_p \tag{3.13}$$

For specific spectral shapes, such as the JONSWAP spectrum with a peak enhancement factor $\gamma = 3.3$, the following empirical relationships are often used (Pecher and Kofoed, 2016):

$$T_p \approx 1.29 T_z \approx 1.12 T_e \tag{3.14}$$

These ratios are proper for converting between different period definitions when only one is available.

Real sea states are also directionally spread. The directional spectrum $S(f, \theta)$ accounts for energy distribution over frequency and direction. A common model is (Pecher and Kofoed, 2016):

$$S(f,\theta) = S(f) \cdot \varepsilon(\theta) = S(f) \cdot \frac{2}{\pi} \cos^{2s}(\theta - \theta_0) \tag{3.15}$$

where θ_0 is the mean wave direction and s is a directional spreading parameter.

These parameters are essential for describing sea states and are widely used in wave energy resource assessment, device design, and numerical modelling.

Chapter 4

Marine Renewable Energy

This chapter explores wind and wave energy in depth. The section on offshore wind energy focuses on mooring systems and environmental loading conditions. Additionally, the wave energy section examines the leading technology types and their interaction with the wave field. The chapter concludes with an overview of co-location, highlighting the synergies, challenges, and future outlook of integrating these systems in shared maritime zones.

4.1 Offshore Wind Turbines

Wind energy is a crucial component of the global transition to renewable energy. Offshore wind energy offers distinct advantages such as minimal land use conflicts and reduced acoustic and visual disturbances (Barrera et al., 2020). However, deploying offshore turbines presents engineering challenges, particularly related to the complex environmental conditions and the design of support structures in deep waters.

4.1.1 Wind Turbines Components

The main components of Offshore Wind Turbines, according to (Dhanak and Xiros, 2016), are:

- Rotor: converts the kinetic energy in the wind to rotational energy of the rotor and drivetrain by utilising aerodynamic lift. Composed by:
    - Rotor blades: extract power from the wind;
    - Hub: component that combines the rotor blades and connects the rotor to the drivetrain.
- Nacelle: contains the drivetrain, generator, and other equipment such as hydraulic machinery and protects it from the weather. It also provides the support frame for the drivetrain. Composed by:
    - Drivetrain: is the rotating connection between the rotor and the generator;
    - Bearings and generator.

- Support Structure. Composed by:
  - Tower: hollow (or steel lattice) structure usually made of concrete, steel or a combination of both. It encloses cables to connect to the electrical grid;
  - Substructures and Foundations: keep the turbine in position while being exposed to external natural conditions.

Offshore wind turbines come in various foundation types, with the choice primarily depending on water depth, terrain, and turbine capacity. The main types of foundation are monopile, tripod, and floating structures (Figure 4.2).

Currently, offshore wind turbines in Europe primarily use monopile foundations, as these structures are typically deployed in shallow waters (Figure 4.1). However, floating platforms present significant cost advantages, particularly when supporting larger capacity turbines. The following sections will therefore focus on Floating Offshore Wind Turbines (FOWTs).

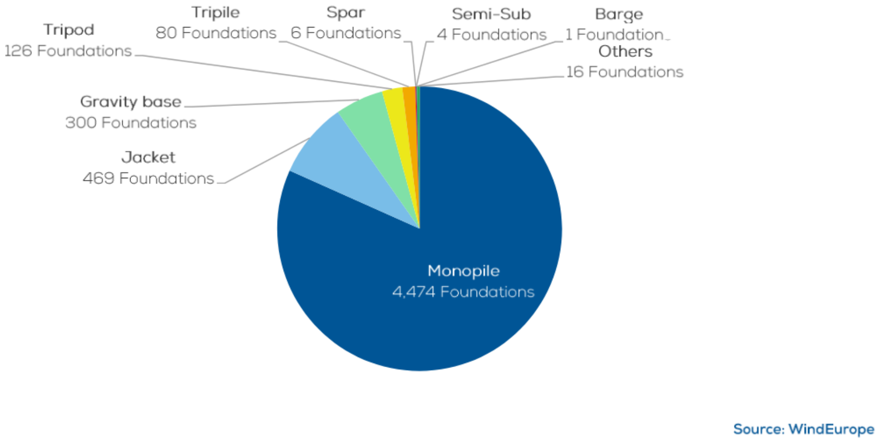

Figure 4.1: Share of substructure types for grid-connected wind turbines in 2020 (Costanzo et al., 2025).

4.1.2 Foundations and Mooring System

The floating platform allows deployment in deeper waters, typically beyond 50 meters, where fixed-bottom foundations such as monopiles or jackets are no longer feasible (DNVGL-OS-E301, 2018).

The three principal types of floating platforms are spar-buoy, tension leg platform (TLP), and semi-submersible. This division is based on the way the platforms achieve stability. Each design offers different trade-offs in terms of cost and ease of installation.

Spar-buoy: The stability of a spar-buoy is ensured by an imbalance of weights between the upper and lower parts of the ballast. The lower part is heavier, moving the centre of gravity down. This results in a torque that keeps the spar straight.

Theoretically, the spar-buoy can straighten the tower only using the ballast and buoy. This means that the catenary mooring lines would be used to keep the turbine in place. However, the buoy also needs the mooring lines to achieve stability.

Tension Leg Platform: This foundation consists of a slender cylindrical buoy anchored to the seabed with taut leg mooring lines.

The weight of water displaced by the buoy must be larger than the combined weight of the wind turbine and the buoy. Theoretically, the TLP would be able to hold in this way. However, a reserve buoyancy is included to tension the mooring lines connected to anchors on the seafloor.

Semi-Submersible and Barge: These platforms combine features from the two previous types. This platforms contain a buoyancy tank that will hold the platform straight, and mooring lines to anchor the platform on the seabed.

Floating platforms must remain stable and in position despite the ocean's dynamic environment. This is achieved using mooring systems that anchor the floating platform to the seabed while allowing limited motion. Mooring lines can be classified in terms of arrangement or material.

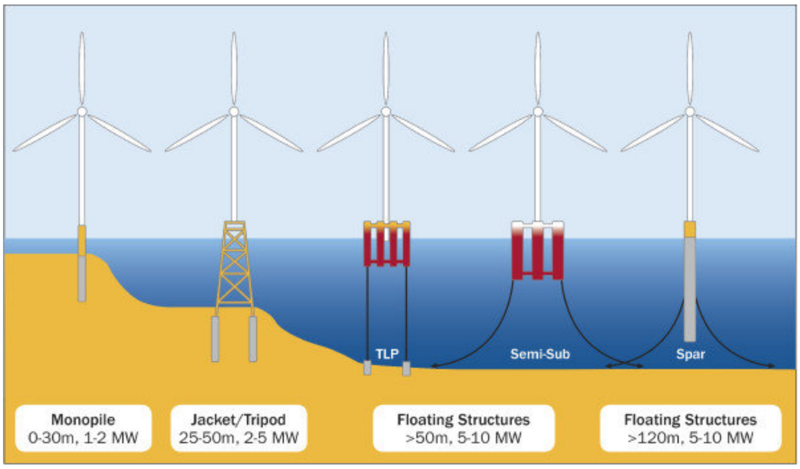

Figure 4.2: Types of Offshore Wind Turbines (Rolo Pérez, 2014).

The primary materials used are: chains, wire ropes and synthetic fibre ropes. The chain is most commonly used because it is less sensitive to damage and corrosion than wire ropes. Additionally, the main mooring configurations include catenary, semi-taut, and taut systems (Figure 4.3). The configuration choice depends on water depth, platform type, and site conditions (DNVGL-OS-E301, 2018).

Catenary mooring: A significant length of the lines lies on the seabed, causing the anchor to be loaded in a horizontal direction. The types of mooring used in these are chains and wire ropes.

Catenary moorings are usually used in spar-buoy platforms. They are cost-effective and straightforward, but require a large seabed footprint, making them less suitable for densely packed arrays or environmentally sensitive sites.

Taut mooring: The mooring does not lie on the seabed and makes an angle with the seabed. Taut mooring allows the anchor to be deployed vertically or horizontally. Usually, synthetic ropes are used. This configuration leaves a smaller footprint compared to catenary mooring.

The load effects are based on the predicted tensions in the mooring lines. The analysis of the line tensions shall consider the motion of the floating unit induced by environmental loads and the response of the mooring lines to these motions. The characteristic load effects are obtained for stationary, ecological states. Each stationary environmental state may be specified in terms of: Significant Height, Peak Period, Wave Spectrum, Main wave direction, Mean wind speed, among others (Chapter 3) (DNVGL-OS-E301, 2018).

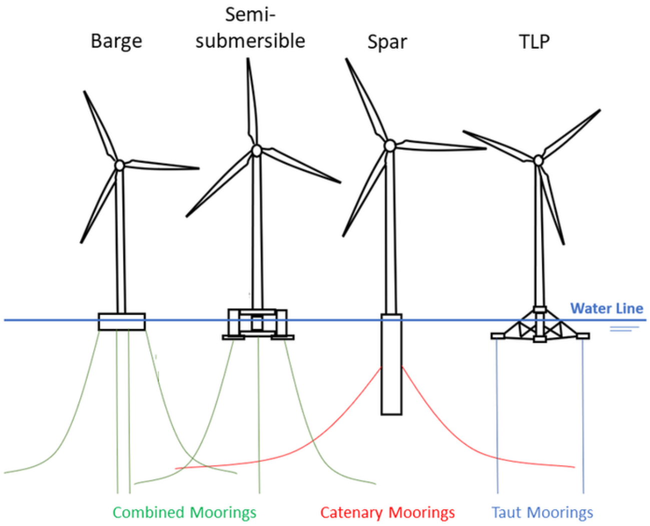

Figure 4.3: Common types of mooring systems (Ladeira et al., 2022).

4.1.3 Environmental Loads and Hydrodynamics

As mentioned above, FOWTs are subject to aerodynamic, hydrodynamic, and inertial loads. The hydrodynamic loads are particularly complex and arise from the interaction between ocean waves and the platform. These include:

- Wave excitation forces: direct forces from incoming waves;
- Added mass effects: apparent increase in inertia due to displaced water;
- Radiation damping: energy loss due to waves radiated by platform motion;
- Quadratic drag: non-linear resistance from water movement around the structure.

The floating platform experiences six degrees of freedom (DOF): surge, sway, heave, roll, pitch, yaw. The equations governing the platform motion are typically expressed in matrix form:

$$(\mathbf{M}+\mathbf{A})\ddot{\mathbf{x}}+\mathbf{B}\dot{\mathbf{x}}+\mathbf{C}\mathbf{x}=\mathbf{f}_{\mathbf{ext}}(t) \tag{4.1}$$

where M is the generalised mass matrix, A is the added mass matrix, B is the radiation damping matrix, C is the hydrostatic stiffness matrix, $\ddot{x}$,$\dot{x}$ and x are, respectively, the acceleration, velocity and position vectors in the six degrees of freedom (Figure 4.4) and F_{ext} is the vector of external forces acting on the buoy (wave forces, mooring forces, etc.) (Paredes, 2016).

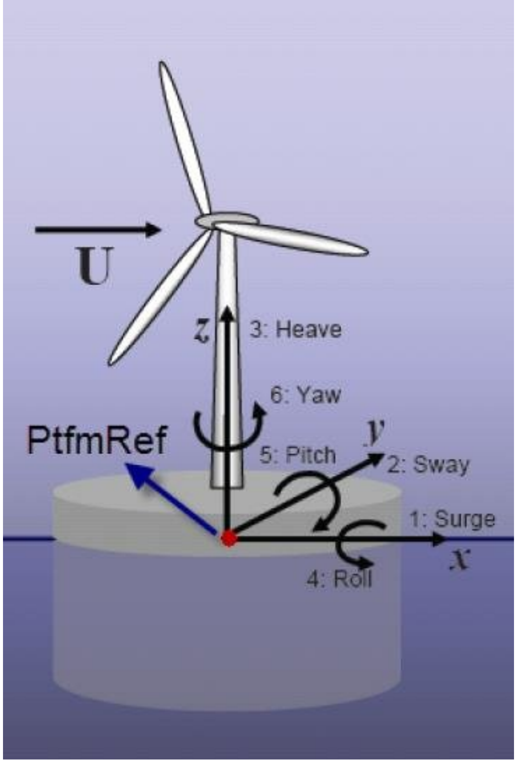

Figure 4.4: Illustration of hydrodynamic forces and six degrees of freedom acting on a semi-submersible floating wind platform (Rolo Pérez, 2014).

Added mass is a phenomenon that must be considered when dealing with the unsteady motion of bodies underwater or unsteady flow around objects. This parameter results from an additional effect (force) from the fluid acting on the structure when formulating the system equation of motion. Further information on this governing equation and numerical modelling is discussed in Chapter 5.

Wave excitation forces can be critical when analysing the environmental loads and fatigue in the mooring lines. The wave forces are external periodic forces applied to the structure. Suppose the frequency of these wave forces matches the natural frequency of the platform in a particular degree of freedom (e.g., pitch or heave). In that case, resonance occurs, leading to amplified platform motions, therefore amplified tensions.

Unlike simple mechanical systems, the natural frequencies of floating offshore wind platforms cannot be derived analytically due to the following complexities (Koo et al., 2014; Cruz and Atcheson, 2016):

- Hydrodynamic Coupling: The platform interacts with the surrounding fluid, introducing frequency-dependent added mass and damping effects that are not constant (frequency-dependent);
- Mooring System Non-linearity: Mooring lines introduce restoring forces that are non-linear and direction-dependent, especially under large displacements;
- Multi-DOF Dynamics: The six degrees of freedom are often coupled, meaning motion in one direction can influence others (e.g., pitch affecting heave);
- Environmental Variability: The platform's response depends on sea state, wave directionality, and wind loading, which vary over time.

To quantify the platform's response to wave excitation across different frequencies, Response Amplitude Operators (RAOs) are used (Cruz and Atcheson, 2016). An RAO is defined as the ratio of the response amplitude of the platform (e.g., displacement, rotation) to the amplitude of the incoming wave at a given frequency:

$$\mathrm{RAO}(\omega) = \frac{|\mathbf{x}(\omega)|}{|\eta(\omega)|} \tag{4.2}$$

where $\mathbf{x}(\omega)$ is the complex amplitude of the platform response at frequency ω, and $\eta(\omega)$ is the free surface elevation at the same frequency.

The peak frequency of this parameter for each degree of freedom will give a good approximation of the resonance frequency of the platform. And when resonance occurs, the platform experiences amplified motions, leading to larger cyclic loads on structural components and mooring lines. These increased load amplitudes accelerate fatigue damage accumulation, especially in components subjected to high-frequency oscillations or repeated stress reversals (Lamei and Hayatdavoodi, 2020; Koo et al., 2014).

4.1.4 Fatigue Analysis of Mooring Systems

Mooring lines in floating offshore wind turbines are subjected to repeated and varying loads caused by wind, waves, and platform dynamics. These cyclic loads might lead to fatigue failure, even if the peak loads are below the material's breaking stress. Accurate fatigue analysis is essential for predicting the service life of mooring systems and preventing unexpected failures (Barrera et al., 2020).

Miner's Rule (linear damage accumulation hypothesis) is a common method used to calculate fatigue life estimation. This rule assumes that fatigue damage accumulates linearly with load cycles. The cumulative damage D is calculated as:

$$D = \sum_{i=1}^{n} \frac{n_i}{N_i} \tag{4.3}$$

where n_i is the number of stress cycles experienced at a particular stress amplitude, and N_i is the number of cycles to failure at that stress level, derived from the material's S-N or T-N curves.

The number of cycles to failure N is often modelled using a power-law relationship:

$$N = a\left(\frac{\Delta\sigma}{10^6}\right)^{-m} \tag{4.4}$$

where $\Delta\sigma$ is the stress range in pascals (Pa), a is the fatigue strength coefficient, which scales the curve based on material resistance, m is the fatigue exponent, indicating the sensitivity of fatigue life to stress range variations (DNVGL-OS-E301, 2018). The values of a and m are available in DNVGL-OS-E301 (2018), depending on the specific application.

Fatigue failure is predicted when the accumulated damage reaches or exceeds unity ($D \geq 1$), indicating that the component has reached its fatigue limit.

While Miner's Rule is simple and widely adopted, it has several limitations:

- It assumes linear damage accumulation, ignoring load sequence effects;
- It does not distinguish between crack initiation and propagation phases;
- It tends to be conservative, potentially underestimating fatigue life under variable-amplitude loading.

To apply Miner's Rule, representative stress cycles must be extracted from time-domain simulations. This is typically done using the rainflow counting algorithm, which identifies and classifies stress reversals in irregular load histories.

To ensure accurate fatigue predictions, these simulations must incorporate realistic sea states and coupled hydrodynamic-mooring interactions. Tools such as WAFO are commonly used for post-processing. WAFO is a MATLAB toolbox developed for the statistical analysis of random wave processes and fatigue estimation in offshore structures (Brodtkorb et al., 2000).

4.1.5 OC4 and OC5 Floating Wind Turbine Concepts

The OC4 and OC5 projects, developed under the International Energy Agency (IEA) Wind Task 30 and coordinated by the National Renewable Energy Laboratory (NREL), represent two major phases in advancing offshore wind turbine modelling and validation. Both projects are centred around the NREL 5 MW reference wind turbine, but each introduces unique objectives and modelling challenges (Robertson et al., 2017).

The OC4 Phase II concept features the 5-MW turbine mounted on a semi-submersible floating platform called the OC4-DeepCwind. This platform consists of a central column and three offset columns connected by pontoons and braces, designed for deployment in 200 m of water depth. The mooring system comprises three catenary lines spaced 120° apart. OC4 focused on benchmarking simulation tools through code-to-code comparisons, emphasising hydrodynamic complexity and platform motion response (Robertson et al., 2014).

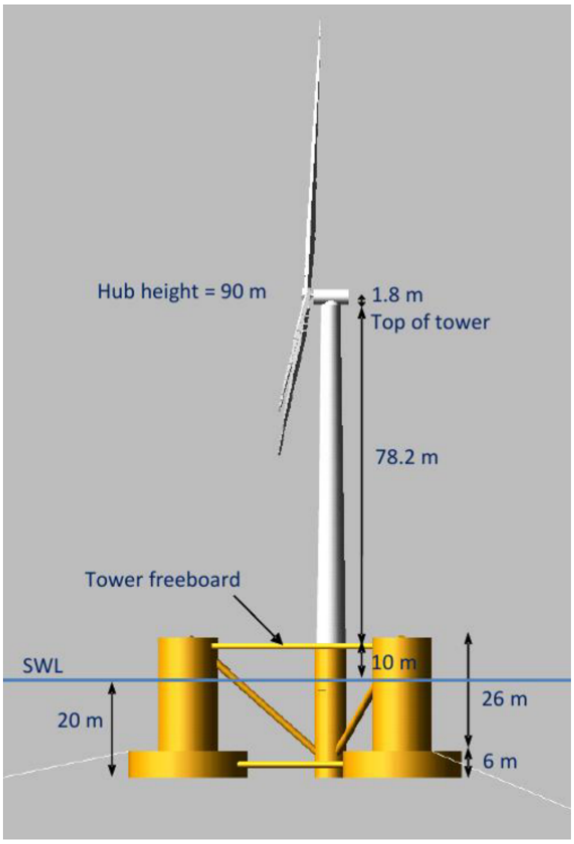

Figure 4.5: Representiation of OC5 (Robertson et al., 2017).

Building on OC4, the OC5 project extended the validation process by incorporating experimental data. While still using the same 5 MW turbine and similar floating platforms, OC5 emphasised the correlation between numerical simulations and physical measurements from wave tank experiments and field tests.. It aimed to improve the accuracy and reliability of simulation tools through model-to-data comparisons (Robertson et al., 2017).

Together, OC4 and OC5 have become foundational benchmarks in floating wind turbine research, supporting the development and validation of simulation frameworks such as FAST, OpenFAST, and WEC-Sim.

Further information used for parameterising the numerical models can be found in Chapter 6.

4.2 Wave Energy Converters

Wave Energy Converters are systems designed to extract usable energy from the ocean wave field and convert it into electricity. While the technology is still in the developmental phase compared to wind or solar energy, recent advancements and pilot projects have proven the feasibility and scalability of several WEC architectures (Dhanak and Xiros, 2016).

4.2.1 Classification of Wave Energy Converters

These converters can be classified into: working principle, orientation relative to wave direction, and deployment location. The most common classification divides them into point absorbers, attenuators, terminators, and overtopping devices (Pecher and Kofoed, 2016; Dhanak and Xiros, 2016). However, the International Energy Agency's Ocean Energy Systems (IEA-OES) suggests grouping oscillating body-based devices into a broader category called Wave Activated Bodies (WABs). Figure 4.6 from Pecher and Kofoed (2016) presents the classification of WECs from IEA-OES. Additionally, Figure 4.7 presents some examples.

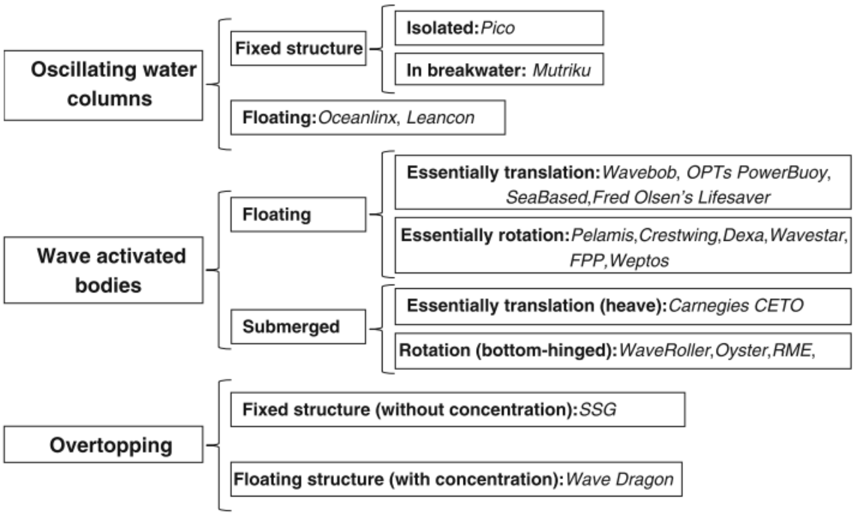

Figure 4.6: Classification of WECs according to IEA (Pecher and Kofoed, 2016).

Among these, overtopping devices have received particular attention due to their robust yet straightforward operational principle and relatively low maintenance needs. In Section 4.2.3, an extensive review of the WaveCat, an overtopping WEC, will be done, as it is the WEC model to use in the study.

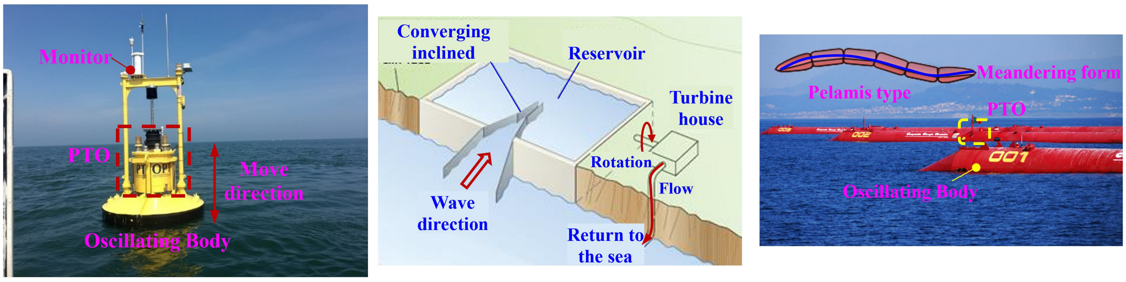

Figure 4.7: Representation of three Wave Energy Converters: PowerBouy, Pelamis and TAPCHAN, respectively (Zhang et al., 2021).

4.2.2 Influence in the wave field

WECs interact with the incident wave field by extracting energy, thereby modifying wave characteristics such as height, direction, and spectral distribution. These interactions give rise to wave attenuation, diffraction, and refraction, which alter the local and far-field wave climate. Understanding these effects is essential for optimising WEC array layouts, evaluating environmental impacts, and designing co-located marine energy systems.

The energy absorbed by a WEC can be estimated using the following expression:

$$P = \frac{1}{2}\rho g H_s^2 C_e \frac{A}{\Delta t} \tag{4.5}$$

where P is the absorbed power, ρ is the water density, g is the gravitational acceleration, H_s is the significant wave height, C_e is the energy capture coefficient of the device, A is the area, and Δt is the interval of time (Monteiro, 2017).

In array configurations, the interaction between individual devices and the wave field can lead to constructive or destructive interference patterns. These interactions influence the energy capture efficiency and the spatial distribution of wave energy. The array layout is critical in determining the extent and nature of the wave field disturbance (Astariz et al., 2015).

Beyond energy extraction, WECs can significantly influence the operational environment of nearby offshore structures. WECs can reduce wave-induced loads on adjacent platforms, mooring systems, and floating wind turbines by attenuating wave energy. This has implications for structural fatigue, stability, and maintenance requirements. For instance, co-locating WECs with floating offshore wind turbines has reduced mooring fatigue loads by modifying the incoming wave spectrum, potentially extending the service life of mooring components and reducing operational costs (Clark and Paredes, 2018).

Advanced numerical tools such as SWAN are commonly employed to simulate these interactions. These models enable the assessment of wave field modifications under realistic sea states and support the design of efficient and environmentally responsible WEC arrays (Zou et al., 2024). Within such models, the wave transmission and reflection coefficients are critical parameters that characterise how devices interact with the incident wave field.

These coefficients quantify the proportion of wave energy that is transmitted past or reflected by a WEC and are typically derived from experimental data or high-fidelity hydrodynamic simulations. Spectral wave models like SWAN allow the simulation of the spatial redistribution of wave energy due to the presence of WECs (The SWAN Team, 2024). This integration ensures that both near- and far-field effects are captured, including the wake zones and energy shadows that influence downstream conditions.

In summary, WECs function as energy harvesters and as modifiers of the marine environment. Their influence on the wave field and the structural response of nearby offshore infrastructure must be carefully considered in the planning and deploying of wave energy projects, particularly in co-located or multi-use marine spaces.

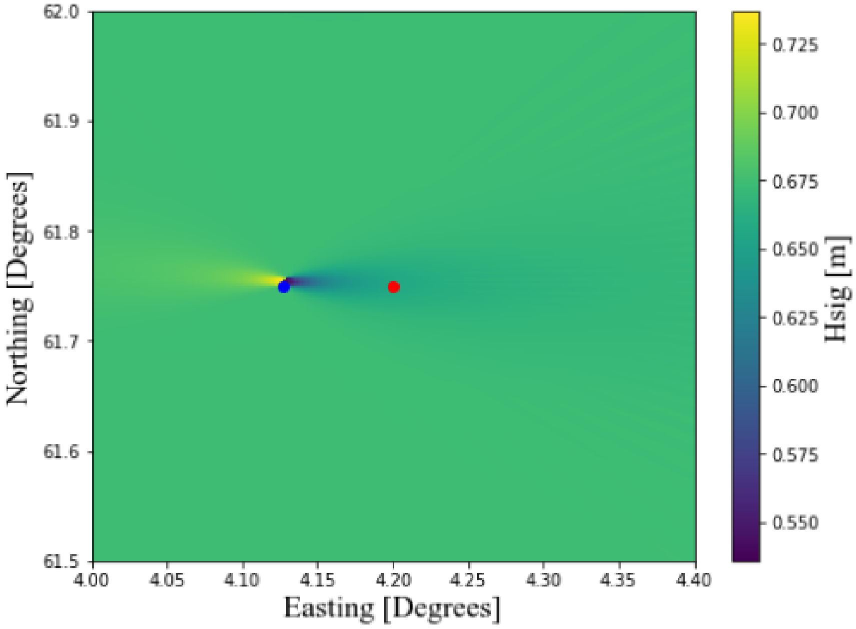

Figure 4.8: Shadow effect in a co-location solution. The blue dot represents the WEC and the red one the FOWT (Clark and Paredes, 2018).

4.2.3 WaveCat

The WaveCat is a novel floating overtopping WEC, whose principle of operation is based on oblique overtopping. Developed for offshore deployment in water depths of 50 to 100 m, it combines the wave-concentrating advantages of a converging catamaran geometry with the energy efficiency of low-head hydro turbines (Fernandez et al., 2012).

Unlike traditional catamarans with parallel hulls, the WaveCat's hulls converge toward the bow, forming a wedge that channels wave energy into a narrowing corridor (Figure 4.9). As waves propagate obliquely between the hulls, water overtops the inner hull walls and is stored in elevated reservoirs along the vessel. These reservoirs are gradually emptied through low-head turbines, generating electricity. The converging design ensures that overtopping continues progressively along the length of the device, thereby maximising energy extraction over the entire wave crest (Fernandez et al., 2012).

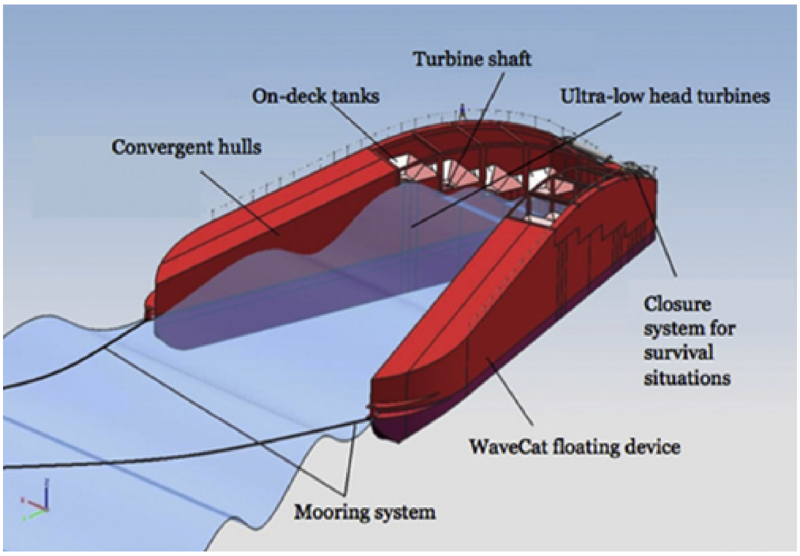

Figure 4.9: Scheme of the WaveCat WEC (Fernandez et al., 2012).

The main advantages of this device are:

- Reduced structural loading due to distributed overtopping;
- Higher reliability due to minimal moving parts—the only continuously operating components are the turbines and generators;
- Adaptability to varying sea states by adjusting the hull angle, freeboard, and draught (Fernandez et al., 2012; Carballo and Iglesias, 2013).

The CALM mooring system ensures that WaveCat always faces incoming waves, maintaining optimal performance without active positioning mechanisms. Laboratory tests with scaled prototypes in wave tanks have demonstrated the viability of the oblique overtopping mechanism and highlighted the importance of hull angle in maximising overtopping volume and power output (Fernandez et al., 2012).

The transmission coefficient of these devices varies from 0.506 to 0.807, and the reflection coefficient from 0.421 to 0.470 (Fernandez et al., 2012).

4.3 Co-Location of Marine Renewable Energy Systems

Offshore renewable energy systems have emerged as an emerging component in the global transition to sustainable energy. The most promising resources are offshore wind and wave energy, each characterised by distinct technological maturity and spatial distribution. Offshore wind energy has reached a high level of technological development and cost competitiveness, whereas wave energy remains in a pre-commercial phase, facing significant technical and economic challenges (Ramos et al., 2022). Despite these differences, the co-location of WECs and Offshore Wind Turbines is increasingly being explored as a strategy to optimise marine spatial planning, reduce costs, and enhance the reliability of energy production (Perez-Collazo et al., 2014; Kesari et al., 2019).

The synergistic integration of wind and wave energy systems offers several potential benefits. These include cost reductions through shared infrastructure, increased energy yield per unit area, smoother and more predictable power output due to resource complementarity, and improved environmental performance through consolidated spatial impacts (Perez-Collazo et al., 2014; Ramos et al., 2022).

An auspicious aspect of co-location lies in its potential to mitigate structural loads on FOWTs. Hydrodynamic interactions between WECs and FOWTs can be harnessed to attenuate wave energy before it reaches the wind turbine platform. This wave attenuation effect, often referred to as wave shadowing, can significantly reduce the amplitude and frequency of wave-induced motions (Figure 4.8), thereby decreasing fatigue loads on mooring lines, tower structures, and mooring lines (Clark and Paredes, 2018). The load attenuation not only extends the operational lifespan of components but also opens opportunities for lighter and more cost-effective structural designs.

Recent studies have highlighted that the spatial arrangement and control strategies of WECs are critical in maximising these protective effects. For instance, arrays of WECs positioned upstream of FOWTs can act as a hydrodynamic buffer, dissipating wave energy through energy extraction and diffraction. This interaction is highly sensitive to wave directionality, device spacing, and control algorithms, necessitating advanced modelling and optimisation tools to fully exploit the benefits (Clark and Paredes, 2018; Perez-Collazo et al., 2014).

4.3.1 Synergies and Development Challenges

Co-located systems present a range of synergies, the most notable of which include:

- Smoothing of Power Output: The complementary nature of wind and wave resources can lead to a more stable and continuous energy supply. Since wind and wave energy often peak at different times, their combination reduces variability in power output and improves the overall capacity factor (Kesari et al., 2019; Ramos et al., 2022);

- Cost Reduction: Co-location enables shared use of infrastructure such as grid connections, substations, and maintenance vessels. This integration has significantly reduced the LCoE of wave energy systems, bringing them closer to commercial viability (Perez-Collazo et al., 2014; Ramos et al., 2022);

- Structural Load Reduction: The deployment of WECs near FOWTs can lead to a measurable reduction in wave-induced dynamic loading. This enhances structural resilience and contributes to operational stability, particularly in harsh sea states. The resulting decrease in fatigue damage can reduce maintenance frequency and improve the economic feasibility of floating wind systems (Clark and Paredes, 2018);

- Environmental Synergies: By consolidating infrastructure within a shared marine space, co-located systems may reduce the cumulative environmental footprint compared to separate installations (Perez-Collazo et al., 2014).

Despite these advantages, several development challenges remain. Integrating floating structures in dynamic offshore environments necessitates advanced layout optimisation techniques that account for hydrodynamic interactions and mooring dynamics. Additionally, the increased design complexity and potential for interference between devices introduce uncertainties in performance and reliability. Insurance and financing may also be affected by the novelty and unproven nature of such configurations (Perez-Collazo et al., 2014; Ramos et al., 2022).

Moreover, the slower pace of wave energy technology development compared to offshore wind complicates synchronised deployment schedules, potentially extending project timelines and increasing capital risk. Addressing these challenges will require continued research, demonstration projects, and the development of robust design and simulation tools tailored to hybrid offshore energy systems.

Chapter 5

Numerical Models

5.1 Wave Field

Understanding the local wave climate is essential for the design and performance assessment of marine structures. It plays a vital role in evaluating the dynamic response of these systems and is crucial for accurately predicting fatigue and assessing energy potential.

5.1.1 Numerical Model: SWAN

SWAN is a third-generation spectral wave model developed for predicting wave transformation in coastal and offshore regions (The SWAN Team, 2024; Amarouche et al., 2023). It solves the wave action balance equation, which describes the evolution of the wave energy spectrum as a function of frequency and direction, under the influence of various physical processes such as refraction, diffraction, wave-wave interactions, and energy dissipation due to bottom friction and breaking.

In SWAN, the wave action is defined as:

$$N(\sigma,\theta) = \frac{S(\sigma,\theta)}{\sigma} \tag{5.1}$$

where $S(\sigma,\theta)$ is the energy spectral density, σ is the relative frequency, and θ is the propagation direction of the wave motion.

Hence, the governing equation in SWAN is based on the spectral action balance Eulerian equation:

$$\frac{\partial N}{\partial t} + \nabla \cdot ((\mathbf{c}_g + \mathbf{u})N) + \frac{\partial c_\sigma N}{\partial \sigma} + \frac{\partial c_\theta N}{\partial \theta} = \frac{S_{tot}}{\sigma} \tag{5.2}$$

The first term of Equation 5.2 represents the temporal variation of the action density N. The second term accounts for the spatial propagation of N in the geographical domain (along the OX and OY directions), with $\mathbf{c}_g$ being the group velocity vector and $\mathbf{u}$ the current velocity. The third term represents the variation of relative frequency σ due to changes in water depth and the presence of currents, where c_σ is the propagation velocity in frequency space. The fourth term accounts for the change in wave action due to directional refraction, with c_θ representing the propagation velocity in directional space. On the right-hand side, the source term encompasses all physical processes that generate, dissipate, or redistribute wave energy (Barajas et al., 2025).

The SWAN model requires fundamental inputs: bathymetric data, initial and boundary conditions (input spectra or conditions). Depending on the scenario, atmospheric force data (such as wind and pressure fields) and oceanic forces (like current fields) may also be needed.

In order to improve the accuracy of simulations in specific areas of interest, the user might choose to use a grid nesting approach. This method uses results from a larger, coarse-resolution computational domain as boundary conditions for a smaller, higher-resolution domain. This allows for detailed wave predictions in localised regions while accounting for broader offshore conditions (Monteiro, 2017).

Additionally, the model is capable of using different types of spatial grids, such as:

- Rectangular grids for structured domains;
- Curvilinear grids for complex coastlines;
- Unstructured grids for flexible resolution.

Besides that, SWAN can simulate obstacles. Natural obstacles, such as the coastline or islands, for example, are defined within the bathymetric data, and total reflection of the incident wave energy is assumed for them. Non-natural obstacles, such as breakwaters or other coastal protection structures, are introduced as polygonal lines defined by the coordinates of their vertices. These non-natural obstacles are assigned reflection and transmission coefficients for the incident energy (Monteiro, 2017).

Before calculating the wave action density flux from one grid point to its neighbouring points, SWAN checks whether any obstacle lines cross a grid length. If such an intersection exists, the model applies a transmission (or reflection) coefficient to the flux between those nodes. Since SWAN uses a finite volume discretisation scheme centred on the grid nodes, the presence and treatment of these obstacles can significantly influence the wave field. As a result, this can affect the amount of wave energy reaching a WEC, ultimately impacting the estimated absorbed power by altering the shape and intensity of the local wave conditions (Monteiro, 2017). A representation of how SWAN interprets obstacles in its domain can be found in Figure 5.1.

When applied to the reflection coefficient, it is always constant. However, the transmission coefficient has six ways of being defined. The first is considering that the transmission coefficient is constant; there is the option to consider it frequency-dependent and frequency and direction-dependent. The last two forms are by considering that the incident wave conditions at the obstacle and on the obstacle height influence the transmission coefficient, and finally, using the Goda/Seelig formula for computing the transmission coefficient (The SWAN Team, 2024).

This software is also able to work in three states:

- Static mode: steady-state wave field estimation;

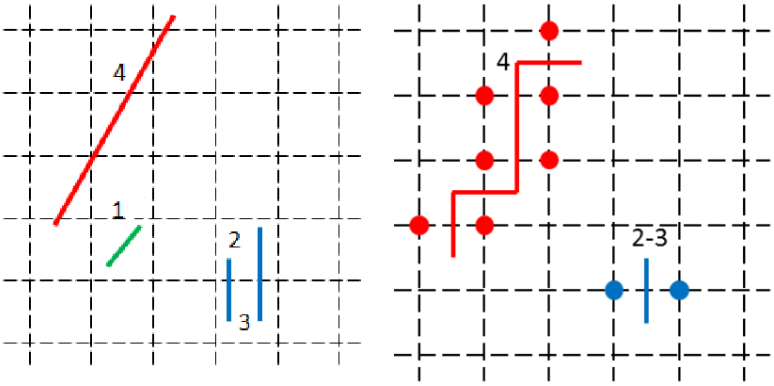

Figure 5.1: Representation of how SWAN deals with obstacles (Monteiro, 2017).

- Quasi-dynamic mode: simulates temporally variable wave fields with sequential steady-state solutions;
- Dynamic mode: full time-dependent evolution.

Moreover, this software offers various output options, including detailed tables with numerous parameters at specified locations (such as significant wave height H_s, peak period T_p, among others). Additionally, it can generate 1D and 2D wave spectra and export results in formats like .mat and .vsk, allowing visualisation of the entire computational grid or selected subregions for the parameters of interest.

In sum, this is a powerful software used to predict wave transformation on the coast, with multiple options to accurately simulate the wave conditions of a particular area or point.

5.2 Dynamics in Floating Offshore Wind Turbines

FOWTs are subjected to complex dynamic interactions between wind loading, wave excitation, structural response, and mooring system constraints. Their behaviour is highly nonlinear, with significant coupling between hydrodynamics and structural motion. This section presents the governing physical principles and numerical formulations of WEC-Sim, underlying FOWT simulations.

5.2.1 Numerical Model: WEC-Sim

WEC-Sim (Wave Energy Converter Simulator) is an open-source MATLAB/Simulink-based tool developed by the NREL and Sandia National Laboratories (SNL) to simulate WEC hydrodynamics using time-domain analysis (Wang et al., 2024; Sricharan and Chandrasekaran, 2021). Built on the Simscape Multibody environment, WEC-Sim enables modelling of multi-body systems with constraints, power take-off (PTO) systems, and control modules.

Taking into account the Equation 4.1, WEC-Sim uses it to analyse the motions of the rigid-body and the first term of this equation according to Cummins' equation for hydronamics equation can be written as (Ruehl et al., 2024):

$$(\mathbf{M}+\mathbf{A})\ddot{X} = \mathbf{F}_{\mathrm{ex}}(t)+\mathbf{F}_{\mathrm{md}}(t)+\mathbf{F}_{\mathrm{rad}}(t)+\mathbf{F}_{\mathrm{pto}}(t)+\mathbf{F}_{\mathrm{v}}(t)+\mathbf{F}_{\mathbf{B}}(t)+\mathbf{F}_{\mathbf{m}}(t) \tag{5.3}$$

where $F_{\mathrm{ex}}(t)$ is the wave excitation force, $F_{\mathrm{md}}(t)$ is the mean drift force, $F_{\mathrm{rad}}(t)$ is the radiation force, $F_{\mathrm{pto}}(t)$ is the power take-off (PTO) force, $F_{\mathrm{v}}(t)$ is the damping force due to fluid-structure interaction, $F_B(t)$ is the buoyancy restoring force due to hydrostatic stiffness, and $F_m(t)$ is the Morison Element force.

Concerning the context of this thesis, F_{pto} is not considered because there is no energy conversion (to electricity) to analyse the dynamics of mooring lines.

The radiation force includes two frequency-dependent matrices:

- The added-mass matrix $A(\omega)$, which is associated with the acceleration of the body;
- The wave damping matrix $B(\omega)$, which is related to the body's velocity.

The wave excitation force $F_{\mathrm{exc}}(t)$ consists of a Froude-Krylov component, generated by undisturbed incident waves, and a diffraction component that arises due to the presence of the floating structure. The buoyancy force $F_B(t)$ depends on the hydrostatic stiffness coefficient K_{hs}, the displacement of the body, and its mass.

Finally, the hydrodynamic coefficients required to compute these forces are provided by a frequency-domain Boundary Element Method (BEM) solver, which supplies the necessary data as functions of the wave angular frequency ω.

BEM is a potential flow-based numerical method well-suited for offshore hydrodynamics, assuming the fluid is incompressible, inviscid, and irrotational. This leads to Laplace's equation for the velocity potential:

$$\nabla^2\phi = 0 \tag{5.4}$$

The equation is solved on the wetted surface of the body using Green's theorem, reducing the problem to a boundary integral formulation. The total velocity potential is decomposed into three components:

$$\phi = \phi_{\mathrm{inc}} + \phi_{\mathrm{diff}} + \phi_{\mathrm{rad}} \tag{5.5}$$

From these components, the hydrodynamic forces are derived:

- Added mass and radiation damping from ϕ_{rad}, representing the fluid response to body motion,
- Excitation forces from ϕ_{diff}, representing the effect of incoming waves.

The resulting frequency-dependent coefficients—added mass $A(\omega)$, damping $B(\omega)$, and excitation amplitudes $F_{exc}(t)$—are exported in H5 format from solvers such as NEMOH or WAMIT. These are then interpolated and transformed into the time domain within WEC-Sim, enabling simulation of the platform's motion under irregular wave conditions. Additionally, WEC-Sim, as a linear radiation and diffraction simulator tool for WECs, does not account for second-order drift forces.

The necessary inputs in this toolbox are:

- Hydrodynamic data files (added mass, radiation damping, wave excitation forces);
- A Simulink model characterising the system;
- Wave spectrum or time-series (e.g., from SWAN);
- Body definitions, constraints, and mooring models;
- Control strategies and environmental conditions.

This tool supports rigid and flexible body modelling and can simulate devices with multiple interconnected bodies. Furthermore, it can be integrated with external mooring dynamics libraries, such as MooDy, to accurately represent mooring line behaviour and its interaction with platform motion (Clark and Paredes, 2018).

WEC-Sim provides a range of outputs, including time-domain responses such as body motions, velocities, and accelerations, as well as mooring fairlead motions. These outputs are accessible in several formats, including MATLAB structures, time-series plots, and visualisations such as animations, which ease both qualitative and quantitative analysis of system performance (Ruehl et al., 2024).

Figure 5.2 represents the workflow to use this toolbox, from input to output files.

In conclusion, WEC-Sim is a powerful and flexible simulation environment tailored for wave energy applications. Its modular structure, compatibility with external tools, and support for advanced control strategies make it well-suited for detailed performance evaluation and design optimisation.

5.3 Dynamics in Mooring Lines

Marine structures rely on mooring systems to maintain station-keeping and ensure operational stability under dynamic environmental conditions. These mooring systems are subjected to complex loading due to waves, currents, and platform motions, making accurate modelling essential for performance prediction and structural integrity assessment.

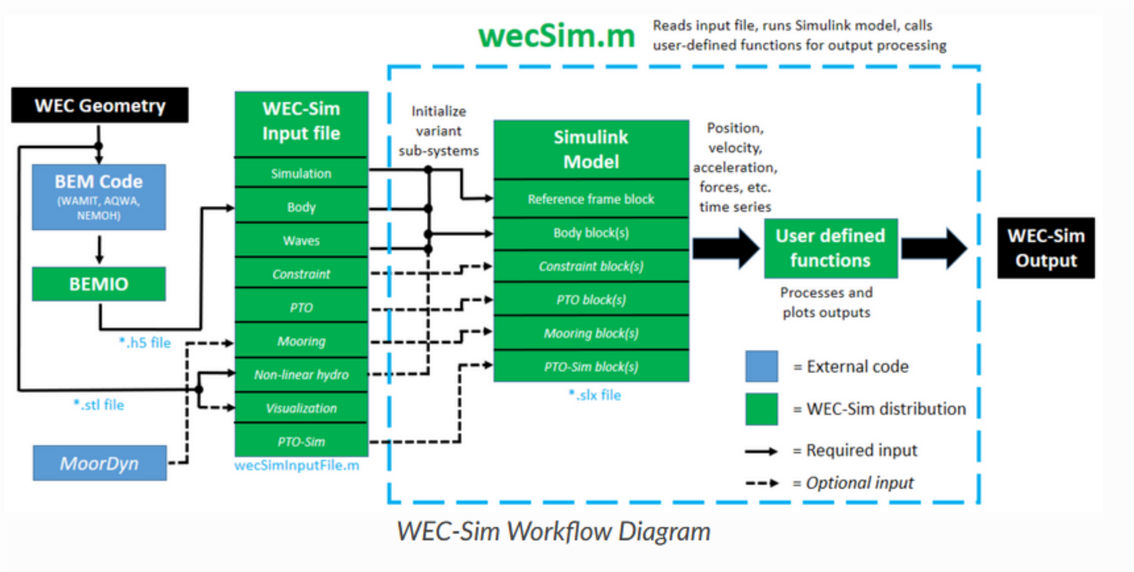

Figure 5.2: WEC-Sim Workflow Diagram (Ruehl et al., 2024).

5.3.1 Numerical Model: MooDy

MooDy is a modular finite element library designed for time-domain simulation of mooring cables under hydrodynamic loading. It employs the Local Discontinuous Galerkin (LDG) method, offering high accuracy in capturing cable behaviour, including snap loads and seabed contact (Palm, 2014; Barajas et al., 2025).

The governing equation for the cable position $\mathbf{r}(s,t)$, assuming inextensible and torsion-free behavior, is:

$$\frac{\partial^2 r}{\partial t^2} = \frac{\partial T}{\partial s} + f_{env} \tag{5.6}$$

where T is the internal tension, and f_{env} is the total environmental force per unit length.

The environmental force f_{env} is decomposed into six components:

$$f_{env} = f_1 + f_2 + f_3 + f_4 + f_5 + f_6 \tag{5.7}$$

where f_1 is gravity and buoyancy forces, f_2 is tangential added mass forces, f_3: normal added mass force, f_4: tangential drag force, f_5: normal drag force, and f_6: contact and seabed reaction forces (Palm, 2014).

The internal tension T is computed by solving the above equations using the Local Discontinuous Galerkin (LDG) method, which provides high-resolution results even in the presence of sharp gradients such as snap loads. The resulting time-domain tension histories are essential inputs for fatigue analysis, which is addressed in the section 4.1.

As mentioned in the previous section, MooDy can be implemented with WEC-Sim, where WEC-Sim works as a boundary condition for the fairlead and anchor motions. This toolbox also needs line properties (axial stiffness, damping, mass, buoyancy), seabed interaction, and friction for contact settings (Palm and Eskilsson, 2023).

The outputs of this toolbox are:

- Time-domain histories of mooring line tension, positions, and velocities;
- Stress/strain distributions along the cable;
- Snap load events and fatigue-critical points (Palm and Eskilsson, 2023).

MooDy is implemented in C++ and MATLAB and supports hp-adaptivity, making it efficient for solving high-frequency dynamics. Its ability to simulate realistic mooring behaviours, including line pretension, seabed interaction, and dynamic wave/current loading, makes it a powerful tool combined with WEC-Sim.

Chapter 6

Metodology

This chapter presents the methodology adopted to study the effects of the co-location of FOWTs and WECs on the fatigue of mooring lines. Firstly, the definition of site selection, data collection, and sea states will be addressed. The sea state definition employs a statistical analysis using Monte Carlo, which is then used as input for the numerical modelling tools. The combination of these tools aims to simulate realistic offshore conditions and evaluate the dynamic response of mooring systems. The methodology ensures reproducibility, scientific rigour, and alignment with industry standards such as DNVGL-OS-E301 (2018).

A coupled time-domain approach (using WEC-Sim and MooDy) will be employed to compute the mooring systems' dynamic response. This design is suitable for studying non-linear interactions between environmental loads, floating structures, and mooring systems. The wave field generation tool will use a frequency-domain approach for the defined sea states. Then the output spectra are used as input in WEC-Sim, and 3-hour simulations of each sea state are performed (DNVGL-OS-E301, 2018). Lastly, the fatigue analysis will be performed using rainflow-counting.

6.1 Site Description

The North Sea is a shallow shelf sea adjacent to the North Atlantic, with a mean depth of approximately 80 m. It is a semi-enclosed basin bordered by the United Kingdom, Norway, Denmark, Germany, the Netherlands, Belgium, and France. The study area is located in the North Sea between 61° N and 62.8° N and 3° E and 4.5° E (Figure 6.8), coinciding with the region analysed by Clark and Paredes (2018).

Moreover, the wave climate in the North Sea is shaped by substantial seasonal variability, storm activity, and the influence of dominant westerly winds (see Figure 6.2). These winds generate most of the wave energy, with the most pronounced effects occurring during winter. Storms frequently produce wave heights exceeding 6–10 m, whereas summer wave heights typically range from 1 to 3 m (Dodet et al., 2010). Figure 6.1 presents a Significant Height rose where it is clear the dominant significant height, 2 to 4 meters, and the dominant wave directions.

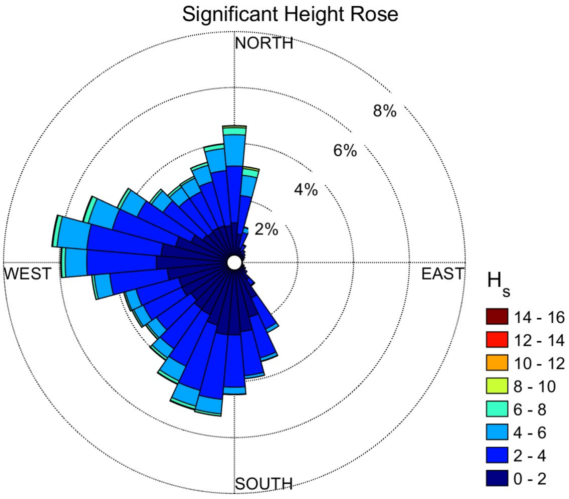

Figure 6.1: Significant height Rose.

6.2 Data Collection

In order to simulate the state of the sea in the mooring system of a FOWT, a certain number of sea states will be defined that will characterise the wave climate of that area. This approach is used because: assuming a constant state would not represent the wave climate due to its variability; it decreases the computational time compared with a dynamic model considering data from the last 30 years. Sea states are typically defined based on wave parameters such as significant wave height (H_s), peak wave period (T_p), and wave direction (θ). These interdependent parameters exhibit complex statistical relationships that require appropriate probabilistic modelling.

The wave and wind climate data were collected from "ERA5 hourly data on single levels from 1940 to present" (Hersbach et al., 2023). From the wide range of variables that could be extracted from ERA5, the chosen ones were according to the parameters to be computed in the project's next phase. In this case, the next phase will simulate the sea states in SWAN, and it is decided to admit a JONSWAP spectrum in the boundary conditions (Equation 3.7). Therefore, the following parameters for wave climate and wind data were collected:

- Product Type: Reanalysis;
- Wind Variables:
  - U_{10}: horizontal speed of air moving towards the east, at a height of 10 m above the surface of the Earth, in metres per second;
  - V_{10}: horizontal speed of air moving towards the north, at a height of 10 m above the surface of the Earth, in metres per second.
- Waves Variables :
  - H_s: average height of the highest third of surface ocean/sea waves generated by wind and swell. It represents the vertical distance between the wave crest and the wave trough;
  - T_p: period of the most energetic ocean waves generated by local winds and associated with swell;
  - T_{m10}: average time it takes for two consecutive wave crests, on the surface of the ocean/sea, to pass through a fixed point;
  - θ: mean direction of ocean/sea surface waves;
  - ε: indicates whether waves (generated by local winds and associated with swell) are coming from similar directions or from a wide range of directions.

Reanalysis combines model forecasts with global observations using data assimilation to produce a consistent, physically based dataset. Unlike real-time forecasting, it operates without time constraints and at lower resolution, allowing the integration of more observations—including reprocessed historical data—for improved long-term accuracy and continuity (Hersbach et al., 2023).

Regarding the bathymetry of the study area, the study used the EMODnet (European Marine Observation and Data Network) information (EMODnet Bathymetry Consortium, 2024). EMODnet provides high-resolution, harmonised bathymetric data across European waters, compiled from hydrographic surveys and publicly available datasets. The bathymetry of this area ranges from 200 to 350 m, including areas at the 100 m level nearshore. The representation of its bathymetry can be found in Figure 6.8.

Before defining the sea states, the wind velocity variables and the mean wave direction were processed. The mean wave direction, originally in nautical coordinates, was adjusted by subtracting 90° to ensure a continuous representation. The wind velocity components were converted into two variables: magnitude and direction. The wind direction was then aligned with the same coordinate system as the wave direction (Figure 6.2).

6.3 Sea State Definition

Usually, 2D histograms are used to determine the sea states (Astariz et al., 2015; Perez-Collazo et al., 2014), however this technique limits the number of variables that can be tested (normally H_s and T_p). A way of surpassing this problem is by using statistical modelling to determine the sea states. First, a joint probability distribution is created (using a Copula function), and then new sea states are created according to that function (using Monte Carlo). The dataset point used to determine the sea states was 61.4° N and 3° E, as it is a borderline point that will then be used as a boundary condition to generate the wave field forward.

Even though all variables will be used for simulation, not all fit in a joint probability distribution. For that, the correlation between all sea states is calculated to determine the best way to model these variables.

The statistical dependence of variables can be computed with the Spearman correlation coefficient. The Spearman rank correlation coefficient, denoted as ρ_s, is a non-parametric measure of the strength and direction of association between two ranked variables. Unlike the Pearson correlation coefficient, which assesses linear relationships, the Spearman coefficient evaluates monotonic relationships, whether linear or not. This coefficient ranges from -1 to 1, with zero indicating that there is no relationship between variables and the higher absolute values indicating a stronger relationship between the variables (Wilks, 2006). This coefficient is given by:

$$\rho_s = 1 - \frac{6\sum d_i^2}{p(p^2-1)} \tag{6.1}$$

where d_i is the difference between the ranks of each observation, and p is the number of observations.

A strong correlation is given for ρ_s higher than 0.6 (Wilks, 2006). Table 6.1 presents the correlation matrix for the variables mentioned above. The conclusions that can be taken from this is: θ, θ_{wind} and ε do not correlate with the other variables (negative or near null values in every column and row corresponding to them); T_{m10} has a good correlation with H_s and T_p, as expected; and U_{wind} has excellent correlation with H_s.

Table 6.1: Spearman's Correlation Matrix.

	H_s	T_p	θ	T_{m10}	U_{wind}	θ_{wind}	ε
H_s	1.000	-	-	-	-	-	-
T_p	0.427	1.000	-	-	-	-	-
θ	-0.201	-0.048	1.000	-	-	-	-
T_{m10}	0.627	0.862	-0.058	1.000	-	-	-
U_{wind}	0.752	0.037	-0.246	0.123	1.000	-	-
θ_{wind}	0.051	0.028	-0.110	0.049	-0.041	1.000	-
ε	-0.338	-0.235	-0.039	-0.263	-0.316	-0.014	1.000

A strong correlation suggests a robust interdependence between the variables, necessitating a joint probabilistic model (Wilks, 2006). Conversely, a weak correlation allows for independent modelling. The variables that will be modelled jointly are: H_s, T_p, T_{m10} and U_{wind}. The rest are going to be modelled independently.

6.3.1 Joint Probability Distribution - Copula Model

After deciding which variables are correlated, the joint probability distribution will be modelled. Creating such a distribution is a process that involves determining appropriate marginal distributions and combining them into a unified probabilistic framework. Table 6.2 specifies the distributions assumed for this part.

Table 6.2: Distributions used for each variable.

Variable	H_s	T_p	T_{m10}	θ	U_{wind}	θ_{wind}	ε
Distribution	Lognormal	Lognormal	Lognormal	Kernel	Normal	Kernel	Kernel

Figure 6.2 shows the fit of each distribution to the histogram of observed points. For H_s, T_p, T_{m10} and U_{wind} the distributions is given according to Li et al. (2013). However, the direction of the wind and waves cases didn't have a clear distribution, meaning that it would probably be a non-parametric distribution or a superposition of parametric distributions. The θ is given by a 3-peak normal distribution, but is assumed as a kernel to simplify. Thereby, θ_{wind} and ε were considered kernel aswell. A kernel distribution is a non-parametric representation of the probability density function (PDF) of a random variable that can be used when a parametric distribution cannot properly describe the data, or when you want to avoid making assumptions about the data distribution. A Kernel distribution is defined by a smoothing function and a bandwidth value, which control the smoothness of the resulting density curve (MathWorks, 2025). For all cases, the Kernel distribution worked well. It is important to mention that ensuring accurate fitting is critical, as errors in the marginal distributions propagate into the joint model and subsequent simulations.

6.3.1.1 Copula Model

In order to create a unified distribution, a Gaussian Copula model will be used. Copulas are functions that describe dependencies among variables and provide a way to make distributions that model correlated multivariate data. A multivariate distribution can be created by specifying marginal univariate distributions and choosing a copula to provide a correlation structure between variables.

The copula matrix is given by:

$$Co(u_1, u_2, \ldots, u_n) = \Phi_R\left(\Phi^{-1}(u_1), \Phi^{-1}(u_2), \ldots, \Phi^{-1}(u_n)\right) \tag{6.2}$$

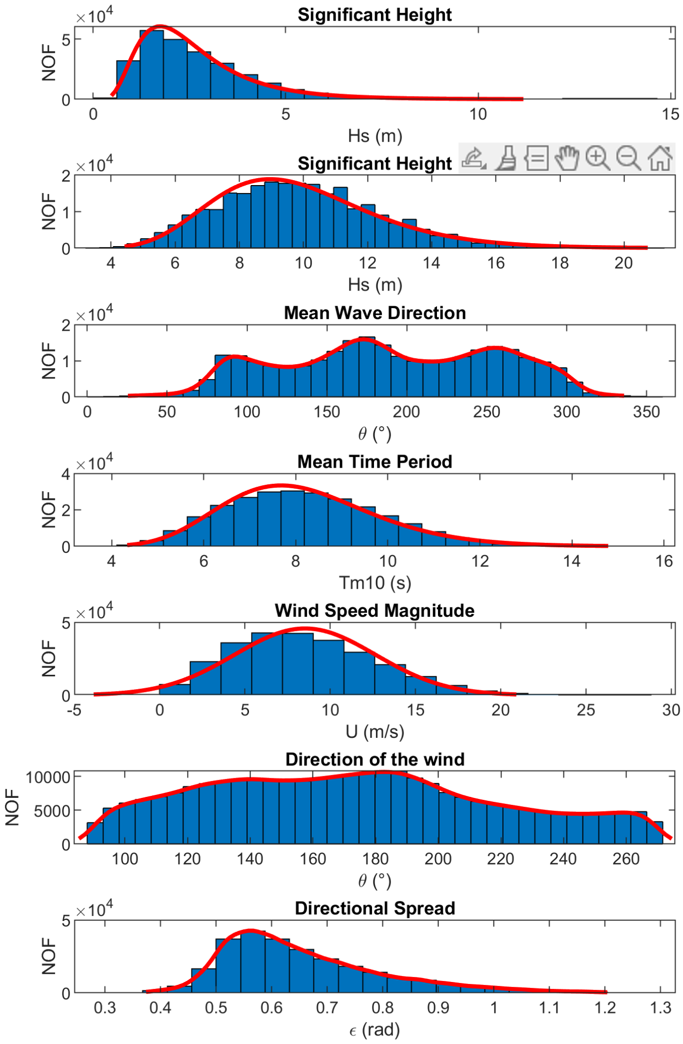

Figure 6.2: Probability density function of the observed states.

where $u_i = F_i(t_i)$ is the marginal probability of default by time t_i, Φ^{-1} is the inverse CDF of the standard normal distribution, and Φ_R is the CDF of the multivariate normal distribution with correlation matrix R. Table 6.3 shows the copula matrix for this study.

In addition, the Gaussian copula is often favoured for its mathematical tractability, ease of implementation, and compatibility with existing techniques for multivariate normal distributions. It has been extensively used in finance, particularly in modelling credit risk, as seen in the influential work of, and in environmental sciences to represent spatial and temporal correlations (Deumic and Halmkrona, 2019).

Finally, to generate the sea states, the Monte Carlo method will be employed. This method allows for predicting variables given their statistical distributions and dependencies, enabling the simulation of the desired number of sea states. By repeatedly sampling from the joint distribution of wave parameters, the Monte Carlo simulation provides a robust framework for estimating the probabilistic behaviour of ocean conditions.

Table 6.3: Copula matrix.

	H_s	T_p	T_{m10}	U_{wind}
H_s	1.000	-	-	-
T_p	0.451	1.000	-	-
T_{m10}	0.647	0.871	1.000	-
U_{wind}	0.734	0.040	0.129	1.000

6.3.2 Sea State Generation

The last step of this section is the generation of the sea states. For that, the explanation on how the Monte Carlo approach retrieves the sea states and the number of sea states to be computed will be discussed.

From the copula matrix, a number of correlated standard normal vectors is created (5000 samples). Then it is applied the normal cumulative distribution function (CDF) to each component to get variables from 0 to 1. Finally, the inverse cumulative function is applied to each variable to convert the uniform variables into simulated values.

This technique is called resampling and is based on constructing artificial data sets from a given collection of real data. The main advantage of this method is its non-reliance on assumptions regarding the underlying parametric distribution of the data or the sampling distribution of the test statistic (Wilks, 2006).

Moreover, resampling techniques apply to both scalar and vector-valued data. In the scalar case, each observation consists of a single numerical value, whereas in the vector case, each data point comprises multiple components reflecting the multidimensional nature of the phenomenon under study. This latter form is particularly advantageous in contexts where spatial correlation is relevant, as it allows each element of the data vector to correspond to a distinct spatial location. Consequently, the method is well-suited to capturing spatial dependencies that might otherwise be overlooked in scalar analyses (Wilks, 2006).

From the bigger sampling pool, a total of 30 sea states were selected to ensure a representative yet computationally manageable dataset using k-means. This number falls within the range recommended by DNVGL-OS-E301 (2018) for reliable analysis of marine operations. These sea states are listed in Table A.2, and Figure 6.3 visualises the distribution of these states across four key parameters: significant wave height (H_s), peak period (T_p), wave direction (θ), and wdirectional spreading (ε).

It is important to remember that the directions are given in nautical convention and that the figures that involve these parameters are adjusted by 90º to be continuous in the figures.

Finally, the frequencies were calculated by assessing the influence of each generated sea state in the Significant Wave Height/Peak Period (H_s/T_p) space. This was accomplished by computing the Euclidean distance between each generated point and all observed points, resulting in an $N \times M$ distance matrix, where N is the number of generated sea states and M is the number of observed sea states. Each observed point was then associated with the index of its nearest generated point. The number of observed points linked to each generated sea state was subsequently counted and

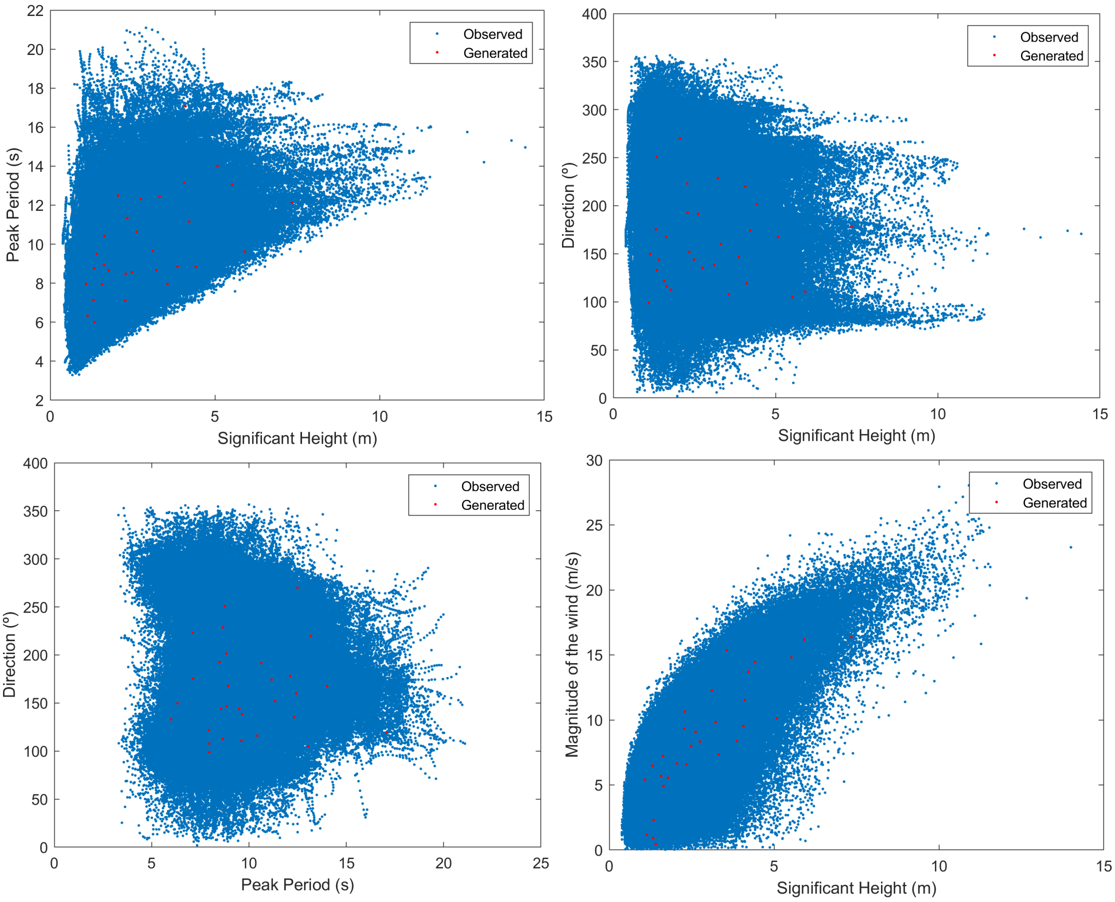

Figure 6.3: Representation of the generated sea states in different dimensions.

normalised by the total number of observations, yielding the frequency of occurrence for each generated sea state (Table A.1).

6.4 Simulation Scenarios

This section outlines the process used to define the different cases evaluated in the fatigue analysis of a co-located Wave Energy Converter and Floating Offshore Wind Turbine system. The focus is on assessing the influence of various spatial configurations. First, the parameters selected for study are discussed, followed by a description of how the simulations were chosen using a Design of Experiments (DoE) approach—specifically, the Taguchi method.

6.4.1 Parameters

Considering the wide range of aspects involved in the co-location of WECs and FOWTs, numerous variables could be analysed. These include the number of WECs, their spatial arrangement, the use of multiple WEC layers, array orientation, the distance between WECs and the FOWT, and the layout pattern (e.g., linear or curved configurations), among others.

For the purposes of this study, the parameters selected were: the number of WECs; the distance between the WEC array and the FOWT; the spacing between individual WECs; and the direction (orientation) of the array. These parameters were chosen based on insights from the relevant literature and the specific characteristics of the present analysis—for example, the consideration of more than one wave direction.

Subsequently, the levels of each parameter were selected as follows:

- Number of WECs: 1, 3, 5, 7.

  These values were chosen to ensure symmetry around the FOWT and always to include one WEC directly facing the FOWT, starting from one and iteratively adding 2;

- Distance FOWT-WEC: 120 m, 220 m, 270 m, and 420 m.

  The minimum distance was based on Clark and Paredes (2018) configuration using the lower distance in the literature reviewed. 100 m increments defined further levels;

- Distance WEC-WEC: 198 m, 220 m, 320 m, 420 m.

  Carballo and Iglesias (2013) stated that the minimum distance between WECs should be 2.2*D* (where D = 90 m), resulting in 198 m. The additional levels were created by increasing the distance by 50 m.

- Angle of WEC array relative to FOWT: 180º, 250º, 270º, 350º.

  These angles are given in nautical coordinates and represent the three peaks of occurrence of the direction of waves, plus the case where the WEC array is facing West.

6.4.2 Design of Experiments

According to the previous section, four parameters will be studied with four levels each. If a full factorial approach were used—where every possible combination of parameter levels is simulated—it would require a total of $4^4 = 256$ simulations. While this method ensures complete coverage of the design space, it is computationally unfeasible given the high number of simulations required.

To address this challenge, a more efficient strategy was adopted: the Design of Experiments (DoE). DoE is a structured, statistical approach used to plan experiments to maximise the amount of information gained while minimising the number of simulations or tests. It allows researchers to systematically investigate the effects of multiple variables and their interactions on a given outcome (Ingram et al., 2011).

Among the various DoE approaches, the Taguchi method was selected. This method employs orthogonal arrays to study the main effects of multiple parameters using a reduced number of simulations. It is particularly recognised as a signal-enhancing method, which aims to amplify the influence of the factors (signal) while reducing the impact of uncontrolled variation (noise). By emphasising these causality relationships through the design matrix, the Taguchi method helps improve the system's robustness under study.

Table 6.4: Taguchi Orthogonal Array applied to the study.

Simulation	N.WECs	Distance FOWT-WEC [m]	Distance WEC-WEC [m]	Angle [º]
0	0	-	-	-
1	1	120	198	180
2	1	220	248	250
3	1	320	298	270
4	1	420	348	350
5	3	320	348	250
6	3	420	298	180
7	3	120	248	350
8	3	220	198	270
9	5	420	248	270
10	5	320	198	350
11	5	220	348	180
12	5	120	298	250
13	7	220	298	350
14	7	120	348	270
15	7	420	198	250
16	7	320	248	180

This methodology is consistent with guidelines outlined in the EquiMar protocols (Ingram et al., 2011), which support structured experimental design for marine renewable energy systems.

Table 6.4 is the result of the application of the L16 orthogonal array of the Taguchi method, and simulation 0 represents the baseline. The visual representation of this simulations are in Figures 6.4,6.5,6.6, and 6.7. The red dot represents the FOWT and the blue line the WECs.

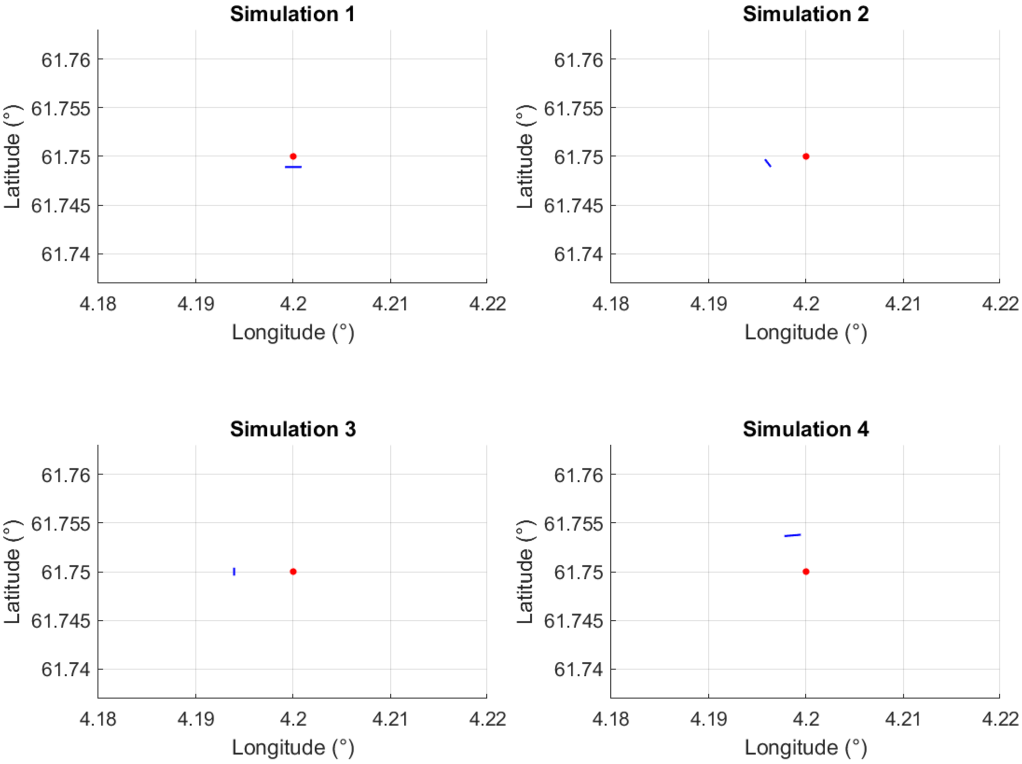

Figure 6.4: Visual representation of the simulation's configuration. Simulation 1 to 4.

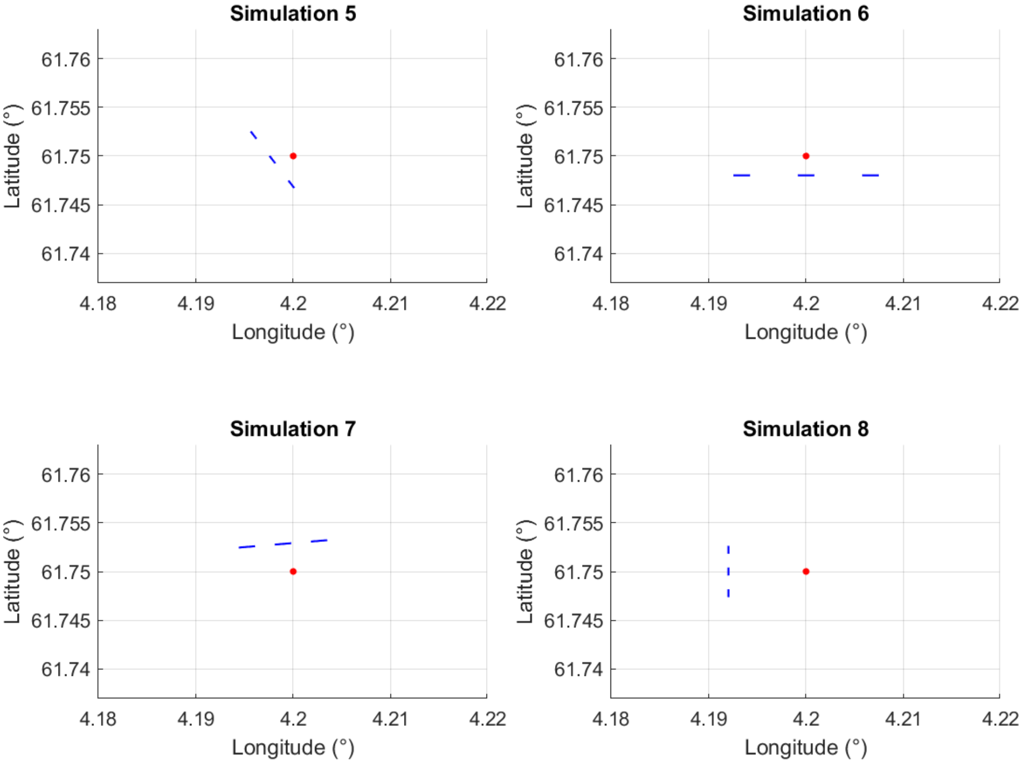

Figure 6.5: Visual representation of the simulation's configuration. Simulation 5 to 8.

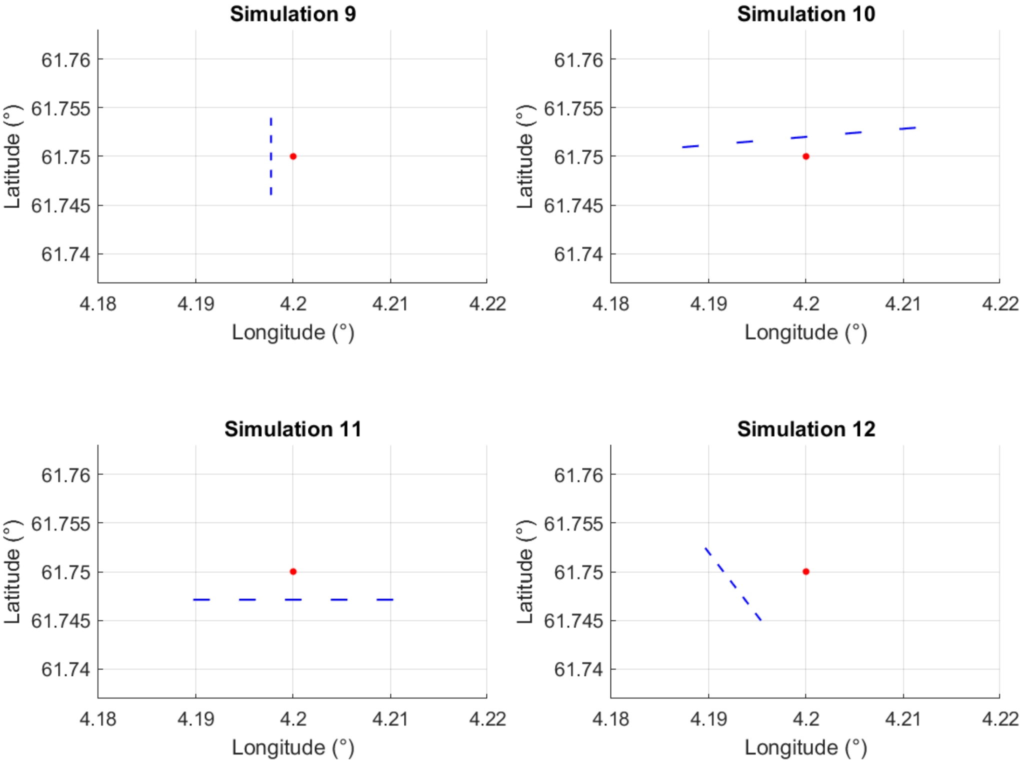

Figure 6.6: Visual representation of the simulation's configuration. Simulation 9 to 12.

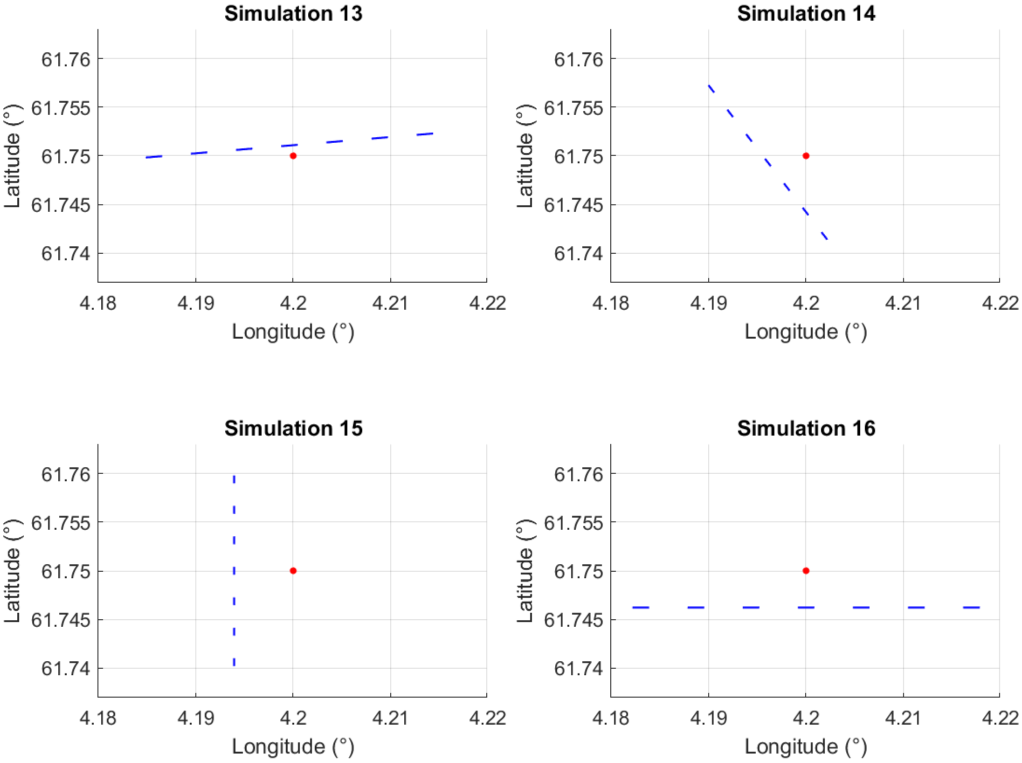

Figure 6.7: Visual representation of the simulation's configuration. Simulation 13 to 16.

6.5 Simulations Workflow

6.5.1 SWAN

The first stage of the simulation process involved modelling the wave environment using the SWAN model, version 41.51. This software was selected for its capability to simulate spatially varying wave fields in coastal and offshore regions, incorporating complex bathymetry and directional wave spectra.

The computational domain was defined using a structured rectangular grid with a spatial resolution of $1 \times 10^{-4\circ}$ in longitude (approximately 55.5 m) and $5.2 \times 10^{-4\circ}$ in latitude (approximately 57.9 m). The grid resolution and physical settings were validated against previous studies using similar configurations (Clark and Paredes, 2018) and ensure accurate representation of the spatial variability of the wave field and adequate capture of the layout and interactions of the WECs. Bathymetric data within the domain was obtained from EMODnet (Figure 6.8).

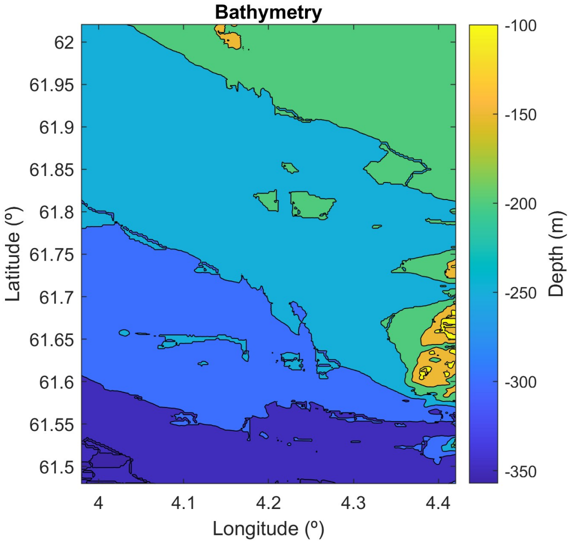

Figure 6.8: Bathymetry of the area of study.

All coordinates were defined in nautical convention, consistent with the data sources used throughout the study.

A stationary wave field was selected to reduce computational cost while still capturing the representative wave conditions for each sea state, and the input spectrum in the boundary points was defined using the JONSWAP formulation. The enhancement factor was calculated for each sea state (Equation 3.8), and the input parameters included significant wave height (H_s), peak period (T_p), mean wave direction (θ), and directional spreading (ε). The wind field is included by defining the wind magnitude and direction.

Furthermore, identical boundary conditions were applied on all sides of the domain to ensure a fully developed wave field and avoid artificial reflections or empty zones.

The model configuration included key physical processes such as third-generation wave growth (GEN3), wind input using Wu's formulation (DRAG WU), wave breaking, bottom friction, and wave steepness limitation (LIM). These settings enabled a realistic simulation of wave transformation and energy dissipation across the domain. However, triplet and quadruplet interactions were disabled.

The WEC used in this study is the WaveCat, previously described in Section 4.2. Its selection was based on the availability of empirical transmission and reflection coefficients and its demonstrated performance in co-location scenarios. In the SWAN simulations, the WaveCat was represented using a transmission coefficient of 0.80 and a reflection coefficient of 0.45, in accordance with the values reported by Fernandez et al. (2012). These coefficients were applied to model the WEC's influence on the wave field and its subsequent impact on the FOWT mooring system.

This device is 90 m long, and to optimise the representation of the WECs as obstacles, the grid resolution in the area of influence was chosen to be approximately equal to the characteristic dimension of the WEC. This ensured that the WECs were adequately resolved within the computational mesh. Care was taken to avoid placing WECs directly on grid nodes, which was managed through a MATLAB script that calculated the precise location of the ends of the WEC based on the defined configuration.

6.5.2 WEC-Sim and Moody

The next step of the simulation is quantifying the tensions and motions of the FOWT through a coupled time-domain simulation approach. The platform motion and hydrodynamic response were modelled using WEC-Sim, while the dynamic behaviour of the mooring system was captured with MooDy. Both programs are MATLAB toolboxes, and the versions used are WEC-Sim v3.0-MooDy with MATLAB R2017b.

The simulation setup is configured through the *wecSimInputFile.m* script, which defines global simulation parameters, wave characteristics, hydrodynamic body data, and mooring configuration.

Simulation parameters

The simulation time was set to 11,600 s (3 hours as DNVGL-OS-E301 (2018) suggests for fatigue damage analysis), with a ramp-up period of 600 s to eliminate transient effects. A fixed time step of 0.05 s was used for solvers and data exchange.

Wave Characteristics

The wave conditions were defined using a MATLAB script which applied cubic interpolation to the 1D spectra at the FOWT location generated by SWAN. This process transformed the original set of 38 output frequencies into 4500 discrete frequency bins (Figure 6.9). Although Ruehl et al. (2024) recommends using approximately 1000 bins, preliminary tests revealed signal repetition, likely due to the simulation duration. This issue was not observed for shorter simulation periods. To ensure accuracy, a convergence study was conducted (Appendix B), and 4500 bins were ultimately adopted as the optimal resolution.

Importing the spectra—rather than assuming a predefined spectrum—allows the wind field effects to be captured, which would otherwise be neglected. In the current version of WEC-Sim, assigning a specific direction to each frequency is impossible. Therefore, the mean wave direction at the location is used.

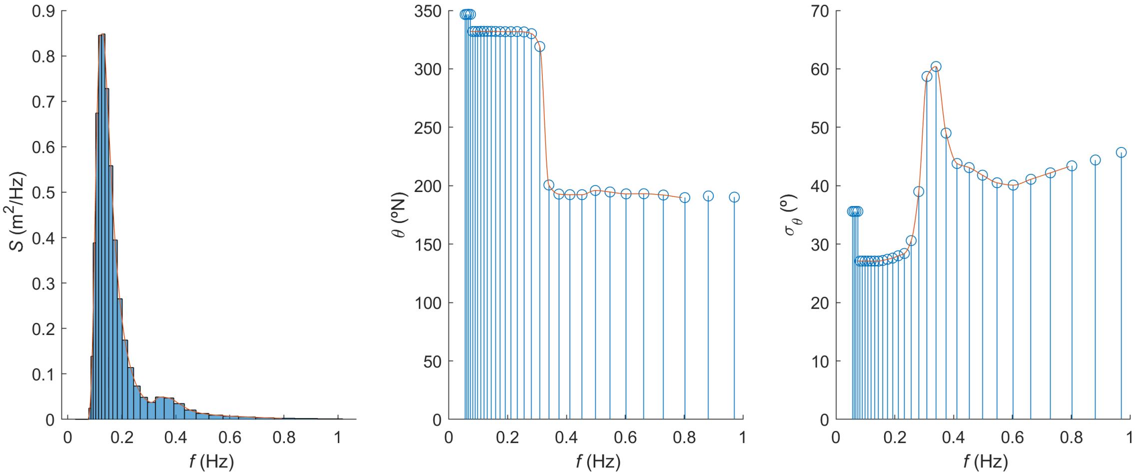

Figure 6.9: Example of interpolation of a sea state for frequency, direction and spread.

In Figure 6.9 (centre and right), the blue dots represent the outputted discretised frequencies, and the red line is the set of interpolated points. The set of points does not include the higher frequencies because the model (WEC-Sim) only evaluates the effects from 0.01 Hz to 0.8 Hz.

Hydronamic Body Data

The floating platform was modelled as a single rigid body in WEC-Sim. Hydrodynamic coefficients, including added mass, radiation damping, and wave excitation forces, were imported from a precomputed .h5 file generated using WAMIT. This file was provided by Clark and Paredes (2018) and is consistent with validated data from the OC5 project. A corresponding .ast geometry file was also provided and used for visualisation purposes within the SimMechanics Explorer.

WEC-Sim is a linear radiation and diffraction simulation tool for WECs, developed using MATLAB and Simulink. It relies on hydrodynamic coefficients generated by potential flow solvers such as WAMIT or NEMOH. Therefore, WEC-Sim does not account for second-order wave drift forces.

Table 6.5 summarises the key parameters used for FOWT modelling.

The platform was also constrained to allow only surge, heave, and pitch motions via a floating joint. Its initial displacement was set to $[0, 0, -0.45]$ m.

Mooring Configurations

The FOWT was moored using three catenary chain lines arranged at 120° intervals. Each mooring line was modelled in MooDy and discretised into 10 finite elements with a polynomial order $p = 5$, allowing for high-fidelity capture of dynamic effects such as snap loads and bending.

Table 6.5: Properties of the Floating Wind Turbine (Robertson et al., 2017).

Parameter	Value
Mass [kg]	1.4265×10^7
Roll Inertia [kg·m^2]	1.3947×10^{10}
Pitch Inertia [kg·m^2]	1.5552×10^{10}
Yaw Inertia [kg·m^2]	1.3692×10^{10}
Displacement [m^3]	1.3917×10^4
Center of Gravity [m]	-8.07 (z-direction)
Center of Buoyancy [m]	-13.18 (z-direction)

The mooring configuration was defined in the *mooring_system.m* script, also provided by Clark and Paredes (2018). In Tables 6.6 and 6.7, the characteristics of the mooring cables and the mooring system are presented, respectively. The equivalent line diameter listed in Table 6.6 is the diameter of a uniform circular cable made of the same material, with the same mass and submerged weight per unit length as the chain. It is a parameter used by MooDy and other mooring codes to estimate the hydrodynamic forces acting on mooring chains.

Table 6.6: Properties of the Mooring Chain (Robertson et al., 2017).

Parameter	Value
Link diameter [m]	0.0766
Equivalent line diameter [m]	0.1427
Axial stiffness EA [N]	7.536×10^8
Mass per unit length [kg/m]	113.35
Submerged weight [N/m]	1065.7
Added mass coefficient	1.0
Hydrodynamic drag coefficient	1.1
Seabed drag coefficient	1.0

Table 6.7: Properties of the Mooring System (Robertson et al., 2017).

Component	Position $[X, Y, Z]$ (m)
Anchor 1	(837.6, 0.0, -200.0)
Anchor 2	(418.8, -725.4, -200.0)
Anchor 3	(418.8, 725.4, -200.0)
Fairlead 1	(40.9, 0.0, -14.0)
Fairlead 2	(20.4, -35.4, -14.0)
Fairlead 3	(20.4, 35.4, -14.0)
Unstretched cable length [m]	835.5

A sequential one-way coupling strategy was used between WEC-Sim and MooDy. Platform motions computed in WEC-Sim were passed to MooDy at each time step to calculate the corresponding mooring line response. This approach enabled high-resolution tension data to be extracted at the fairlead without requiring a fully coupled solver architecture.

6.5.3 WAFO

This section describes the methodology to estimate the fatigue damage experienced by mooring chains in floating offshore wind turbine (FOWT) simulations. The process employs rainflow counting using the WAFO toolbox (version 2017.1) in MATLAB R2017b. The analysis uses time-domain tension data extracted from numerical simulations and empirical S-N fatigue curves from DNVGL-OS-E301 (2018) for studless chain links. This methodology follows Clark and Paredes (2018) to determine fatigue damage.

Firstly, the tension time series of the three cables from MooDy is imported, and the first 600 s of data are discarded to eliminate the transient effects. Assuming a sampling interval of 0.5 s, this ensures only the steady-state response is analysed. Then, rainflow counting is applied as explained in subsection 4.1. Subsequently, the nominal stress range is calculated by converting the force range to stress using the cross-sectional area of the mooring chain, where the diameter is the link diameter (Table 6.6). Furthermore, fatigue life N (in cycles) is estimated using a power-law S-N relationship from Equation 4.4. The material selected is Studless chain (open link) with $a = 6 \times 10^{10}$, and $m = 3$.

Finally, unit fatigue damage is computed using Miner's Rule (Equation 4.3). In order to compute the fatigue damage over 1 year the following parameters are used:

- One year contains 365.25 days;
- Each day is divided into eight three-hour sea-states;
- Total number of sea-states per year is:

$$n_{\text{seas}} = 365.25 \times 8 = 2922 \tag{6.3}$$

- The sum of the probability of each sea state must be one (Table A.1).

The fatigue damage for each sea state over the year is computed as:

$$D_{\text{year},j} = D_{\text{unit},j} \cdot p_j \cdot n_{\text{seas}} \tag{6.4}$$

Where j indicates the index of the sea state.

And the total fatigue is given by the sum of $D_{\text{year},j}$ for each cable. In this context, the design life of the FOWT is considered to be 20 years (as in Clark and Paredes (2018)).

6.6 Statistical analysis

To assess the influence of the design parameters on the fatigue life of the mooring system, an Analysis of Variance (ANOVA) was conducted. The primary objective was to quantify the relative contribution of each design factor to the variation in fatigue damage and identify those that significantly affect fatigue performance. Additionally, a Signal-to-Ratio (S/N) ratio analysis is conducted as part of the Taguchi methodology.

ANOVA is a statistical method that separates the total variability in a response variable into components attributable to different explanatory factors. This study employed it to determine which variables most significantly influence the fatigue life of mooring lines, based on the outputs from numerical simulations.

The factors and levels are described in the Simulation Scenarios section, including four parameters and four levels, giving a total of 16 simulations (Table 6.4). The value analysed by ANOVA is the total damage by the fatigue per simulation per cable (Table 7.6).

6.6.1 ANOVA Implementation

A multi-factor ANOVA was performed using MATLAB. Each factor was treated as a fixed effect, and interaction terms were neglected for simplicity. The analysis yielded the following statistical indicators:

- P-values, indicating the statistical significance of each factor (significant if $p < 0.05$);
- Sum of Squares (SS), representing the portion of total variance explained by each factor;
- Percentage Contribution, showing the relative importance of each factor in influencing fatigue damage;

Finally, factors with statistically significant p-values were interpreted as having a meaningful effect on fatigue performance. The percentage contribution helped identify the most influential parameters.

6.6.2 S/N Ratio

The Signal-to-Noise (S/N) ratio is a key metric in the Taguchi method, used to evaluate the robustness of a system by quantifying the variability in performance relative to the desired outcome. In the context of fatigue analysis, a higher S/N ratio indicates more consistent and reliable performance under varying sea states, which is desirable for mooring system design.

The S/N ratio transforms the variability in the response variable into a single metric, allowing for straightforward comparison across different design configurations. For fatigue damage, the goal is to minimise the response (i.e., damage), and the corresponding equation is:

$$\mathrm{S/N} = -10\log_{10}\left(\frac{1}{n}\sum_{i=1}^{n} D_{\mathrm{year},i}\right) \tag{6.5}$$

where $D_{\mathrm{year,i}}$ represents the observed fatigue damage in the i-th simulation, and n is the number of observations. This formulation penalises variability and higher damage values, thereby favouring configurations that yield lower and more consistent fatigue damage.

Chapter 7

Results and Discusssion

This chapter presents the results and discussion of the simulation workflow, organised according to the chronological application of each tool. The analysis begins with the Wave Field modelling using SWAN, followed by the evaluation of Dynamics in FOWTs through WEC-Sim, and the Dynamics in Mooring Lines using MooDy. The final section focuses on Fatigue Analysis performed with WAFO. Additionally, the chapter includes an interpretation of the statistical analyses conducted throughout the process.

Each analysis begins with Simulation 0, the baseline case without WECs, serving as a reference point. Subsequent simulations are then compared against this baseline to identify deviations, highlight anomalous results, and support a critical discussion of the observed trends.

7.1 Wave Field

All sea states were simulated as stated in Table A.2, and the results were tables with properties at the FOWT location, 1D spectra at the boundary and at the FOWT location. Apart from that, H_s, T_p and θ were calculated for all points of the grid for visualisation.

The analysis begins with a comparison of input and output spectra. These present a slight decrease in energy at the peak frequency, as seen in Figure 7.1. A closer inspection reveals the influence of the wind field in the spectra, coming as a low-energy peak at frequencies higher than the peak frequency. While this does not represent a significant change in the spectrum, it is an important phenomenon to consider.

Moving next, the total variance of the spectrum in each sea state in m^2, the Significant Height, Peak Period and Direction were accessed for all simulations. The total energy is calculated by the MATLAB script that makes the interpolation to input into WEC-Sim. It calculates the total energy and the total energy truncated by the frequency limits in WEC-Sim. The values of simulation 0 (no co-location) are the ones going to be used for comparison with the further simulations. The equation to determine the difference for each variable compared to the baseline is the following (adapted from Monteiro, 2017):

$$\Delta X(\%) = \frac{X_{baseline} - X_{simulation}}{X_{baseline}} \cdot 100 \tag{7.1}$$

where X is the variable to study.

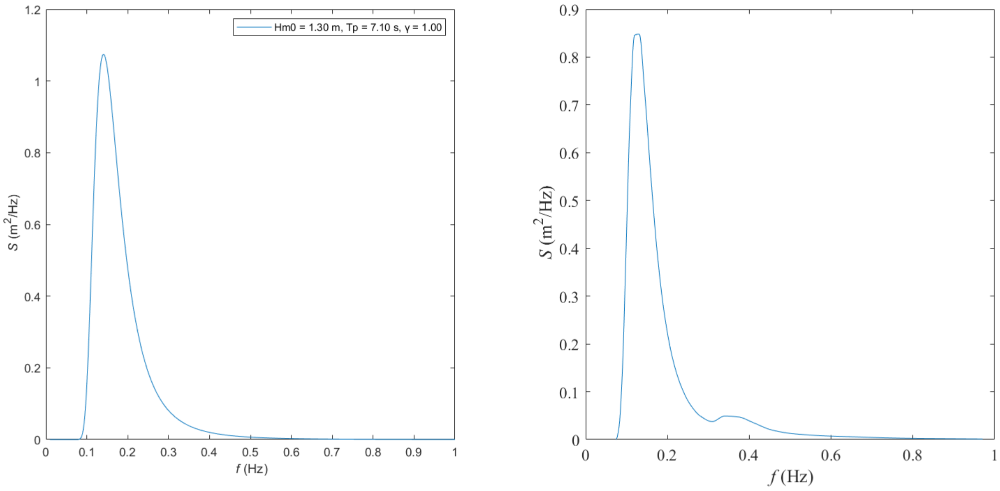

Figure 7.1: Representation of input spectra (left) and modified by conditions (right) of Sea State 1 for Simulation 0.

Regarding the total energy of each sea state influenced by the simulations, Figure 7.2 presents a heat map where warmer colours mean a higher energy decrease. In contrast, cooler means a lower energy decrease or even an increase.

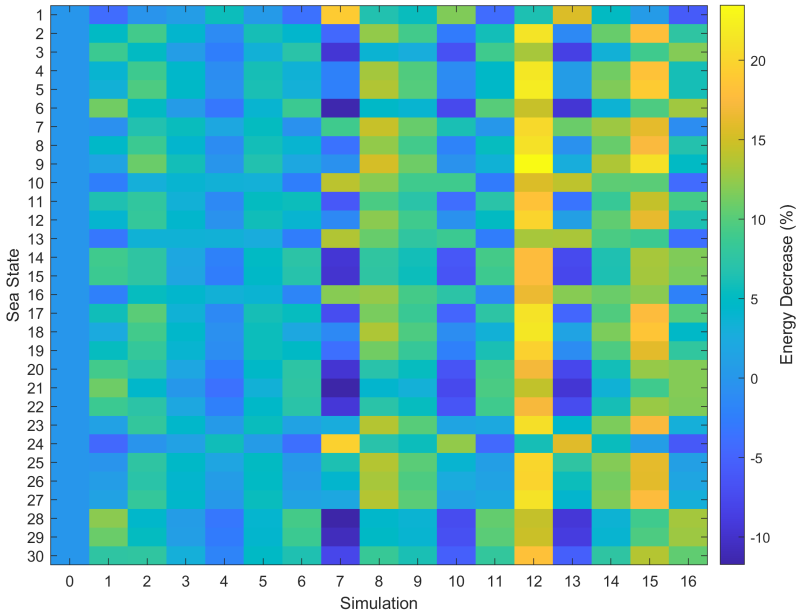

Figure 7.2: Heat map of the energy decrease, Δm_0, for all simulations and sea states.

It is clear from the Figure 7.2 that simulation 12 was the one with highest energy descrease ranging from 6.12 % to 23.47 % (Table 7.1) in sea states 24 and 9, respectively. This simulation accounted for 5 WECs, a distance FOWT-WEC of 420m, a distance WEC-WEC of 198 m and an angle of 250º. As a higher number of sea states were within the range of capture of this configuration, it is believed that this is a critical factor for the simulation's performance. Simulation 15 was a configuration that also had a reasonable energy decrease. The common factor was the angle the WEC array made to the FOWT. In this phase of the results, it is difficult to predict which variables at the levels will have more impact regarding the Design of Experiments method used. Nonetheless, the simulations using a 250º have a higher energy decrease. It is expected that in the statistical analysis, the angle will have a significant impact on the model.

The first four simulations, each involving a single WEC, display predominantly neutral colours in the results, indicating minimal variation in energy reduction. This suggests that a single WEC has a limited influence on the wave field through shadowing effects. These simulations also exhibit the lowest standard deviation values, as shown in Table 7.1, further supporting the observation of minimal impact.

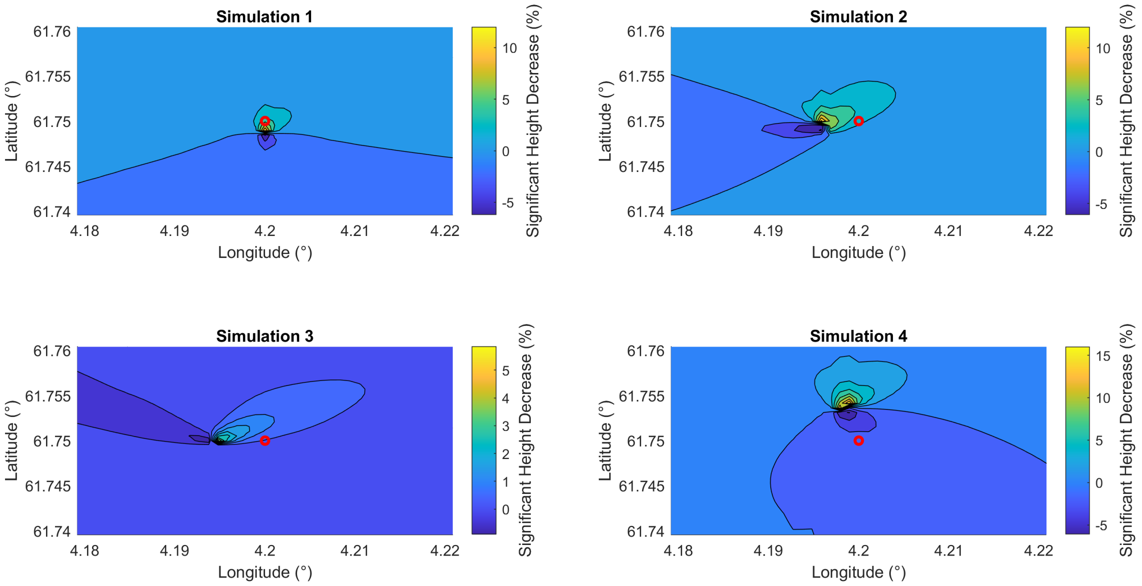

Figure 7.3: Significant height decrease in simulations 1, 2, 3, and 4.

Figure 7.3 illustrates the wave field response for sea state 9 in simulations 1 to 4. Appendix B provides additional visualisations for the remaining simulations. Moreover, simulations 5 through 16 demonstrate more consistent and predictable behaviour, as the WEC array forms a more effective barrier to incoming waves.

For the simulations that presented lower energy decrease, namely Simulations 7, 10, and 13. Simulations 7 and 10 exhibited negative mean energy decreases, despite showing a wide range of values. For instance, Simulation 7 ranged from -11.73% to 19.62% for sea states 21 and 24, respectively (Figure 7.4). Interestingly, the sea states that yielded the highest energy reductions in the best-performing simulations correspond to the worst outcomes in these cases. This suggests that the poor performance may be due to a misalignment between the wave direction (predominantly from the south or southwest) and the shielding orientation of the WEC arrays, which in these simulations faced north. In these simulations with energy increase, the common factor was the alignment of the WEC array with the FOWT, at 350º.

Table 7.1: Minimum, Maximum, Mean, and Standard Deviation for Energy Decrease for all simulations.

Simulation	$\Delta m_0, min$	$\Delta m_0, max$	$\bar{m_0}$	σ_{m_0}
1	-4.58	12.08	4.16	4.82
2	-0.27	10.89	6.70	2.65
3	0.13	5.92	3.13	1.61
4	-3.65	5.78	-0.28	2.49
5	0.42	6.62	4.63	1.49
6	-3.80	9.30	3.49	3.86
7	-11.73	19.62	-1.03	9.26
8	3.79	15.32	10.08	3.55
9	2.81	11.01	7.53	2.47
10	-7.51	12.40	-0.72	5.94
11	-4.31	10.67	4.63	4.49
12	6.12	23.47	17.67	4.17
13	-9.51	15.86	0.62	8.11
14	3.37	13.45	8.63	3.15
15	0.62	21.12	13.49	4.88
16	-5.93	13.13	5.85	5.93

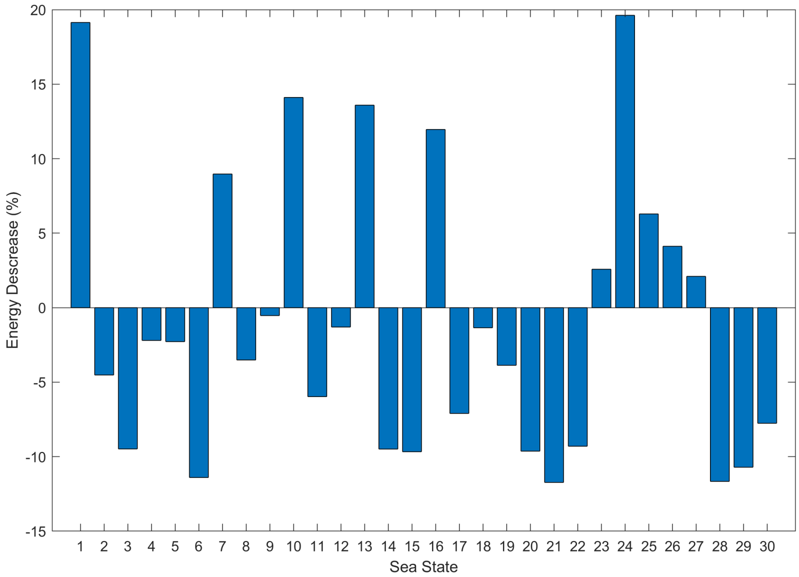

Figure 7.4: Energy decrease, Δm_0, of simulation 7.

When analysing the reduction in significant wave height, ΔH_s, a similar spatial pattern was observed when comparing to the energy one (Figure C.1 for comparison), due to the direct relationship between wave energy and significant height, as described by Equation 3.9. Therefore, the discussion on significant wave height reduction is inherently linked to the analysis of energy attenuation. In the case of the H_s reduction it ranges from -5.77 % to 12.48 %.

Moving on to the analysis of wave direction in the simulations, the percentage difference compared to the baseline ranged from -2.57% to 2.59%. In scenarios where the WEC array protects the west side, the wave direction tends to shift south, indicating an increase in angle. Conversely, when the array is positioned to the north, the waves tend to redirect further north. In other configurations—particularly the first four simulations—the impact on wave direction appears minimal, and no clear relationship between the influencing factors can be identified. This behaviour is illustrated in Figure 7.5.

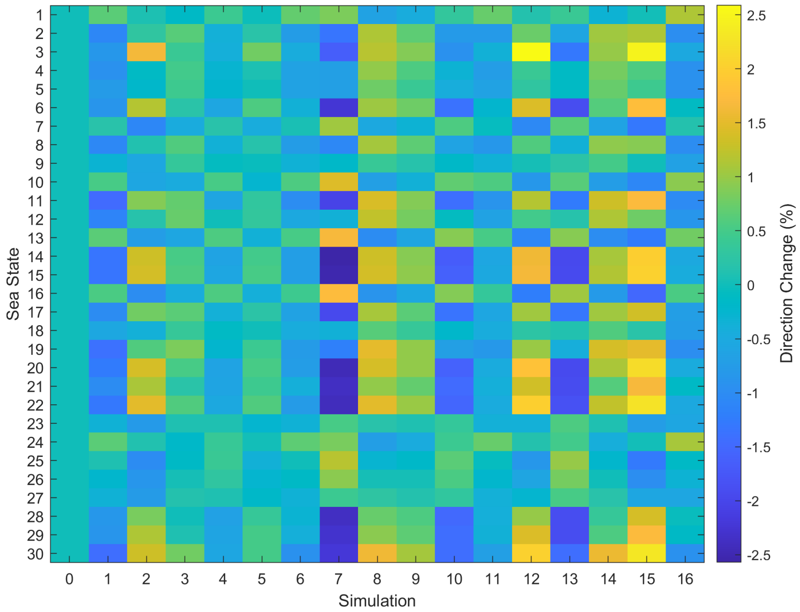

Figure 7.5: Heat Map of the direction change, $\Delta\theta$, for all simulations and sea states.

Finally, considering the peak period, T_p, it seems that it it is not affected by the simulation itself but according to the sea state. In almost all cases, it doesn't change except for sea states 11, 20, 21, 24, 27, 28, and 30. Analysing these sea states, it is not clear what relation they can have. It is essential to mention that even though these variables change, it is in a residual way from -0.21 % to 0.15%.

Before moving to the next phase of results corresponding to the WEC-Sim and MooDy results, a quantification of the energy discarded by the WEC-Sim limits was performed to assess whether it was critical. The analysis outcomes were that the energy discarded was residual, with a maximum of 0.0214 % and a minimum of 0.019 % of energy discarded, which is not significant.

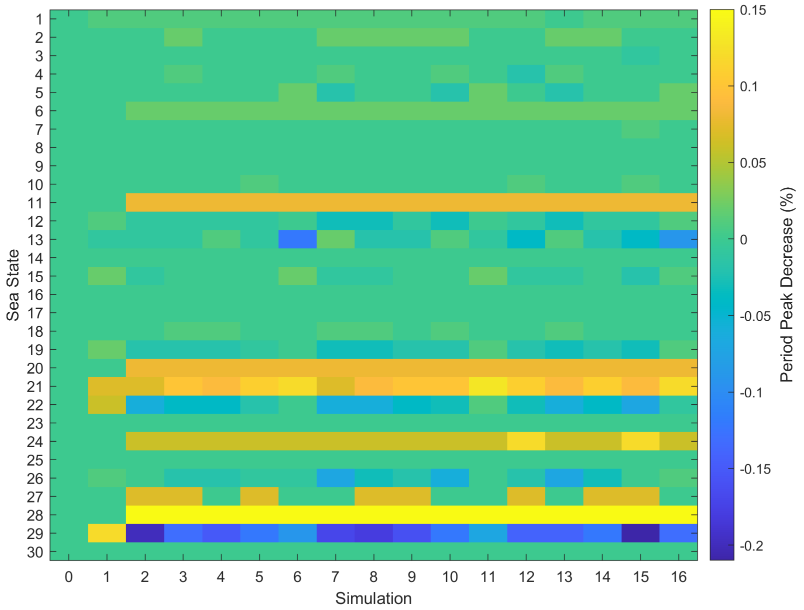

Figure 7.6: Heat Map of the peak period change, ΔT_p, for all simulations and sea states.

7.2 Dynamics in FOWT platform

Following the wave field characterisation, the dynamic response of the floating platform was analysed using time-series data generated by WEC-Sim. These outputs include platform motions and forces, evaluated across all sea states.

The primary motion components assessed were surge, pitch, and heave, along with the forces in the platform. Then, the minimum, maximum, root mean square (RMS), and standard deviation were computed for Simulation 0 — Table D.1 presents the surge, pitch, and heave standard deviation. From RMS and standard deviation, the magnitude of the motion and variability were measured.

The RAO was computed for each translational degree of freedom and sea state to identify the corresponding resonance frequencies, facilitating a clearer understanding of the platform's dynamic behaviour. As expected, the resonance frequencies remained relatively consistent across all sea states, indicating that they are primarily governed by the system's physical properties rather than environmental variability. Table 7.2 summarises the approximate resonance frequencies identified for each degree of freedom.

Table 7.2: Approximate Resonance Frequencies for Pitch, Surge, and Heave.

Degree of Freedom	Peak Frequency (Hz)	Peak Period (s)
Pitch	0.03	33.33
Surge	0.0088	113.63
Heave	0.057	17.54

It is expected that sea states with peak periods close to the resonance frequencies will induce larger motion amplitudes in the corresponding degrees of freedom. Table A.2 shows that none of the sea states align closely with the resonance frequencies for pitch and surge, suggesting that resonance effects in these modes are unlikely. However, for heave, sea states 24 and 27—with peak periods of 17.1 s and 14 s, respectively—are near the heave resonance frequency, indicating a potential for amplified vertical motion under these conditions.

7.2.1 Pitch

The pitch response to all sea states suggests an increase of pitch motion as significant height increases and to have higher values for sea states 23, 25, and 30 (Figure 7.7). These are sea states that have a high peak period, however, not close to the resonance frequency, not suggesting resonance. These values range from 0.36 mm to 9.3 mm of displacement, presenting low variability and absolute value.

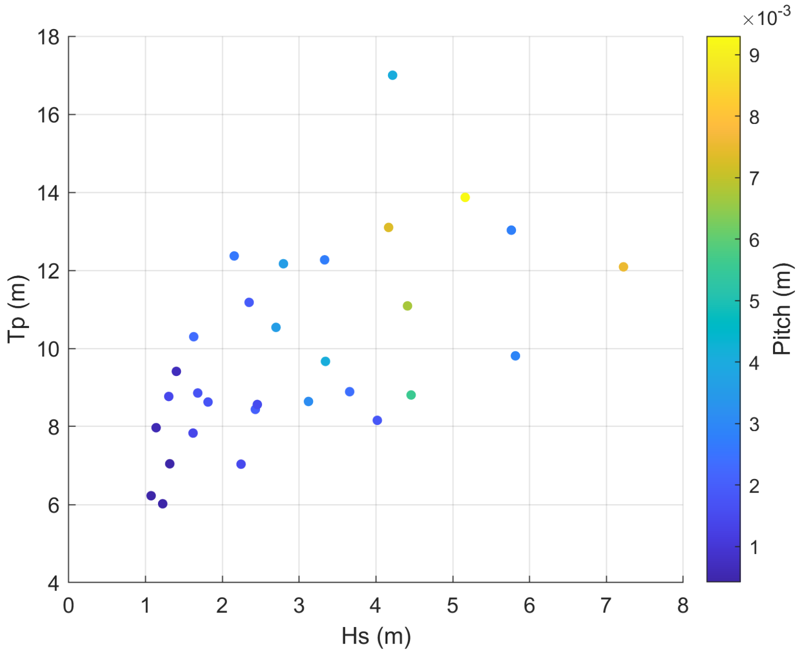

Figure 7.7: Pitch representation in Hs/Tp plane.

Figure 7.8 presents the pitch time series for Sea States 24, illustrating the platform's vertical response under this wave condition.

Moreover, the pitch motion observed in the other simulations generally tends to be slightly lower than the baseline case, except Simulations 7, 10, and 13. Conversely, Simulations 12 and 15 showed the most significant reductions in pitch RMS values (Figure 7.9). This pattern closely mirrors the trends in the wave field analysis, suggesting a correlation between significant wave height and pitch motion. In particular, simulations that experienced greater reductions in significant wave height also showed more pronounced decreases in pitch motion.

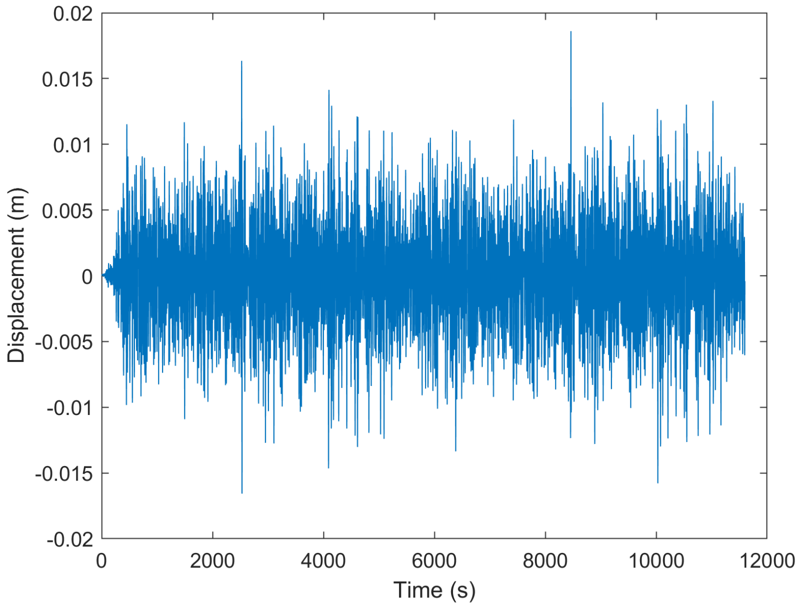

Figure 7.8: Representation of pitch time-series for Simulation 0 in sea state 24.

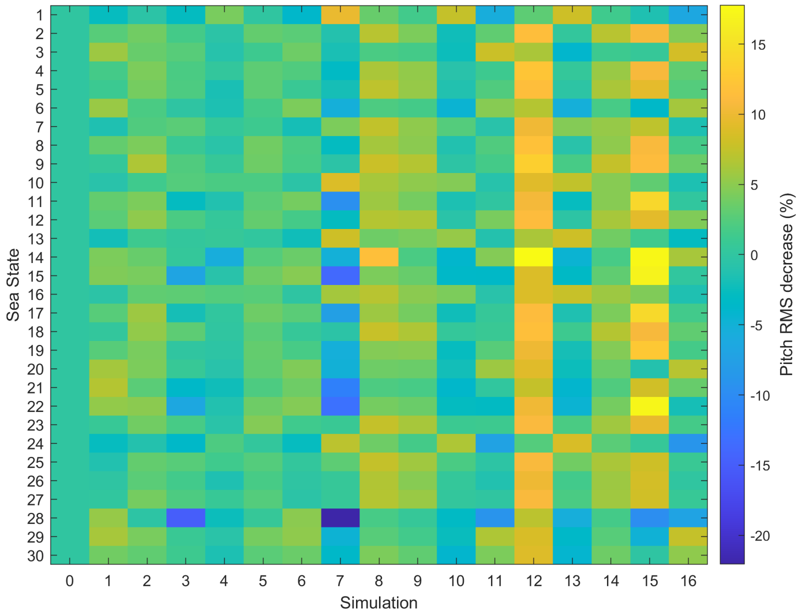

Figure 7.9: Heat Map of the pitch RMS for all simulations and sea states.

7.2.2 Surge

The surge response generally mirrored the pitch behaviour across all sea states (Figure 7.10). It suggests that surge also correlates with significant height, presenting an increase as significant height increases.

The sea states that presented higher pitch RMS values in the surge motion were 23, 24, 25, 27, and 30 (Figure 7.10). Among these, Sea State 27 recorded the highest surge displacement, reaching up to 2.7 m. The reason behind this is unclear, as the peak period of these sea states is not close to the resonance frequency. Nevertheless, such amplified surge motions may have a significant impact on mooring line tensions and, consequently, on the fatigue behaviour of the system. This is particularly relevant given that surge-induced loads are primarily governed by mooring stiffness, affecting the tension in these.

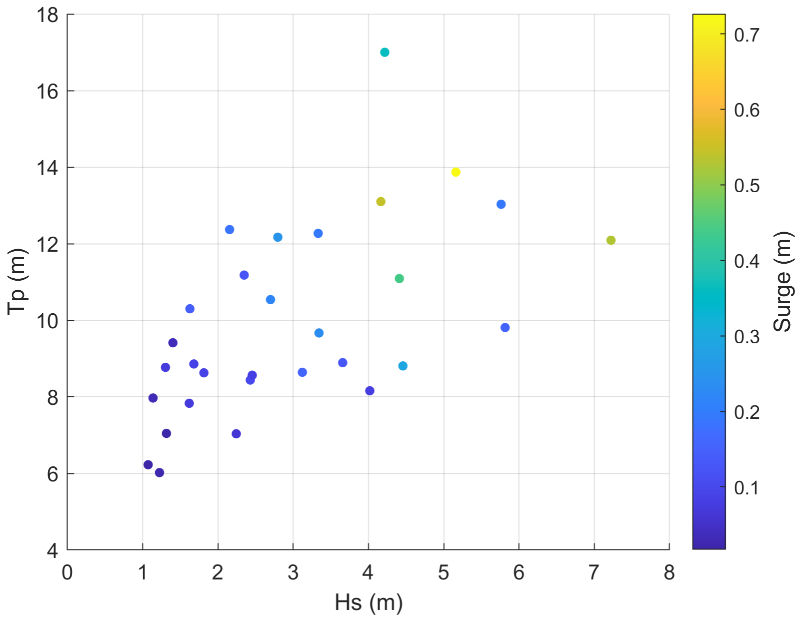

Figure 7.10: Surge representation in Hs/Tp plane.

It is important to note that second-order drift forces were not incorporated into the numerical model. Since surge motion is highly affected by these forces, the platform's behaviour in this degree of freedom may not be fully represented. Figure 7.11 displays the time series of the surge displacement in sea state 24.

When comparing the alternative simulations, a general trend of reduced surge motion is observed. Notably, Simulations 8, 9, 12, 14, and 15 showed a more pronounced decrease in surge amplitude (Figure 7.12). This reduction might be explained by the alignment between the incident wave direction and the orientation of the WECs, resulting in higher reductions. Adversely, Simulations 7, 10, and 12 demonstrated an increase in surge motion, consistent with the trend observed in pitch behaviour.

These findings underscore the importance of WEC orientation in influencing platform dynamics and highlight its potential impact on motion behaviour across different sea states. Furthermore, the effects of the WECs become more pronounced from Simulation 7 onward, where three or more devices are included. This supports the conclusion that a greater number of WECs forms a more consistent hydrodynamic barrier, contributing to a more effective reduction in platform motion.

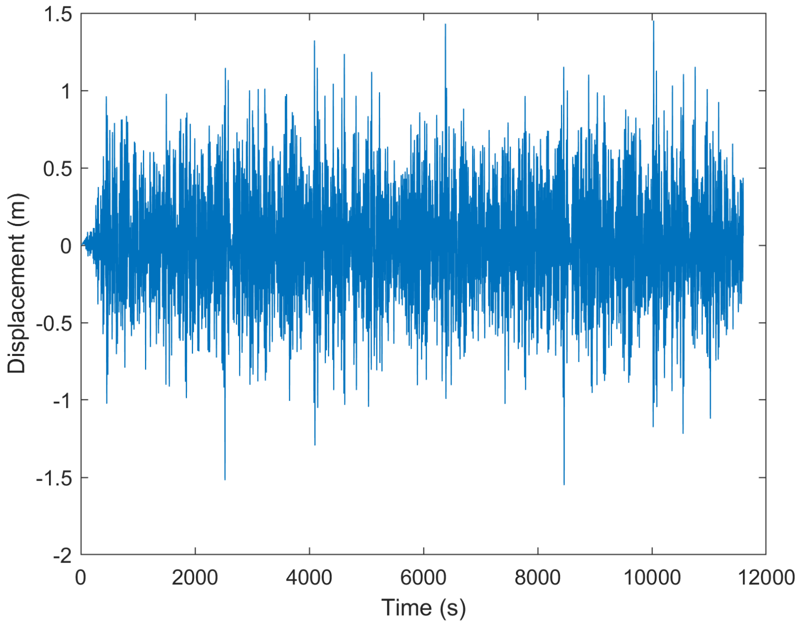

Figure 7.11: Representation of surge time-series for Simulation 0 in sea state 24.

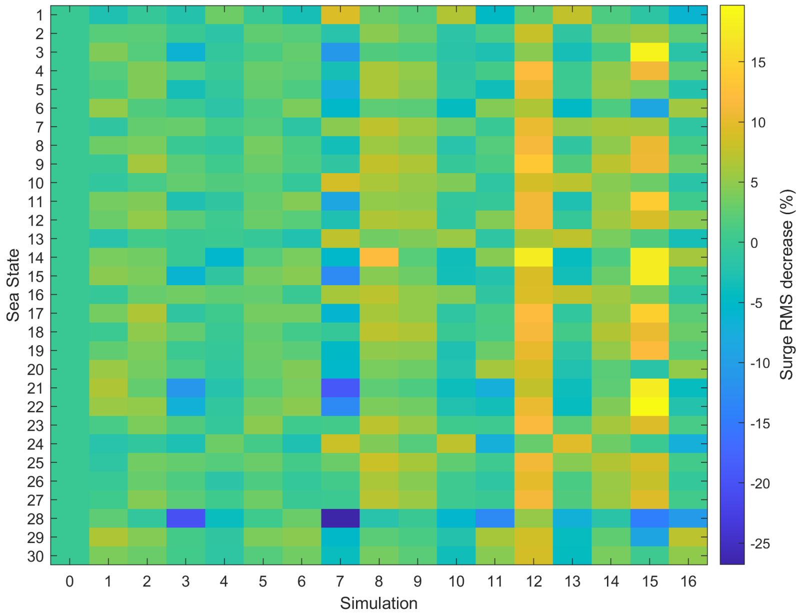

Figure 7.12: Heat Map of the surge RMS for all simulations and sea states.

7.2.3 Heave

Heave motion presents clearly a correlation with T_p (Figure 7.13). The reason behind this is the resonance peak period being 17.54 seconds, and for sea states where peak periods are near this value, the heave amplitudes will tend to increase. The higher values of heave displacement were for sea states 23, 24, 27, 28, and 30, where values ranged between 4 and 6 m. This resonance-driven response highlights the platform's sensitivity to wave excitation near its natural frequency, which can have important implications in tension and fatigue.

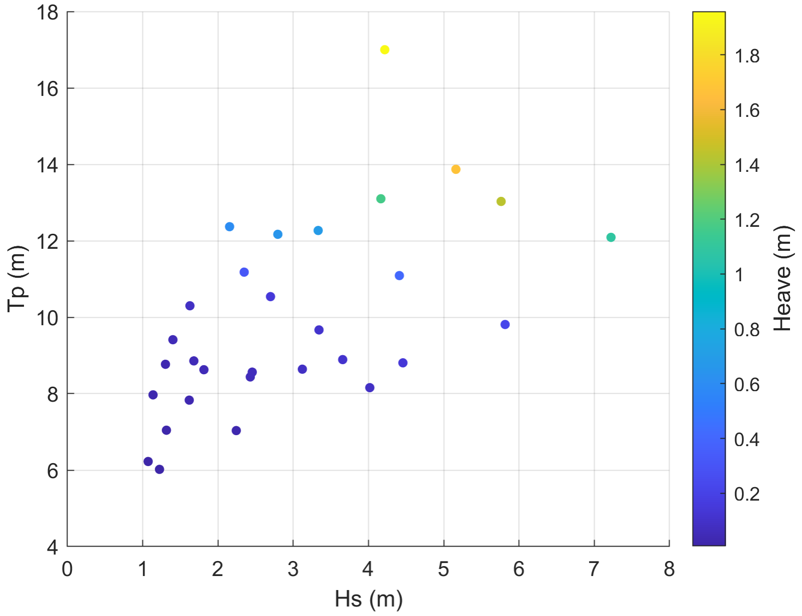

Figure 7.13: Heave representation in Hs/Tp plane.

As shown in Figure 7.14, the heave displacement for sea state 24 exhibits high amplitudes indicative of resonance effects. Additionally, a recurring pattern in the platform's response becomes apparent from approximately 7000 s onward. The underlying cause of this repetitive behaviour remains unclear and warrants further investigation.

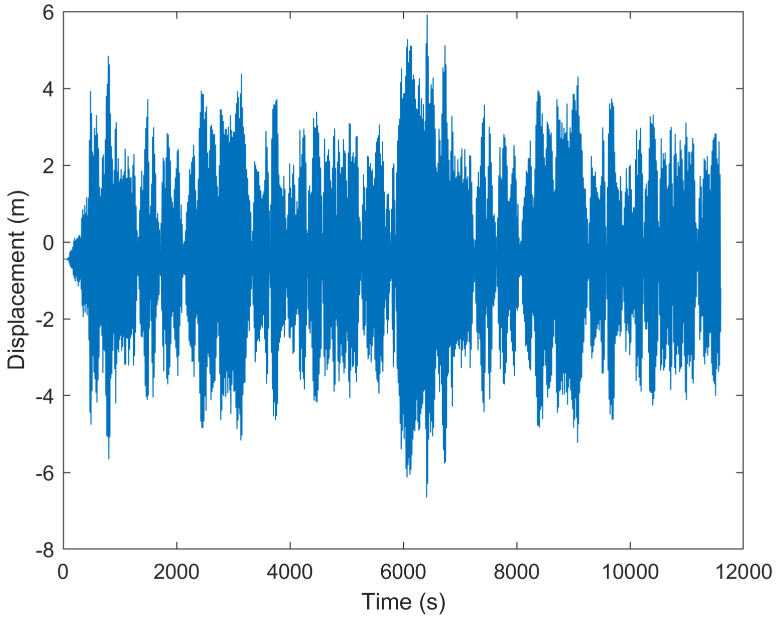

Figure 7.14: Representation of pitch time-series for Simulation 0 in sea state 24.

Compared to the other simulations scenarios, there is a general reduction in heave RMS values, except for Simulations 7, 10, and 13. The most significant decreases were observed in Simulations 12 and 15. The observed increases in heave displacement in certain cases may be attributed to misalignment between the platform configurations and the prevailing wind direction for the specific sea state, as well as diffraction effects occurring between the WECs. Finally, regarding motion, the factors that seem to have a higher impact are the number of WECs and the alignment with the FOWT.

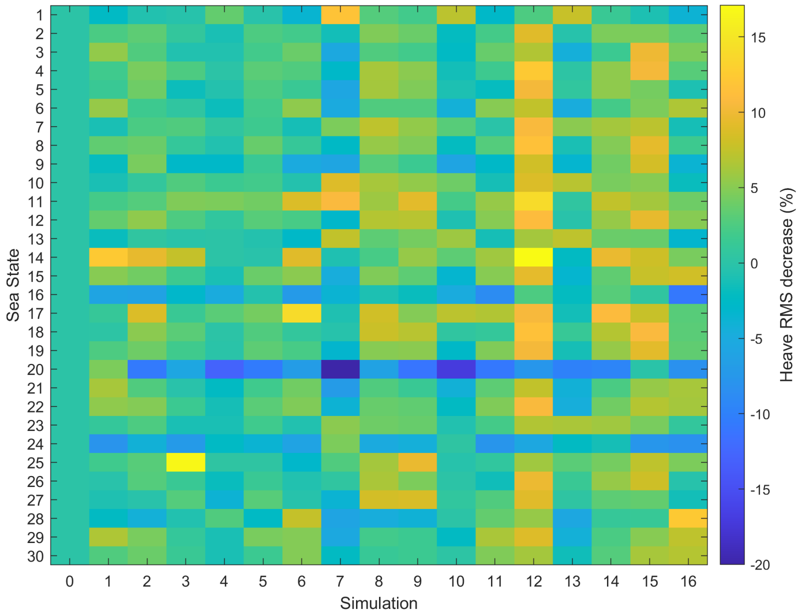

Figure 7.15: Heat Map of the heave RMS for all simulations and sea states.

7.3 Dynamics in Mooring Lines

The results obtained from MooDy regarding the dynamics of the mooring lines include detailed time series of tension at the fairlead for each cable. In addition, MooDy provided information on the operational state of each mooring line at various time steps.

To analyse the fairlead tension, key statistical metrics—minimum, maximum, RMS, and standard deviation—were calculated for each sea state. The highest RMS tension values were observed in sea states 24 and 27; however, RMS variability across sea states was relatively low (Figure 7.18).

Cable 1 consistently exhibited the highest tension values, while cables 2 and 3 showed nearly identical responses. This symmetry is attributed to a limitation in WEC-Sim 2017, which does not support directional wave spectra and assumes a default wave direction of 0º (from the west), resulting in symmetric loading conditions. The comparatively lower tension in Cables 2 and 3 can also be explained by diffraction and shadowing effects caused by the platform structure.

In contrast to the RMS values, the standard deviation of tension showed greater variability, particularly in sea states 23, 24, 27, 28, and 30 for both cables. These sea states also correspond to those with higher heave motion amplitudes. A comparison of the time series data suggests a correlation between heave motion and tension, as illustrated in Figure 7.16.

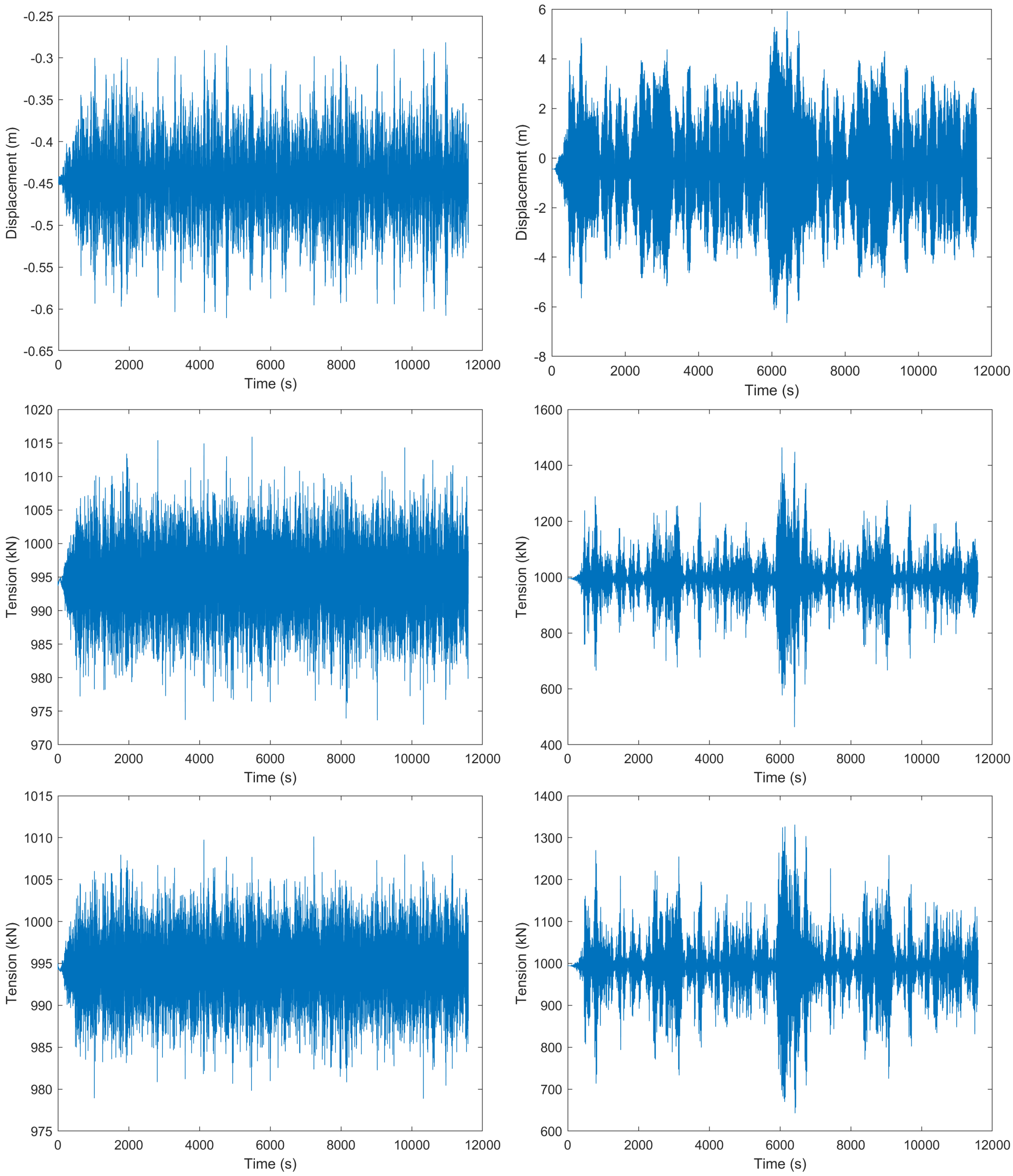

Figure 7.16: Comparison of the heave time-series (first row) with the tension time-series (second row is for Cable 1 and the last for Cables 2 and 3) for sea state 10 (left) and 24 (right).

Although surge motion is typically a dominant contributor to mooring line tension due to its horizontal displacement, this influence is not evident in the current results. This is consistent with the modelling approach, as WEC-Sim does not account for second-order drift forces. Instead, the findings indicate a stronger correlation between heave motion and tension variation. Heave displacements are generally larger than surge across sea states, and this vertical motion appears to be the primary driver of tension fluctuations. However, despite its prominence in the motion response, heave does not always result in the highest tension values due to the mooring system's configuration and the relatively lower sensitivity of axial tension to vertical displacements compared to horizontal ones.

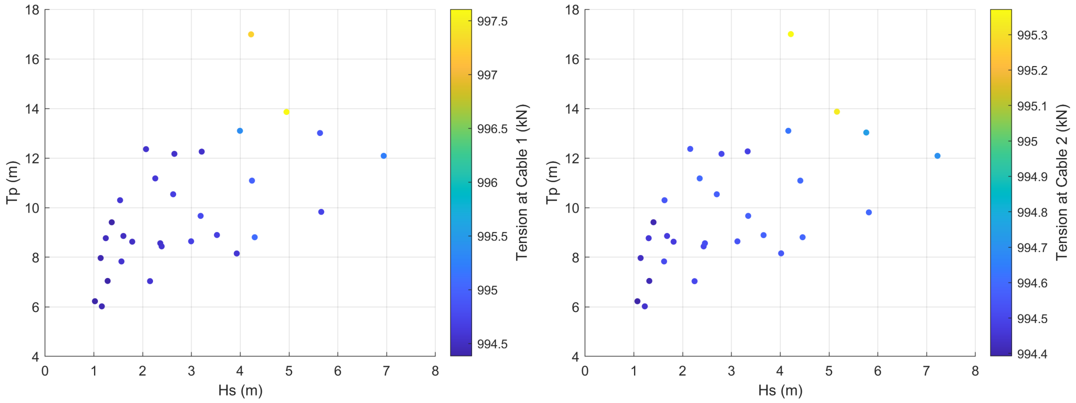

Figure 7.17: Tension representation in Hs/Tp plane in Cables 1 (left) and 2/3(right).

When comparing across simulations, the RMS values showed limited variability; therefore, the standard deviation was used to assess changes in load amplitude. A similar trend to the platform motion was observed: variability decreased most notably in Simulations 12 and 15. This suggests that while the average tension remained consistent, the amplitude of fluctuations was reduced. Contrarily, Simulations 7, 10, and 13 exhibited increased variability, as expected.

Although Cables 1 and 2/3 operate under different tension magnitudes, the relative decrease in variability was similar across all cables. This indicates that the observed trends in load fluctuation are consistent throughout the mooring system, regardless of absolute tension levels.

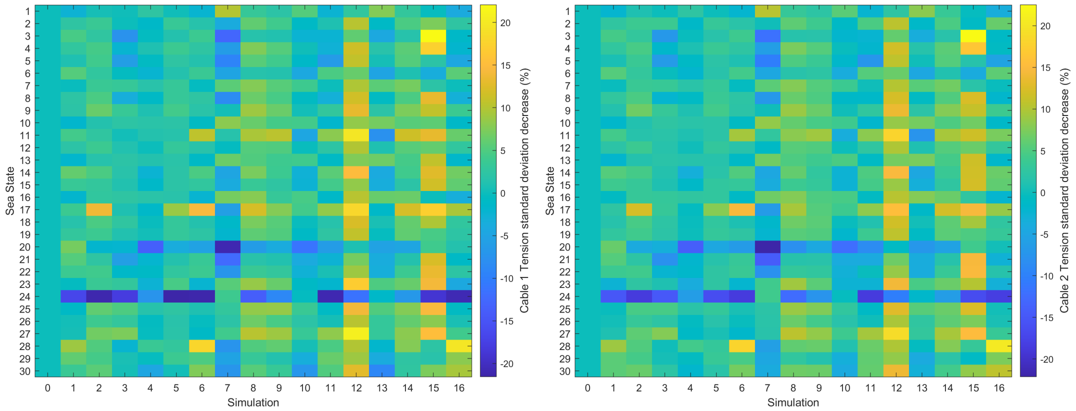

Figure 7.18: Heat Map of the standard deviation of the Tension at Cable 1 and 2/3 for all simulations and sea states.

7.4 Fatigue Analysis

The fatigue analysis starts by analysing the baseline scenario, Simulation 0, for all cables, starting with the unit fatigue in all sea states, then passing to the year fatigue in all sea states, and finally the total fatigue for each cable.

7.4.1 Unit Fatigue Damage across sea states

The unit fatigue is presented in a logarithmic scale (base 10) and can be seen in Figure 7.19. The results for both cables seem to have fluctuations.

Although the sea states are ordered by increasing significant wave height, the same does not apply to the peak period within the significant wave height increase. In several cases, sea states with identical wave heights exhibit different peak periods not sorted. However, there is no clear or consistent relationship between the peak period and fatigue damage. For example, sea states 1 and 2 share the same significant wave height; however, sea state 2 has a shorter peak period and correspondingly lower fatigue damage. In contrast, for sea states 23 and 24, a longer peak period in sea state 24 presents higher fatigue damage.

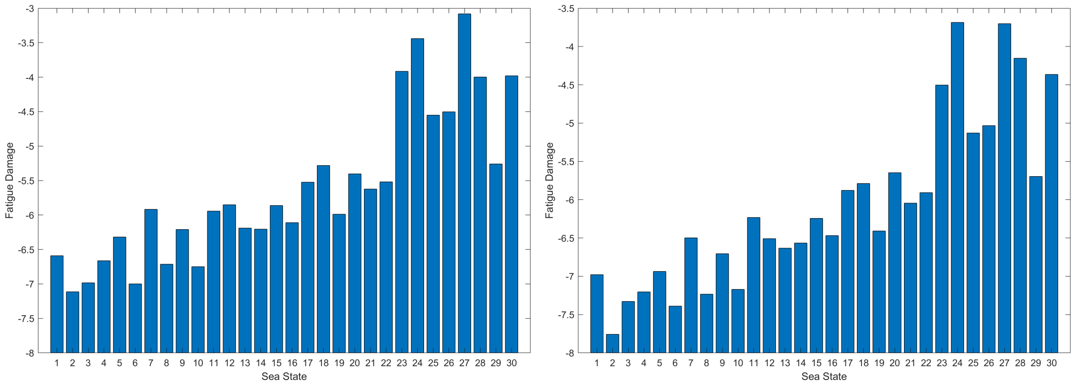

Figure 7.19: Unit fatigue of Simulation 0 for Cable 1 (left), 2, and 3 (right).

Regarding wave direction, for a given significant wave height, fatigue damage tends to be greater when the waves approach from directions near 0° E (i.e., from the west). An exception was noted in the comparison between sea states 24 and 25, where sea state 25, with -8.9º E of wave direction, resulted in lower fatigue damage.

Finally, even considering the fluctuability of the fatigue damage across sea states, it is believed that significant wave height tends to increase fatigue damage. Additionally, sea states 23, 24, 27, 28, and 30 exhibited particularly high damage values.

Among the different mooring cables, Cable 1 consistently exhibited higher fatigue damage, as expected. When considering different sea states in this cable that presented similar fatigue, such as sea state 17, and 22, or 18, and 29 it is essential to understand that the accumulated fatigue in two sea states can be similar if: one sea state has many low amplitude cycles, and the other few high amplitude ones; both sea states have a similar amplitudes cycles.

In sea states 18 and 29, the histogram of the range of stress and number of cycles can be seen in Figure 7.20, and displays a similar distribution. The Table 7.3 presents fatigue in both sea states, as well as the number of cycles to each one. Although the distributions are similar, sea state 18 shows a higher number of cycles and slightly lower fatigue damage than sea state 29. This indicates that sea state 29, despite having fewer cycles, results in greater fatigue damage, likely due to a higher proportion of cycles at more damaging stress ranges.

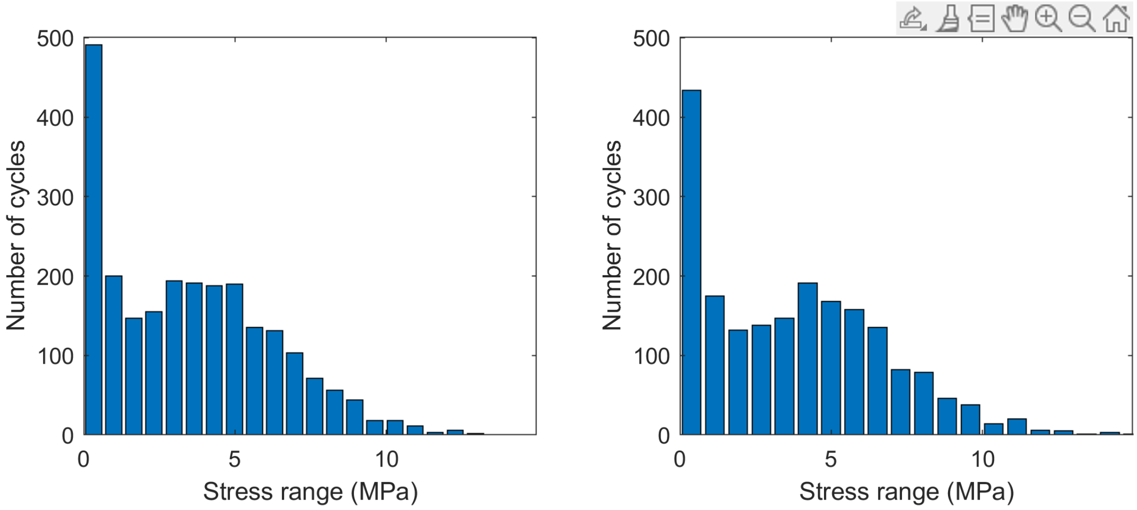

Figure 7.20: Histogram of stress range for sea state 18 (left) and 29 (right) in Cable 1.

Table 7.3: Fatigue damage and number of cycles for sea state 18 and 29.

Sea State	Fatigue Damage	Number of cycles
18	5.23 x 10^{-06}	2354
29	5.50 x 10^{-06}	1973

Interestingly, for sea states 17 and 22, the distributions do not match. Sea state 17 exhibits a high number of cycles at very low stress ranges (0.45 MPa) and an exponential decrease in the number of cycles as stress ranges increase (Figure 7.21). On the other hand, sea state 22, even though it presents fewer cycles, they are presented in the higher stress range, contributing more to fatigue damage. Ultimately, these two states present similar damage, and sea state 22 presents fewer cycles (Table 7.4).

Table 7.4: Fatigue damage and number of cycles for sea state 17 and 22.

Sea State	Fatigue Damage	Number of cycles
17	2.99 x 10^{-06}	2215
22	3.03 x 10^{-06}	2116

These two examples reinforce the key insight that fatigue damage is not solely dependent on the number of cycles, but also on their amplitude. A large number of low-stress cycles can result in similar fatigue damage as a smaller number of high-stress cycles.

Both patterns observed in Cable 1 are also evident in Cables 2 and 3:

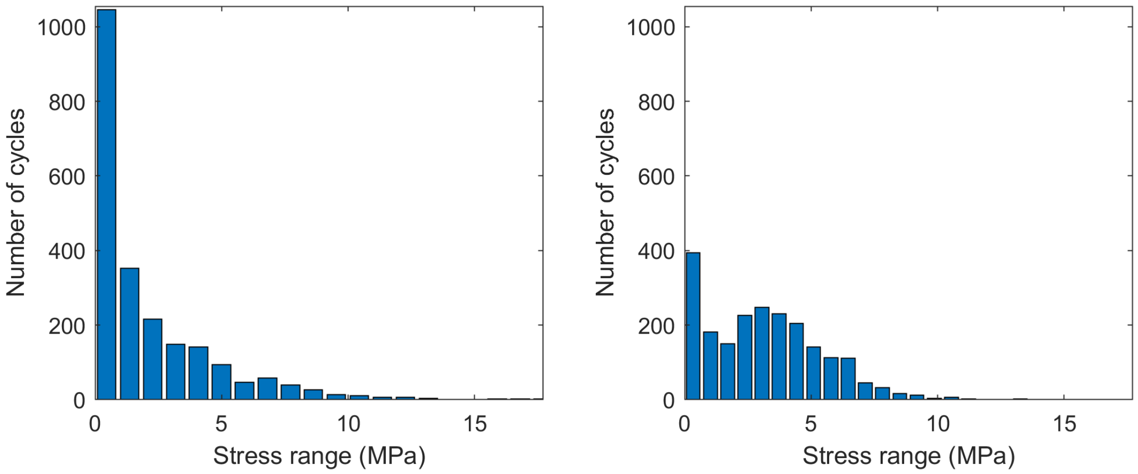

Figure 7.21: Histogram of stress range for sea state 17 (left) and 22 (right) in Cables 2 and 3.

- Sea states 16 and 19 present similar fatigue damage, and the stress range distributions closely match, indicating that both the number and amplitude of cycles are comparable;
- Sea states 17 and 22 demonstrate:
  - A high number of low-stress cycles characterises Sea state 17;
  - Sea state 22 has fewer cycles, but they occur at higher stress ranges, contributing more significantly to fatigue damage.

7.4.2 Year Fatigue Damage across sea states

The annual fatigue damage across sea states depends on the frequency of occurrence of each sea state throughout the year. Sea states with lower occurrence frequencies contribute less to the overall annual fatigue damage (Figure 7.22). In the figures, these values are presented on a logarithmic scale for better visualisation.

To assess the influence of each sea state on the total fatigue damage, the fatigue damage of each sea state is normalised by dividing its annual fatigue value by the total annual fatigue, and then multiplying by 100.

For Cable 1, sea states 1 to 22 and 29 contribute marginally to the total fatigue, each with an influence between 0 % and 1 %. Only the remaining sea states exceed the 1 % threshold. Sea state 26 contributes approximately 2 %, with values ranging from 1.64 % to 2.33 %. Sea states 25, 27, and 30 each contribute between 4 % and 5 %. Notably, sea state 23 contributes around 13 % to the total fatigue. Sea states 24 and 27 exhibit the highest influence, contributing approximately 35 % and 40 % of the total fatigue, respectively, despite sea state 27 having a relatively low occurrence frequency of just 2.4 % (equivalent to 210.24 h).

In Cable 2, sea states 1 to 22, 25, 26, 29, and 30 follow the same trend. However, sea state 23 contributes between 6.4 % and 11.3 %. In this case, sea state 24 has a greater influence on total

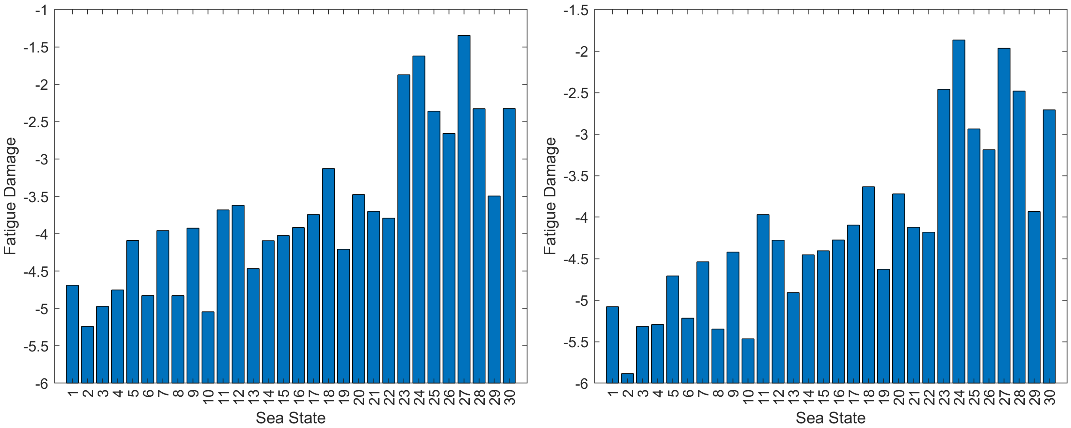

Figure 7.22: Year fatigue of Simulation 0 for Cable 1 (left), 2, and 3 (right).

fatigue than sea state 27, with the latter contributing between 14.2 % and 29.9 %, and sea state 24 contributing between 37.6 % and 61.8 %.

These results affirm that sea states 23, 24 and 27 together account for approximately 82 % of the total fatigue damage in both cables. Therefore, changes in the fatigue contribution from these three sea states — either increases or decreases — will significantly affect the overall fatigue damage.

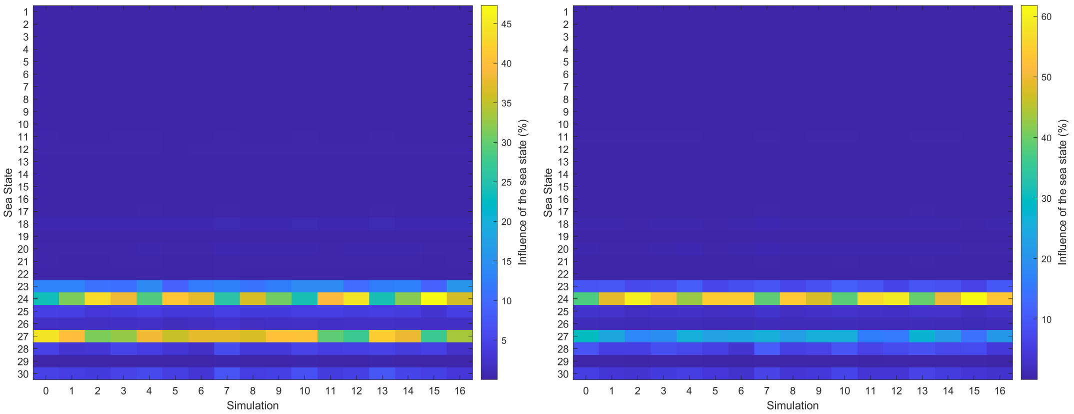

Figure 7.23: Influence of each sea state on the total fatigue in Cable 1 (left), and 2 and 3 (right).

Consistent with the previous analysis, a heat map of the fatigue damage decrease across all sea states and simulations was created (Figure 7.24). Overall, the fatigue damage decreases, except for simulations 3, 4, 7, 10, and 13, and for sea state 24. The increase of fatigue in most simulations for sea state 24 will have a major impact in the total fatigue, and is attributed to the resonance phenomenon. When calculating the RAO in all simulations, a slight shift towards the peak frequency of sea state 24 was perceived, justifying the higher amplitudes of tension and, thereby, the higher fatigue.

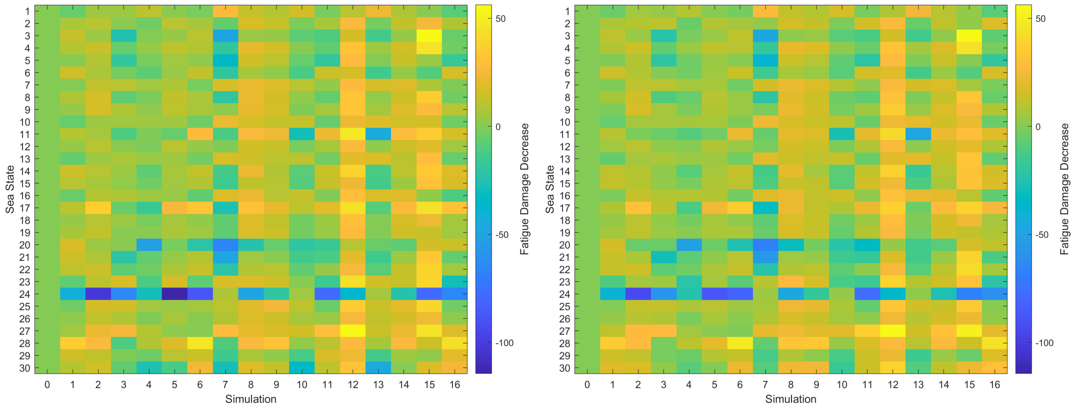

Figure 7.24: Year fatigue of Simulation 0 for Cable 1 (left), 2, and 3 (right).

To illustrate this, simulations 5 and 7 are presented in Figures 7.25 and 7.26, respectively.

In simulation 5, only 4 out of 30 sea states exhibited increased fatigue for both cables. Sea state 24 showed the most significant increase—approximately 115 % in Cable 1 and 90 % in Cable 2. Conversely, sea state 23 experienced a decrease of 17 % and 8 % in Cable 2 and 3. Sea state 27 showed a modest decrease of about 4 % in both cables. Despite the overall decrease in most sea states, the substantial increase in sea state 24 is expected to result in higher total fatigue compared to the baseline simulation.

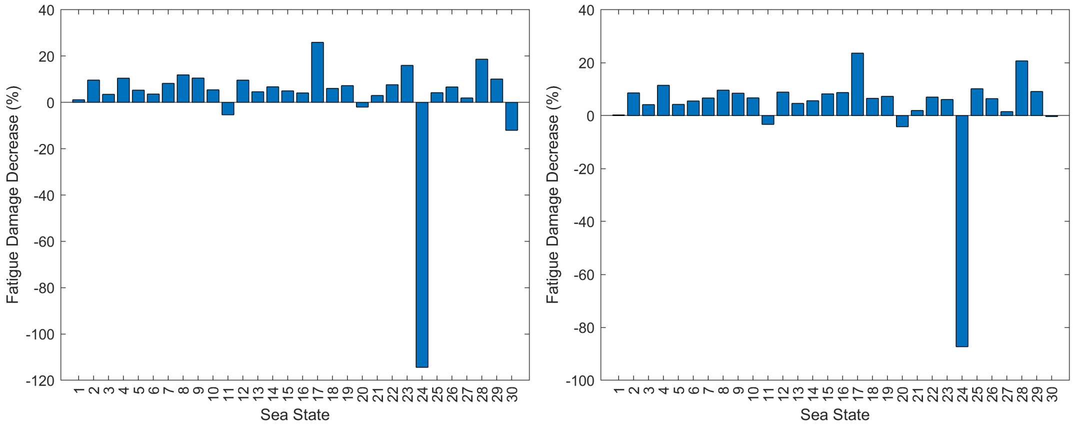

Figure 7.25: Fatigue damage decrease of simulation 5 in Cable 1 (left), and 2 and 3 (right).

Moving to simulation 7, 11 out of 30 sea states showed a positive decrease in fatigue damage. Although sea states 3, 20, and 21 exhibited increases exceeding 45 %, their overall impact on total fatigue is minimal, contributing only 0–1 %. Importantly, sea states 23, 24, and 27 all showed a decrease in fatigue damage, suggesting that this simulation will likely result in lower total fatigue than the baseline. This underscores the dominant influence of these specific sea states.

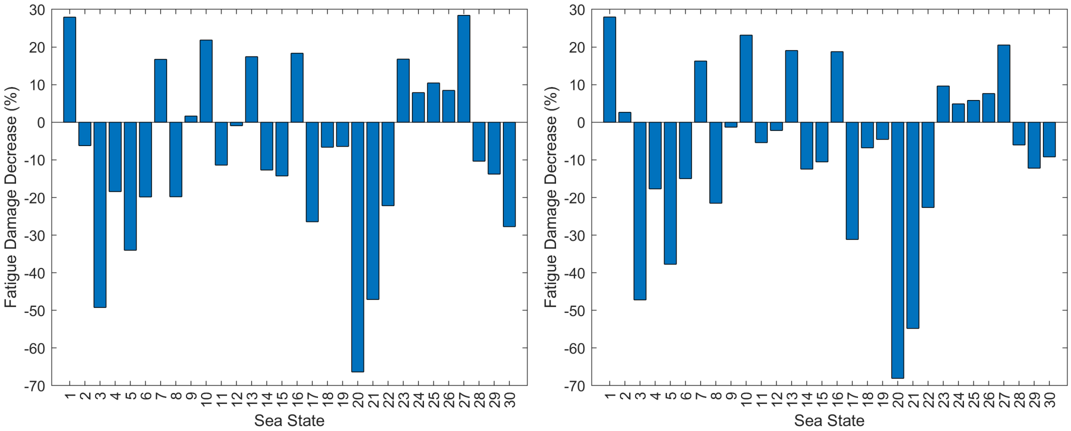

Figure 7.26: Fatigue damage decrease of simulation 5 in Cable 1 (left), and 2 and 3 (right).

To further assess the impact of each sea state on fatigue damage, a matrix was constructed in which the fatigue decrease was weighted by the influence of each sea state. From this matrix, the mean and standard deviation were calculated, alongside the unweighted fatigue damage decrease statistics. These metrics help identify which simulations are likely to exhibit greater reductions in fatigue damage and the variability associated with those reductions (Table 7.5).

The mean is an appropriate measure in this context, as the values fluctuate around zero and have already been adjusted for the frequency of occurrence. Simulations with a negative mean value in the weighted matrix are expected to show an increase in total annual fatigue. However, this inference cannot be made from the unweighted fatigue decrease table, as it does not account for the influence of each sea state and is based on relative decreases rather than absolute values.

Based on this analysis, simulations 7, 9, 10, 12, 13, and 14 are expected to exhibit a reduction in fatigue damage for Cable 1. For Cable 2, simulations 7, 9, 10, and 13 are anticipated to show reductions.

Although the Taguchi method does not directly identify the most influential parameters, further analysis were conducted by grouping the simulations in: Number of WECs (1, 3, 5, 7); Distance between FOWT and WEC array (120, 220, 320, 420 m); Distance between WECs (198, 248, 298, 348 m); Alignment of WEC array with FOWT (180°, 250°, 270°, 350°).

When sorting them the priorities were: Number of WECs, Alignment with the FOWT (as these seem to have a higher impact in fatigue damage), distance FOWT-WEC, and distance WEC-WEC. The analysis focused on Cable 1, as both cables exhibited similar trends. Figures for Cable 2 and 3 are available in Appendix E.

7.4.2.1 Number of WECs

The analysis of the fatigue sorting the number of WECs as stated above, resulted in Figure 7.27. The fatigue for the cases using 1 WEC presented a relatively low variability in terms of fatigue damage decrease (1^{st} heat map in Figure 7.27), and in terms of fatigue decrease, they were the ones that decreased the least. The mean values of fatigue decrease ranged from -3.9 and 8.12 %. The decrease in fatigue damage tends to increase with the addition of WECs, as seen in

Table 7.5: Mean and standard deviation of Fatigue Damage Decrease in the left and weighted with influence of each sea state in the right.

Sim	Cable 1		Cable 2/3	
	Mean	Stand. Dev.	Mean	Stand. Dev.
1	5.01	12.50	5.28	12.39
2	8.12	21.94	7.84	20.65
3	-2.05	16.19	-1.16	15.60
4	-3.94	12.77	-3.84	12.27
5	2.45	23.12	3.58	18.08
6	4.21	21.63	4.21	21.07
7	-7.93	23.37	-7.67	23.18
8	13.64	15.53	13.49	15.91
9	11.41	9.44	11.84	9.16
10	-1.68	12.29	-1.92	11.39
11	0.36	18.91	0.49	20.71
12	26.55	15.95	25.79	15.39
13	-0.56	16.74	0.04	15.22
14	11.94	10.56	12.23	10.77
15	21.33	24.55	20.64	23.37
16	3.44	19.74	4.17	19.19

Sim	Cable 1		Cable 2 / 3	
	Mean	Stand. Dev.	Mean	Stand. Dev.
1	-0.34	2.41	-0.48	3.59
2	-1.12	8.25	-1.59	10.29
3	-0.50	4.83	-0.83	5.79
4	-0.24	1.69	-0.38	1.99
5	-1.48	8.58	-1.51	8.71
6	-1.05	5.98	-1.42	8.12
7	0.40	2.05	0.20	1.06
8	-0.18	3.66	-0.48	4.83
9	0.18	1.75	0.07	1.92
10	0.19	1.24	0.13	0.98
11	-0.78	5.90	-1.26	8.10
12	0.28	4.27	-0.15	4.30
13	0.22	1.31	0.21	0.82
14	0.15	2.12	-0.06	2.79
15	-0.57	7.23	-0.98	7.90
16	-0.67	4.59	-0.91	6.04

simulations 12 and 15, with higher values of fatigue damage decrease. The cases that presented less variability were the simulations using 5 WECs (3rd heat map). In all sets of simulations, there is one simulation with a negative mean fatigue decrease. It always corresponds to the 350º case (4th heat map). Regarding sea states 23, 24, and 27 (Figure 7.28), simulations with a single WEC consistently exhibited negative fatigue damage decreases. Among simulations with three WECs, only simulation 7 showed an overall positive fatigue reduction. Despite some increases in sea state 24, most simulations still demonstrated an overall decrease in fatigue. These findings suggest that increasing the number of WECs significantly enhances fatigue damage reduction.

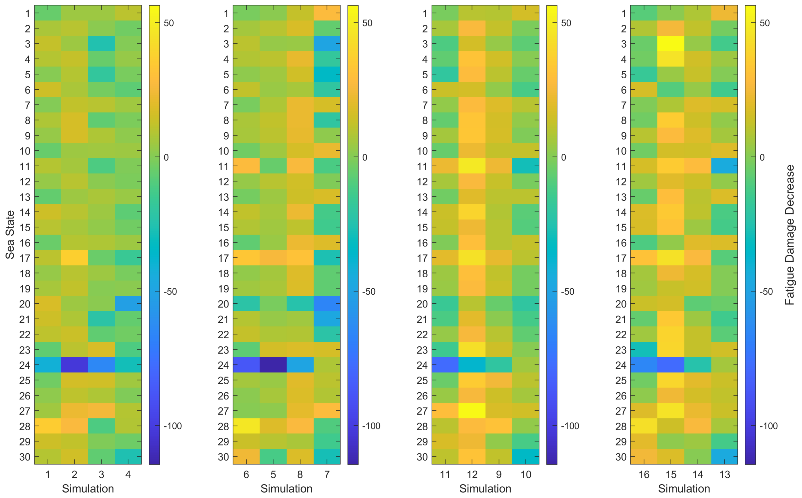

Figure 7.27: Heat maps of year fatigue grouped by number of WECs — 1, 3, 5, 7 from left to right.

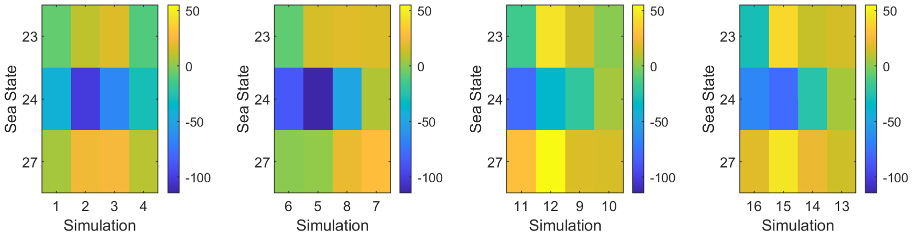

Figure 7.28: Heat maps of year fatigue of Cable 1 of the sea states 23, 24, and 27 grouped by number of WECs — 1, 3, 5, 7 from left to right.

7.4.2.2 Alignment of WEC Array with FOWT

Alignment significantly affects fatigue damage (Figure 7.29). All simulations with a 350° alignment showed negative mean fatigue decreases (fourth heat map). This is explained by the sea state generation process, which is based on a distribution with peaks at 180°, 250°, and 350°, resulting in only six sea states aligned with the 350° direction. Consequently, these simulations exhibited less fatigue reduction, and in some cases, increases, with mean values ranging from -0.56 % to -0.79 %.

Simulations with a 250° alignment (second heat map) achieved the highest fatigue reduction, primarily due to a greater number of aligned sea states, except for sea state 24. This sea state originates from the north, and the 250° alignment offers protection from the southwest. Simulations aligned to the west (third heat map) also showed considerable reductions. In contrast, simulations aligned to the south resulted in lower positive fatigue decreases, even when more WECs were used.

These results confirm that the alignment of the WEC array relative to the FOWT significantly influences fatigue performance. Although WEC-Sim does not explicitly model wave direction, the spectral input from SWAN appears to have propagated the directional effects.

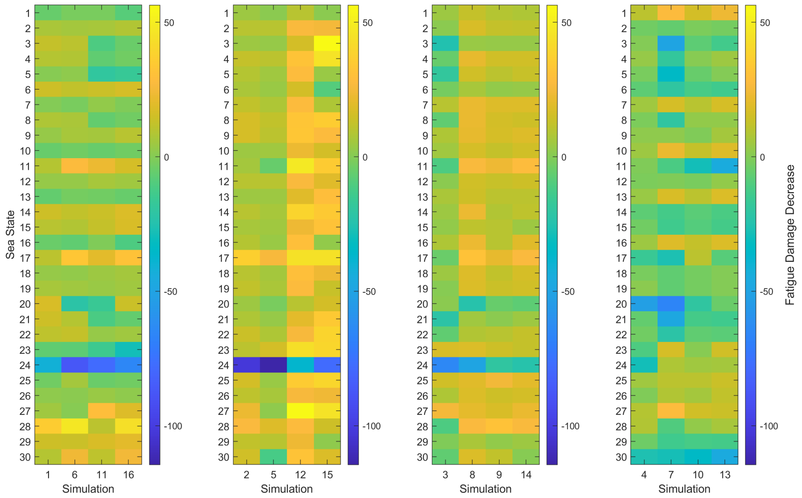

Figure 7.29: Heat maps of year fatigue grouped by alignment of the WEC array with the FOWT — 180º, 250º, 270º, 350º from left to right.

Passing to the analysis of the predominant sea states (Figure 7.30), the effects are aligned with the statements above. The simulation using 180º of alignment presents rather neutral or negative fatigue damage decrease, except for simulations 11 and 16 for sea state 27. Simulations with 250º and 270º show great variability due to wave direction and alignment. The simulations aligned with 350º had a positive damage decrease for all states in simulations 7, 10, and 13.

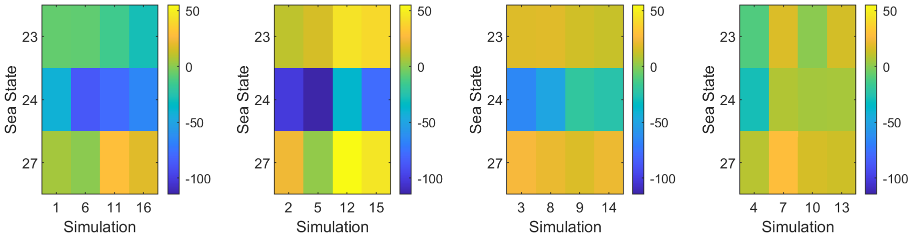

Figure 7.30: Heat maps of year fatigue of cable 1 of the sea states 23, 24, and 27 grouped by alignment of the WEC array with the FOWT — 180º, 250º, 270º, 350º from left to right.

7.4.2.3 Distance between WEC array and FOWT

The impact of the distance between the WEC array and the FOWT on fatigue damage is less definitive (Figure 7.31). Simulations with a 320 m separation (third heat map) demonstrated the most consistent behaviour, with moderate fatigue changes ranging from -2.04 % to 3.44 %. For other distance values, fatigue reductions varied widely—even within the same group—indicating no clear trend in either magnitude or variability.

In sea states 23, 24, and 27, the fatigue damage decreased in simulations using the lower distance, except for simulation 1 (expected as it uses only one WEC). In the remaining cases, the simulations 8, 10, and 13 had the higher fatigue damage decrease, while the others tend to have a fatigue increase, not proving a consistent pattern (Figure 7.32).

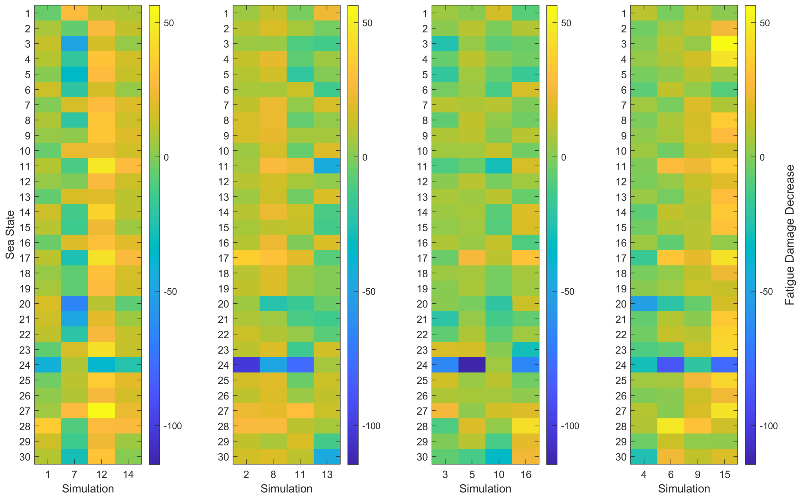

Figure 7.31: Heat maps of year fatigue grouped by distance between WEC array and FOWT — 120 m, 220 m, 320 m, 420 m from left to right.

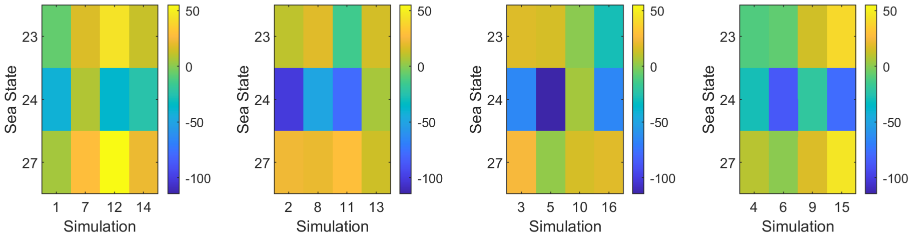

Figure 7.32: Heat maps of year fatigue of cable 1 of the sea states 23, 24, and 27 grouped by distance between WEC array and FOWT — 120 m, 220 m, 320 m, 420 m from left to right.

7.4.2.4 Distance between WECs

Finally, the spacing between WECs also did not exhibit a consistent influence on fatigue reduction (Figure 7.33). For the 198 m spacing group (first heat map), variability in fatigue reduction ranged from 12.28 % to 21.94 %, indicating relatively the lowest variability among all sets. In the other sets, there was no clear behaviour of increased or decreased variability.

For sea states 23, 24, and 27, a progressive trend was observed: simulations with 198 m spacing generally showed a decrease in fatigue damage. As spacing increased to 248 m and 298 m, simulations 7, 9 (from the 240 m set), 12, and 13 (from the 298 m) showed reductions, while the remaining increased. At 348 m, nearly all simulations exhibited increased fatigue, with the exception of simulation 4. This suggests that an increase in the distance between WECs influences fatigue.

Overall, the number of WECs and their alignment with the FOWT appear to have the most significant impact on fatigue damage, while WEC spacing and FOWT-WEC distance have less clear effects. However, this does not imply the latter variables are unimportant. The range of values selected for these parameters may limit the observed effects.

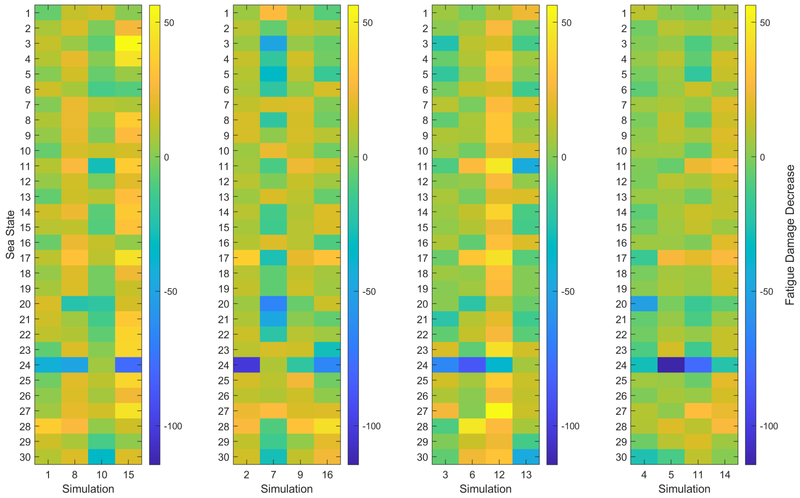

Figure 7.33: Heat maps of year fatigue grouped by distance between WECs — 198 m, 248 m, 298 m, 348 m from left to right.

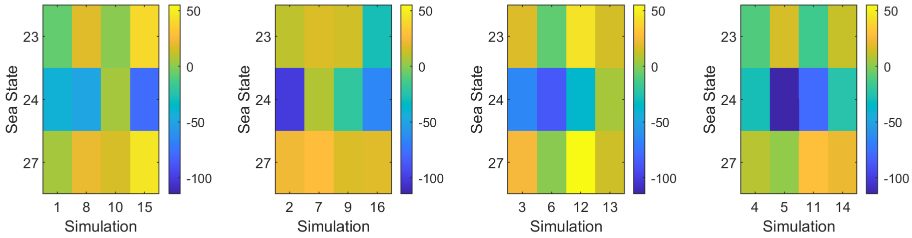

Figure 7.34: Heat maps of year fatigue of cable 1 of the sea states 23, 24, and 27 grouped by distance between WECs — 198 m, 248 m, 298 m, 348 m from left to right.

Additionally, the observed increase in fatigue damage under sea state 24 is expected to influence total annual fatigue negatively. The analysis of the most influential sea states found a slight effect in the distance of FOWT to the WEC array, as well as the distance between WECs. Even though these are only 3 out of 30 sea states, their influence will most likely surpass the effects of the remaining sea states.

7.4.3 Annual Fatigue Damage

The total annual fatigue damage is calculated by summing the contributions from all individual sea states. Table 7.6 presents the total fatigue damage values for each cable over one year, along with the corresponding fatigue life, expressed in years. Fatigue failure is assumed to occur when the accumulated damage equals or exceeds 1. Thus, fatigue life is computed as the inverse of the annual fatigue damage.

Figure 7.35 shows that fatigue damage is reduced in simulations 7, 8, 9, 10, 12, 13, 14, and 15. In contrast, the remaining simulations exhibit an increase in total fatigue. Among all cases, simulation 12 achieves the most significant reduction, with a 27.21 % decrease in Cable 1 and a 13.56 % decrease in Cable 2. This translates to an expected fatigue life of 13.51 years for Cable

Table 7.6: Fatigue damage over one year and fatigue life for Cables 1, 2, and 3.

Simulation	Fatigue Damage		Fatigue Life (years)	
	Cable 1	Cable 2 / 3	Cable 1	Cable 2 / 3
0	0.102	0.036	9.8	27.7
1	0.108	0.039	9.3	25.7
2	0.111	0.044	9.0	22.7
3	0.104	0.041	9.7	24.6
4	0.106	0.040	9.4	25.3
5	0.125	0.047	8.0	21.4
6	0.120	0.045	8.4	22.0
7	0.086	0.033	11.6	29.9
8	0.098	0.037	10.2	27.0
9	0.093	0.034	10.7	29.5
10	0.094	0.034	10.6	29.2
11	0.108	0.042	9.2	23.7
12	0.074	0.031	13.5	32.0
13	0.093	0.034	10.7	29.8
14	0.093	0.034	10.8	29.1
15	0.090	0.037	11.1	27.0
16	0.109	0.041	9.1	24.5

1 and 32.0 years for Cable 2, well above the typical design life of 20 years. In practical terms, the fatigue reduction in Cable 1 implies an increase of 3 years in service life, potentially reducing the maintenance and operation costs. It is important to mention that the fatigue computed in this section is only from tension, not accounting for corrosion or other factors. This means that, despite a substantial decrease in fatigue, not all factors are considered, resulting in an understimation of the real fatigue in the mooring cables.

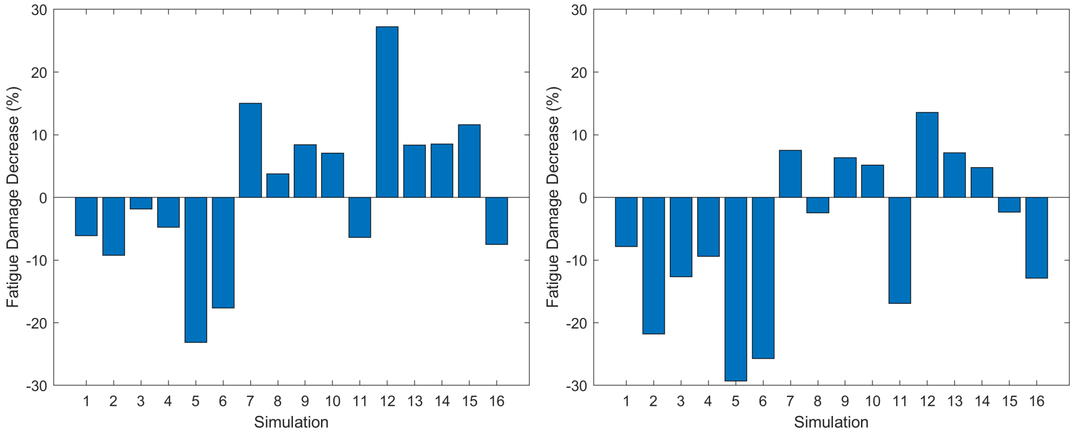

Figure 7.35: Total fatigue damage decrease for all simulations in Cables 1 (left), and 2 and 3 (right).

All simulations in which the total fatigue damage falls below 0.1 (simulations 7, 8, 9, 12, 13, 14, and 15) are considered favourable configurations. Cables 2 and 3 consistently present fatigue levels that allow for a full design life without failure (only accounting for the tension fatigue). However, it is important to note that the expected behaviour in these cables was not fully observed due to a limitation in the numerical model WEC-Sim used in the analysis.

The sea states that resulted in fatigue damage decrease were in line with the analysis made in section 7.4.2. The total fatigue damage follows the trends of the three dominant sea states. Therefore, the year fatigue analysis by group in the previous section will reflect the total fatigue analysis by group.

An analysis of the simulations that reduced fatigue damage in Cable 2 and 3 reveals that only configurations involving more than one WEC exhibited such improvements. Notably, arrays with 5 WECs demonstrated the most consistent reductions (Figure 7.36). Regarding the distance between the WEC array and the FOWT, the 120 m configuration yielded the highest number of favourable outcomes, with 3 out of 4 simulations in that set showing a reduction in fatigue (Figure 7.37). In the spacing between individual WECs, both 248 m and 298 m distances were associated with 3 out of 4 simulations showing fatigue reduction (Figure 7.38). Alignment also played a significant role. No fatigue reduction was observed in simulations with a 180º alignment. In contrast, configurations with alignments of 250º, 270º, and 350º showed reductions in 1, 2, and 3 simulations, respectively (Figure 7.39).

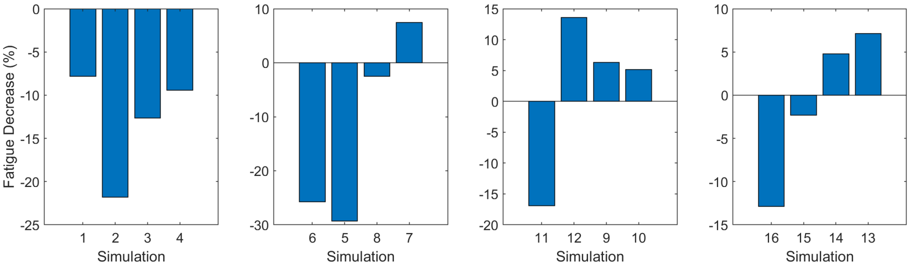

Figure 7.36: Total fatigue decrease in Cable 2 grouped by number of WECs — 1, 3, 5, 7 from left to right.

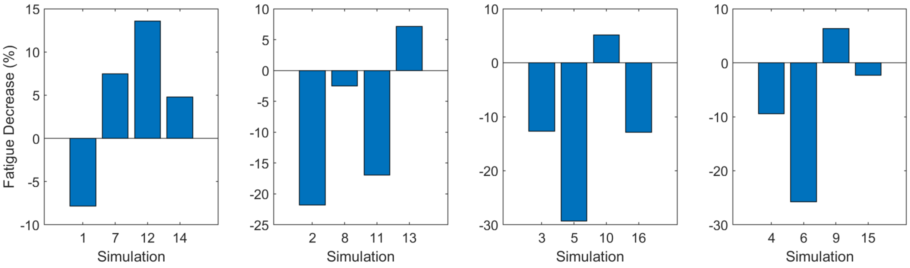

Figure 7.37: Total fatigue decrease in cable 2 grouped by distance between WEC array and FOWT — 120 m, 220 m, 320 m, 420 m from left to right.

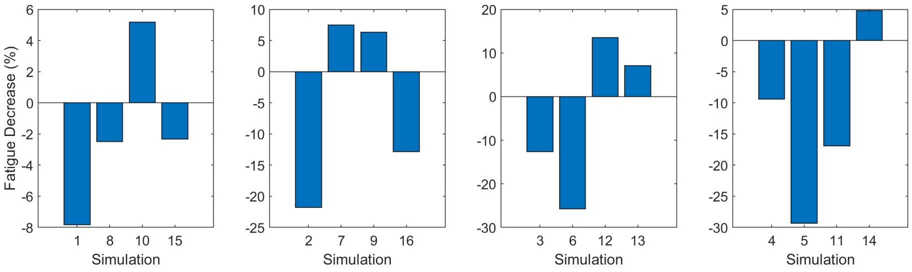

Figure 7.38: Total fatigue decrease in Cable 2 grouped by distance between WECs — 198 m, 248 m, 298 m, 348 m from left to right.

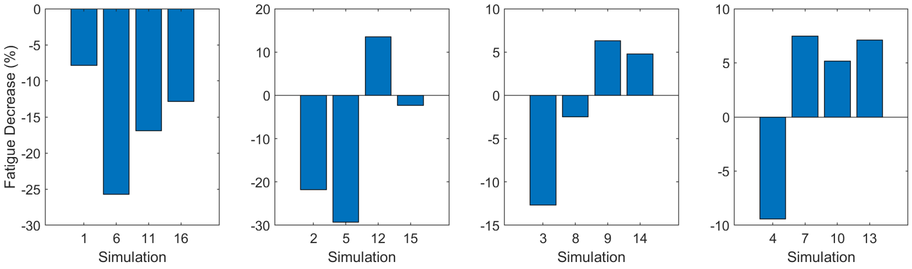

Figure 7.39: Total fatigue decrease in Cable 2 grouped by alignment of the WEC array with the FOWT — 180º, 250º, 270º, 350º from left to right.

In Cable 1, the levels of parameters that showed a higher fatigue decrease were: 5 or 7 WECs, 120 m between the FOWT and WEC array, 198 m between WECs, and 270º or 350º of alignment. The graphics of the total fatigue analysis by group of variables can be found in Appendix E.

These findings suggest that an optimal configuration for minimising fatigue damage in both cables would involve using 5 WECs, positioned 120 m from the FOWT, 248 or 298 m between WECS, and aligned at 350º. The increase in the number of WECs and the lower distance between devices suggest better wave shadowing, leading to a higher fatigue decrease.

Comparing the three configurations with the highest fatigue reduction, simulation 7 utilises 3 WECs, simulation 12 employs 5, and simulation 15 incorporates 7. The feasibility of a project must consider not only the shadow effect but also the energy production of the WECs when co-location is applied. It is expected that the simulations demonstrating greater energy extraction in the wave field analysis correspond to those that absorbed and, consequently, converted more wave energy. Simulations 12 and 15 exhibited higher energy reductions, making them more favourable candidates. Between these two, a comprehensive analysis of cost, energy production, and fatigue reduction in the mooring cables is required. Although the primary focus of this study is the fatigue reduction in the mooring lines of the FOWT, the fatigue experienced by the mooring cables in WECs is also of significant importance, as it contributes substantially to the overall maintenance and operational costs and downtime.

Despite the generally lower fatigue levels in Cables 2 and 3, their relative performance in terms of fatigue reduction is less favourable. These cables show more extreme variations—increases in particular—while experiencing smaller reductions. This sensitivity is likely a consequence of their already low baseline fatigue levels. For example, in simulation 2, Cable 1 exhibited a 10 % increase in fatigue damage (from 0.1016 to 0.1078), whereas Cable 2 experienced a relative increase of over 20 % (from 0.0361 to 0.0390). However, in absolute terms, the increase in Cable 2 was less significant.

The lower fatigue value can likely be attributed to the indirect exposure of Cables 2 and 3 to wave loading, potentially influenced by shadowing effects from the platform structure itself.

The analysis of total annual fatigue damage has highlighted the significant impact of specific sea states on the fatigue life of dynamic cables. While several simulations demonstrated notable reductions in fatigue, others exhibited increases driven primarily by these dominant sea states. Cable 1, being more directly exposed, consistently showed higher fatigue levels. Cables 2 and 3 displayed lower absolute fatigue but were more sensitive to changes due to their reduced baseline levels. It is important to remember that fatigue calculated for Cables 2 and 3 will not be as accurate as wanted for WEC-Sim directional limitation. These findings underscore the importance of both directional wave characteristics and array configuration in influencing fatigue behaviour. The following section discusses a statistical analysis of these results.

7.5 Statistical Analysis

The total fatigue values from simulations 1 to 16 were analysed using Analysis of Variance (ANOVA) and Signal-to-Noise (S/N) ratio analysis, following the Taguchi methodology. The results are presented separately for Cable 1 and Cables 2 and 3.

7.5.1 Cable 1

The ANOVA results for Cable 1 are summarised in Table 7.7. None of the factors were found to be statistically significant at the 95 % confidence level (p-value > 0.05). The lack of statistical significance may be attributed to the high variability inherent in the dataset, the number of samples, and the range of variables studied. The F factor measures the contribution of each factor, a higher value of F means a higher contribution in fatigue reduction.

Table 7.7: ANOVA results for Cable 1.

Variable	Sum Sq.	d.f.	Mean Sq.	F	p-value
Number of WECs	0.00069	3	0.00023	2.90	0.2029
Distance WEC-FOWT	0.00068	3	0.00023	2.83	0.2076
Distance WEC-WEC	0.00031	3	0.00010	1.28	0.4208
Angle	0.00063	3	0.00021	2.62	0.2247
Error	0.0024	3	0.0008	–	–
Total	0.0254	15	–	–	–

A box plot analysis (Figure 7.40) reveals that the parameters involving spatial configuration—specifically distance variables—exhibit higher variability, whereas more uniform responses are observed in number of WECs and alignment, except for an alignment of 250º, and the usage of 3 WECs. These results are consistent with earlier fatigue analysis.

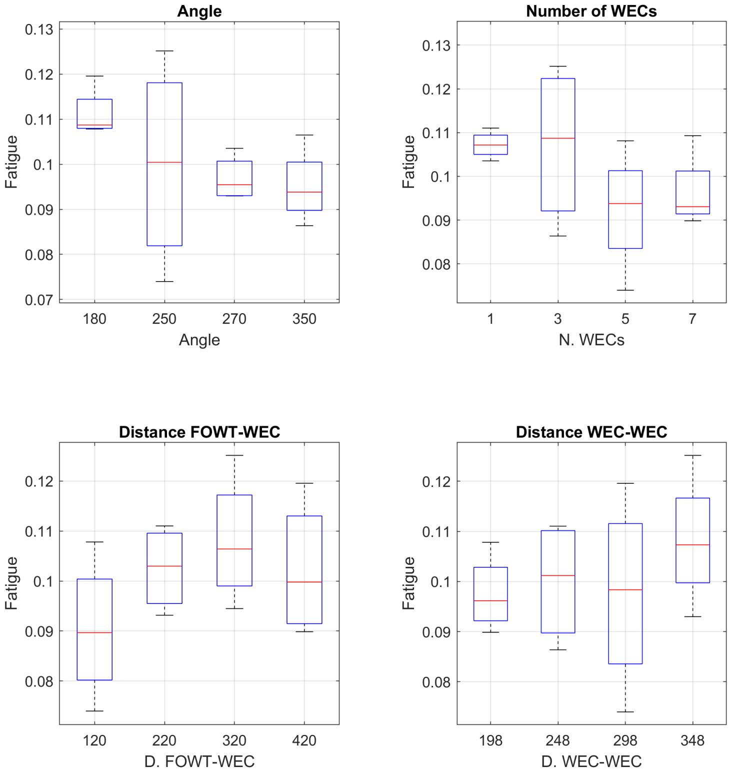

Figure 7.40: Box plot of total fatigue by variable in Cable 1.

Figure 7.41 illustrates the relative contributions of each factor, based on the sum of squares. While not statistically significant, the number of WECs (30.0 %), distance between the WEC array and FOWT (29.4 %), and alignment (27.2 %) were the most influential parameters. The distance between WECs contributed the least (13.3 %). These contributions align partially with the conclusion taken previously, that the number of WECs and alignment are the most influential parameters.

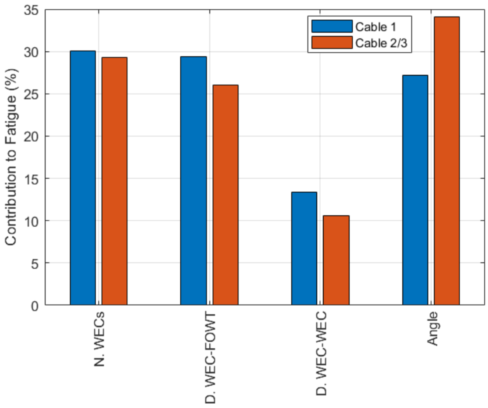

Figure 7.41: Contribution of each variable in total fatigue for Cables 1, 2, and 3.

Additionally, a signal-to-noise (S/N) ratio analysis was conducted following the Taguchi methodology. The S/N ratio, measured in decibels (dB), evaluates the stability and robustness of fatigue performance, where higher values indicate greater consistency across sea states.

Figure 7.42 illustrates the main effects of various parameters on the signal-to-noise (S/N) ratio, providing insights into the robustness and fatigue performance of different configurations.

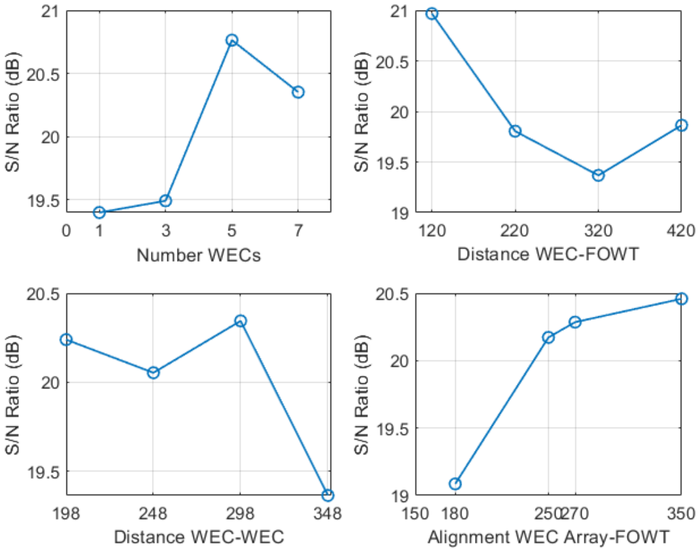

Figure 7.42: Signal-to-Noise analysis grouped by variable in Cable 1.

- Number of WECs: The S/N ratio increases with the number of Wave Energy Converters (WECs), peaking at approximately five units. This trend indicates that a greater number of WECs not only mitigates fatigue damage but also enhances performance consistency across varying sea states.

- Distance between FOWT and WECs: A generally decreasing trend is observed in the S/N ratio as the distance increases from 120 m to 420 m. This indicates that greater separation may introduce more variability in fatigue response, potentially due to reduced hydrodynamic coupling or less effective wave shadowing effect.

- Spacing between WECs: The S/N ratio exhibits a non-monotonic pattern, with noticeable fluctuations between 198 m and 348 m. This behaviour implies a complex relationship influenced by hydrodynamic interactions and wave shadowing, underscoring the importance of careful spacing in array design.

- Alignment Angle: The S/N ratio increases as the alignment angle deviates from 0°, with orientations between 270° and 350° demonstrating the highest robustness, peaking at 350°. Although this last orientation do not align with the predominant wave direction, they appear to reduce direct wave exposure, thereby enhancing fatigue performance stability. Angles such as 250° and 270° also yield high S/N ratios, in this case aligned with the predominant wave direction.

In summary, the S/N analysis confirms that increasing the number of WECs significantly improves fatigue resistance and operational robustness. While other parameters exhibit more nuanced effects, their influence on performance variability should be carefully considered in the design optimisation process, and aligns with the analysis made in the previous section.

7.5.2 Cables 2 and 3

The ANOVA results for Cables 2 and 3 are presented in Table 7.8. Among the tested parameters, the alignment angle was found to be statistically significant at the 95 % confidence level (p = 0.0469). The number of WECs and the distance to the FOWT also showed near-significant effects, with p-values of 0.0573 and 0.0670, respectively.

Table 7.8: ANOVA results for Cables 2 and 3.

Variable	Sum Sq.	d.f.	Mean Sq.	F	p-value
Number of WECs	0.00009	3	3.16e-05	8.37	0.0573
Distance WEC-FOWT	0.00008	3	2.80e-05	7.42	0.0670
Distance WEC-WEC	0.00003	3	1.14e-05	3.01	0.1949
Angle	0.00011	3	3.68e-05	9.73	0.0469
Error	0.00001	4	4.78e-06	–	–
Total	0.00033	15	–	–	–

The relative contributions, shown in Figure 7.41, indicate that alignment angle accounts for 34.1 % of the contribution, followed by number of WECs (29.3 %), FOWT-WEC distance (26.0 %), and spacing between WECs (10.6 %), comparing with Cable 1.

As ilustrated in Figure 7.43, Cable 2 displays corrected main effect trends across all four design variables, with generally higher S/N ratios—ranging from approximately 27.5 dB to 29.2 dB—indicating greater robustness compared to Cable 1.

- Number of WECs: The S/N ratio increases steeply from 1 to 5 WECs, peaking at 5 and slightly decreasing at 7, with an overall increase with the number of WECs, suggesting not only reducing fatigue damage but also enhancing the consistency of the response;
- Distance between WEC Array and FOWT: Performance degrades at intermediate distances, especially around 320 m, with some recovery at 420 m. This indicates that intermediate distances may lead to greater variability in fatigue response, potentially due to suboptimal wave shadow effect or interference effects;
- Distance between WECs: The plot indicates an optimal spacing around 198 m, aligning with trends observed in Cable 1. Spacings of 348 m are detrimental for robustness;

- Alignment Angle: The trend is similar to Cable 1 in terms of the rise of S/N ratio with alignment, however, the increase is less subtle from 180 to 250º, and grows exponentially for 270º;

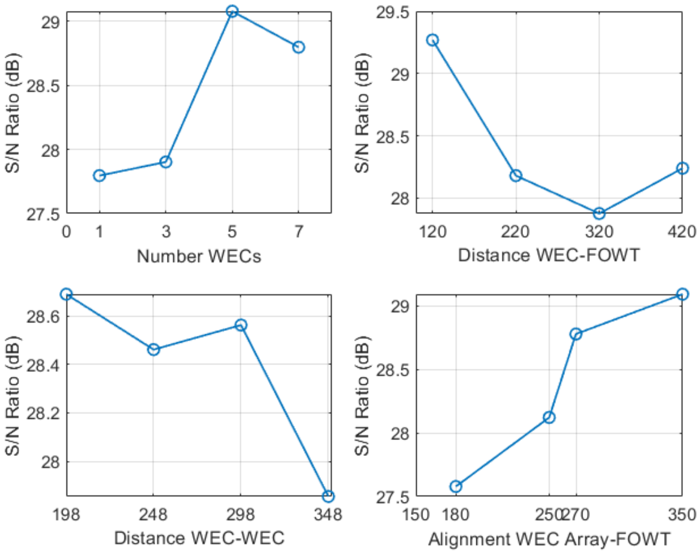

Figure 7.43: Signal-to-Noise analysis grouped by variable in Cables 2 and 3.

The statistical analysis of fatigue damage for Cable 1 reveals that the number of WECs, distance to the FOWT, and alignment angle are the most influential parameters. While the ANOVA results for Cable 1 did not show statistical significance, the sum of squares analysis indicates meaningful contributions from these factors. For Cable 2, the alignment angle was found to be statistically significant, emphasising the importance of directional wave effects.

The Signal-to-Noise ratio analysis further supports these findings, demonstrating that configurations with more WECs and optimised spatial arrangements yield more stable and desirable fatigue performance. In both Cables, the configurations that showed greatest robustness were 5 WECs, 120 m between WEC array and FOWT, 198 m between WECs, and 350º of alignment. These insights are critical for optimising mooring system design, enhancing reliability, and extending the lifespan of offshore structures.

Chapter 8

Conclusion and Further Work

This thesis investigated the structural implications of co-locating Wave Energy Converters with Floating Offshore Wind Turbines, focusing on the fatigue behaviour of mooring cables. Through a combination of statistical sea state modelling, numerical simulations, and fatigue analysis, the study assessed how WEC configurations influence fatigue performance under realistic ocean conditions.

Wave field simulations demonstrated that WECs can significantly attenuate wave energy, particularly when arranged in higher numbers and aligned around 250° for the range of sea states studied. Maximum reductions in significant wave height reached up to 23 %, confirming that co-location can effectively reduce wave-induced loads. However, attenuation varied across sea states, highlighting the importance of environmental directionality and array orientation. The changes in peak period did not correlate with the simulations, and direction did not follow a pattern.

The dynamic response of the FOWT platform revealed a correlation of both surge and pitch with significant height. In the heave motion, it was not clear that this relation was due to the resonance effect, which was clear for several sea states, enhancing the amplitudes of these, prevailing a relationship between peak period and heave motion.

Mooring analysis showed that heave-induced motion was the dominant factor affecting tension variability because second-order drift forces were not accounted for. Cable 1, most exposed to incoming waves, consistently experienced the highest loads, and Cables 2 and 3 presented identical loads of lower amplitude. Additionally, simulations 12 and 15 demonstrated reduced standard deviation in line tension, resulting in smoother load profiles.

Fatigue analysis confirmed that co-location can substantially reduce mooring fatigue, with simulation 12 achieving a 27 % reduction in Cable 1 and meaningful improvements in Cables 2 and 3. Sea states 23, 24, and 27 were identified as the most influential sea states contributing to up to 82 % of the annual fatigue. Alignment and WEC quantity emerged as the most impactful factors, while spacing and distance showed more nuanced, case-dependent effects.

Statistical analysis validated these findings. Although ANOVA did not show significance for Cable 1, alignment proved to be statistically important for Cables 2 and 3. Signal-to-noise ratio analysis supported the robustness of configurations with more WECs, lower spacing between devices, and better alignment. These results illustrate the value of structured experimental design, such as the Taguchi method, in identifying optimal co-location layouts.

Several limitations were noted. The unidirectional wave input in WEC-Sim underestimated directional fatigue differences, particularly in Cables 2 and 3. The model also did not include second-order drift forces.

Despite these limitations, the findings demonstrate the feasibility and potential of co-location as a structural design strategy for offshore renewable systems. Careful array configuration can improve fatigue performance, reduce maintenance, and support more resilient and cost-effective marine energy deployment.

8.1 Future Work

Based on the outcomes of this study, the following research directions are recommended to develop further and refine co-location systems:

- Simulation of the optimal scenario: Take the optimal values in terms of robustness and minimal fatigue, and calculate the fatigue to assess if it would be in fact the optimal scenario;
- Incorporation of Directional Spectra: Implementing directional wave spectra in WEC-Sim would enhance the accuracy of mooring line fatigue predictions, especially for cables not aligned with the primary wave direction;
- Expanded Parameter Space and Simulation Scope: Increasing the range of studied variables—such as a broader number of WECs—and expanding the number of simulations would allow for a more detailed investigation of configuration effects across a more expansive design space;
- Fatigue Analysis of WEC Mooring Systems: Including the WEC moorings in the fatigue analysis would provide a more comprehensive understanding of structural interactions and lifecycle performance in co-located systems.
- Experimental Validation: Conducting physical model testing or analysing field data would help validate numerical predictions and improve model calibration.

Bibliography

Amarouche, K., Akpınar, A., Rybalko, A., and Myslenkov, S. (2023). Assessment of SWAN and WAVEWATCH-III models regarding the directional wave spectra estimates based on Eastern Black Sea measurements. *Ocean Engineering*, 272:113944.

Astariz, S., Perez-Collazo, C., Abanades, J., and Iglesias, G. (2015). Towards the optimal design of a co-located wind-wave farm. *Energy*, 84:15–24.

Barajas, G., Lara, J. L., Davidson, J., and Romano, A. (2025). Porous medium-based PTO damping and overset mesh motion: A combined approach for effective OpenFOAM® simulations of floating OWCs. *Applied Ocean Research*, 154:104309.

Barrera, C., Battistella, T., Guanche, R., and Losada, I. J. (2020). Mooring system fatigue analysis of a floating offshore wind turbine. *Ocean Engineering*, 195:106670.

Bjørni, F., Lien, S., Midtgarden, T., Santos, L., and Jiang, Z. (2023). Life cycle cost analysis of a floating wind farm in the Norwegian Sea. *IOP Conference Series: Materials Science and Engineering*, 1294:012006.

Brodtkorb, P. A., Johannesson, P., Lindgren, G., Rychlik, I., Rydén, J., and Sjö, E. (2000). WAFO — a Matlab toolbox for the analysis of random waves and loads. In *Proc. 10th Int. Offshore and Polar Eng. Conf., ISOPE, Seattle, USA*, volume 3, pages 343–350.

Cagatay, G. (2024). Global offshore wind capacity rises 24% in 2023, second-highest growth in offshore wind history. https://www.aa.com.tr/en/energy/electricity/global-offshore-wind-capacity-rises-24-in-2023-second-highest-growth-in-offshore-wind-history/42117. Accessed: 2025-06-02.

Carballo, R. and Iglesias, G. (2013). Wave farm impact based on realistic wave-WEC interaction. *Energy*, 51:216–229.

Clark, C. E. and Paredes, G. M. (2018). Effects of co-located floating wind-wave systems on fatigue damage of floating offshore wind turbine mooring cables. In *ASME 2018 1st International Offshore Wind Technical Conference*, page 10. ASME International.

Costanzo, G., Brindley, G., and Tardieu, P. (2025). Wind energy in Europe: 2024 Statistics and the outlook for 2025–2030. WindEurope, Brussels, Belgium.

Cruz, J. and Atcheson, M., editors (2016). *Floating Offshore Wind Energy: The Next Generation of Wind Energy*. Green Energy and Technology. Springer International Publishing.

Deumic, A. and Halmkrona, J. (2019). Gaussian Copula. Academic assignment report for Financial Risk—MVE220, Chalmers University of Technology.

Dhanak, M. R. and Xiros, N. I., editors (2016). *Springer Handbook of Ocean Engineering*. Springer Handbooks. Springer Nature.

DNVGL-OS-E301 (2018). Offshore Standards for Position Mooring. Technical Report DNVGL-OS-E301, Det Norske Veritas.

Dodet, G., Bertin, X., and Taborda, R. (2010). Wave climate variability in the North-East Atlantic Ocean over the last six decades. *Ocean Modelling*, 31:120–131.

EMODnet Bathymetry Consortium (2024). Emodnet digital terrain model (dtm) – 2024 release. `https://emodnet.ec.europa.eu/en/bathymetry`.

Fernandez, H., Iglesias, G., Carballo, R., Castro, A., Fraguela, J. A., Taveira-Pinto, F., and Sanchez, M. (2012). The new wave energy converter WaveCat: Concept and laboratory tests. *Marine Structures*, 29:58–70.

Fuchs, R., Zuckerman, G. R., Duffy, P., Shields, M., Musial, W., Beiter, P., Cooperman, A., and Bredenkamp, S. (2024). The Cost of Offshore Wind Energy in the United States from 2025 to 2050. Technical Report NREL/TP-5000-88988, National Renewable Energy Laboratory.

Gomes, J. M. V. B. (2018). Mechanical Design of a Wave Energy Converter: Spider Power UP—Powertrain System, CAD, FEM Stress Analysis. MSc thesis, Faculdade de Engenharia, Universidade do Porto, Porto, Portugal.

Hersbach, H., Bell, B., Berrisford, P., Biavati, G., Horányi, A., Muñoz Sabater, J., Nicolas, J., Peubey, C., Radu, R., Rozum, I., Schepers, D., Simmons, A., Soci, C., Dee, D., and Thépaut, J.-N. (2023). ERA5: Hourly data on single levels from 1940 to present. Copernicus Climate Change Service (C3S) Climate Data Store (CDS). Accessed: 2025-03-25.

Iglesias, G. and Carballo, R. (2014). Wave farm impact: The role of farm-to-coast distance. *Renewable Energy*, 69:375–385.

Ingram, D., Smith, G., Bittencourt-Ferreira, C., and Smith, H., editors (2011). *Protocols for the Equitable Assessment of Marine Energy Converters*. The Institute for Energy Systems, School of Engineering, The University of Edinburgh.

Jani, J. M., Leary, M., and Subic, A. (2016). Fatigue of NiTi SMA-pulley system using Taguchi and ANOVA. *Smart Materials and Structures*, 25:057001.

Kesari, J. P., Gupta, A., Shukla, K., and Garg, P. (2019). A review of the combined wind and wave energy technologies. *International Journal of Engineering Trends and Technology*, 67:131–136.

Koo, B. J., Goupee, A. J., Kimball, R. W., and Lambrakos, K. F. (2014). Model tests for a floating wind turbine on three different floaters. *Journal of Offshore Mechanics and Arctic Engineering*, 136:020907.

Ladeira, I., Márquez, L., Echeverry, S., Le Sourne, H., and Rigo, P. (2022). Review of methods to assess the structural response of offshore wind turbines subjected to ship impacts. *Ships and Offshore Structures*, 18:755–774.

Lamei, A. and Hayatdavoodi, M. (2020). On motion analysis and elastic response of floating offshore wind turbines. *Journal of Ocean Engineering and Marine Energy*, 6:71–90.

Li, L., Gao, Z., and Moan, T. (2013). Joint environmental data at five European offshore sites for design of combined wind and wave energy devices. In *ASME 2013 32nd International Conference on Ocean, Offshore and Arctic Engineering*, volume 8, page 12.

MathWorks (2025). Kernel distribution. MATLAB R2025a Documentation [Online].

Monteiro, N. M. (2017). Efeito da Extração da Energia das Ondas na Propagação da Agitação Marítima na Costa Portuguesa. MSc thesis, Faculdade de Engenharia, Universidade do Porto, Porto, Portugal.

Palm, J. (2014). Developing Computational Methods for Moored Floating Wave Energy Devices. Licentiate thesis, Chalmers University of Technology, Göteborg, Sweden.

Palm, J. and Eskilsson, C. (2023). *MoodyCore Manual version 3.0*. MoodyMarine, Goteborg, Sweden.

Paredes, G. M. (2016). *Study of Mooring Systems for Offshore Wave Energy Converters*. PhD thesis, Faculdade de Engenharia, Universidade do Porto, Porto, Portugal.

Pecher, A. and Kofoed, J. P., editors (2016). *Handbook of Ocean Wave Engineering*. Ocean Enginering and Oceanography. Springer Nature.

Perez-Collazo, C., Astariz, S., Abanades, J., Greaves, D., and Iglesias, G. (2014). Co-located wave and offshore wind farms: A preliminary case study of an hybrid array. *Coastal Engineering Proceedings*, page 10.

Ramos, V., Giannini, G., Calheiros-Cabral, T., López, M., Rosa-Santos, P., and Taveira-Pinto, F. (2022). Assessing the effectiveness of a novel WEC concept as a co-located solution for offshore wind farms. *Journal of Marine Science and Engineering*, 10:267.

Robertson, A., Jonkman, J., Masciola, M., Goupee, A., Coulling, A., and Luan, C. (2014). Definition of the Semisubmersible Floating System for Phase II of OC4. Technical Report NREL/TP-5000-60601, National Renewable Energy Laboratory.

Robertson, A., Jonkman, J., and Wendt, F. (2017). Definition of the OC5 DeepCwind Semisubmersible Floating System. Technical report, National Renewable Energy Laboratory.

Rolo Pérez, L. (2014). Design, Testing and Validation of a Scale Model Semisubmersible Offshore Wind Turbine under Regular Irregular Waves and Wind Loads. MSc thesis, University of Strathclyde, Glasgow, UK.

Ruehl, K., Keester, A., Forbush, D., Grasberger, J., Husain, S., Leon, J., Ogden, D., and Shabara, M. A. (2024). WEC-Sim: Wave Energy Converter SIMulator v6.1.2. Zenodo, National Renewable Energy Laboratory and Sandia National Laboratories.

Sricharan, V. V. S. and Chandrasekaran, S. (2021). Time-domain analysis of a bean-shaped multibody floating wave energy converter with a hydraulic power take-off using WEC-Sim. *Energy*, 223:119985.

Teixeira-Duarte, F., Rosa-Santos, P., and Taveira-Pinto, F. (2025). Multi-objective optimization of co-located wave-wind farm layouts supported by genetic algorithms and numerical models. *Renewable Energy*, 241:122362.

The SWAN Team (2024). SWAN User Manual, SWAN Cycle III version 41.51. Delft University of Technology, Delft, The Netherlands.

Wang, T., Zhu, K., Cao, F., Li, D., Gong, H., Li, Y., and Shi, H. (2024). A coupling framework between OpenFAST and WEC-Sim. Part I: Validation and dynamic response analysis of IEA-15-MW-UMaine FOWT. *Renewable Energy*, 225:120249.

Wilks, D. S. (2006). *Statistical Methods in the Atmospheric Sciences*. Academic Press, 2nd edition.

Williams, R. and Zhao, F. (2024). Global offshore wind report 2024. Global Wind Energy Council, Brussels, Belgium.

Yang, S.-H., Ringsberg, J. W., Johnson, E., Hu, Z., and Palm, J. (2016). A comparison of coupled and de-coupled simulation procedures for the fatigue analysis of wave energy converter mooring lines. *Ocean Engineering*, 117:332–345.

Zhang, Y., Zhao, Y., Sun, W., and Li, J. (2021). Ocean wave energy converters: Technical principle, device realization, and performance evaluation. *Renewable and Sustainable Energy Reviews*, 141:110764.

Zou, S., Robertson, B., Roach, A., Mundon, T., Rosenberg, B., and Penalba, M. (2024). Wave energy converter arrays: A methodology to assess performance considering the disturbed wave field. *Renewable Energy*, 229:120719.

Appendix A

Sea States Generated

Table A.1: Frequency of each sea state.

Sea State	Probability	Sea State	Probability
1	0.027	16	0.053
2	0.026	17	0.021
3	0.035	18	0.049
4	0.028	19	0.021
5	0.058	20	0.029
6	0.051	21	0.029
7	0.031	22	0.018
8	0.026	23	0.038
9	0.066	24	0.024
10	0.017	25	0.053
11	0.063	26	0.024
12	0.058	27	0.019
13	0.018	28	0.016
14	0.044	29	0.020
15	0.024	30	0.016

Table A.2: Sea states generated.

Sea State	H_s [m]	T_p [s]	θ [° N]	T_{m10} [s]	U_{wind} [m/s]	θ_{wind} [°]	σ_θ [°]	$\gamma[-]$
1	1.1	8.0	332.0	6.0	5.4	188.8	27.6	1.0
2	1.1	6.3	239.3	6.5	1.2	239.8	34.2	1.0
3	1.3	7.1	187.0	6.3	6.5	265.4	37.1	1.0
4	1.3	8.8	248.2	7.4	0.9	340.8	52.2	1.0
5	1.3	6.0	247.8	6.4	2.3	223.0	32.7	1.0
6	1.4	9.5	196.1	8.0	0.4	233.9	31.1	1.0
7	1.6	7.9	287.7	7.3	5.7	211.8	30.7	1.0
8	1.6	8.9	241.3	5.9	7.2	257.8	37.2	1.0
9	1.6	10.4	258.1	6.8	4.9	206.1	29.5	1.0
10	1.8	8.7	305.4	8.3	5.6	202.6	30.7	1.0
11	2.1	12.5	222.6	9.6	6.7	360.0	61.7	1.0
12	2.3	7.1	236.7	6.8	9.3	313.2	47.0	1.4
13	2.3	8.5	312.4	6.8	10.6	282.6	39.3	1.0
14	2.3	11.3	209.3	10.0	6.6	242.0	33.5	1.0
15	2.5	8.6	209.5	8.0	8.0	234.0	32.2	1.0
16	2.6	10.6	297.7	8.4	9.1	281.5	40.0	1.0
17	2.7	12.3	230.4	9.2	8.3	225.3	31.0	1.0
18	3.1	9.7	260.0	8.0	12.3	228.3	31.7	1.0
19	3.2	8.7	229.9	7.4	9.8	318.7	46.1	1.2
20	3.3	12.4	206.3	9.1	7.3	250.0	34.3	1.0
21	3.6	8.0	199.2	7.1	15.4	197.9	28.9	2.5
22	3.9	8.8	206.1	7.3	8.4	236.7	33.5	1.8
23	4.1	13.2	263.2	10.2	9.5	310.0	46.7	1.0
24	4.1	17.1	332.5	11.7	11.5	209.3	29.9	1.0
25	4.2	11.2	278.9	9.2	13.7	264.3	36.8	1.0
26	4.4	8.8	265.6	9.3	14.5	291.5	41.0	2.5
27	5.1	14.0	264.3	12.0	10.1	257.5	36.2	1.0
28	5.5	13.1	194.8	11.0	14.8	195.0	27.1	1.0
29	5.9	9.6	194.6	8.3	16.2	200.6	29.3	3.3
30	7.3	12.1	211.1	10.7	16.4	268.2	36.7	1.8

Appendix B

Convergence test in WEC-Sim

In WEC-Sim, wave parameters were introduced using the spectrumImport option. Although the software recommends a discretization of 1000 frequency bins, initial test simulations revealed periodic repetition in the wave elevation time series. To address this, a convergence study was conducted to determine the minimum number of frequency bins required to eliminate signal repetition while minimizing computational cost.

The study began with a frequency resolution of $\Delta f = 9 \times 10^{-5}$ Hz, corresponding to one frequency bin per second of simulation time ($1/10800 \approx 9 \times 10^{-5}$). Given the frequency range of interest (0.01–0.8 Hz), this resolution required approximately 9000 bins. As shown in Figure B.1, the resulting wave elevation time series exhibited no visible repetition.

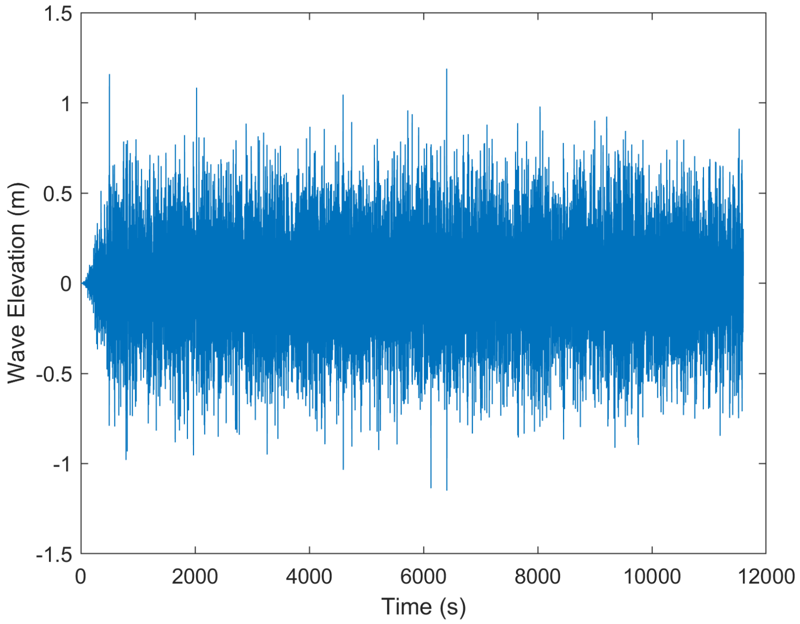

Figure B.1: Wave elevation time for sea state 1 with a discretisation of 9000 bins.

Subsequently, the number of bins was reduced to 4500. As illustrated in Figure B.2, this discretization also produced a non-repetitive signal, indicating that it may be sufficient for accurate simulation.

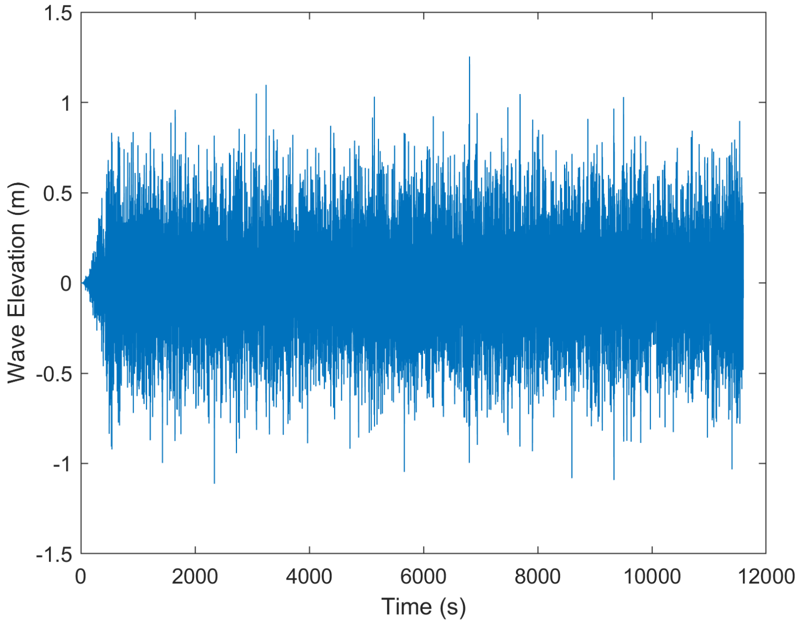

Figure B.2: Wave elevation time for sea state 1 with a discretisation of 4500 bins.

Further reductions to 2500 and 1500 bins were tested to evaluate the lower bounds of acceptable discretization. As shown in Figures B.3 and B.4, both cases exhibited slight repetition in the wave elevation signal, suggesting that these resolutions are insufficient for accurate representation of the wave spectrum.

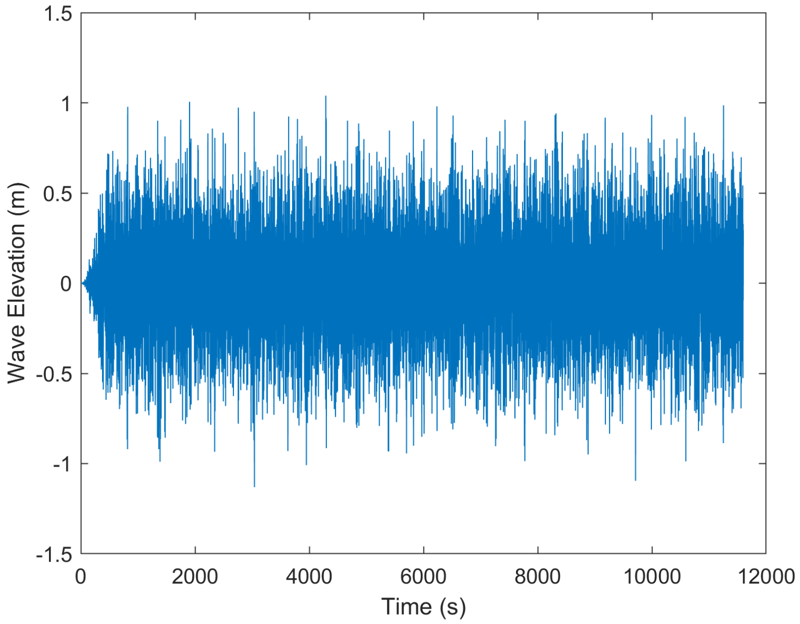

Figure B.3: Wave elevation time for sea state 1 with a discretisation of 2500 bins.

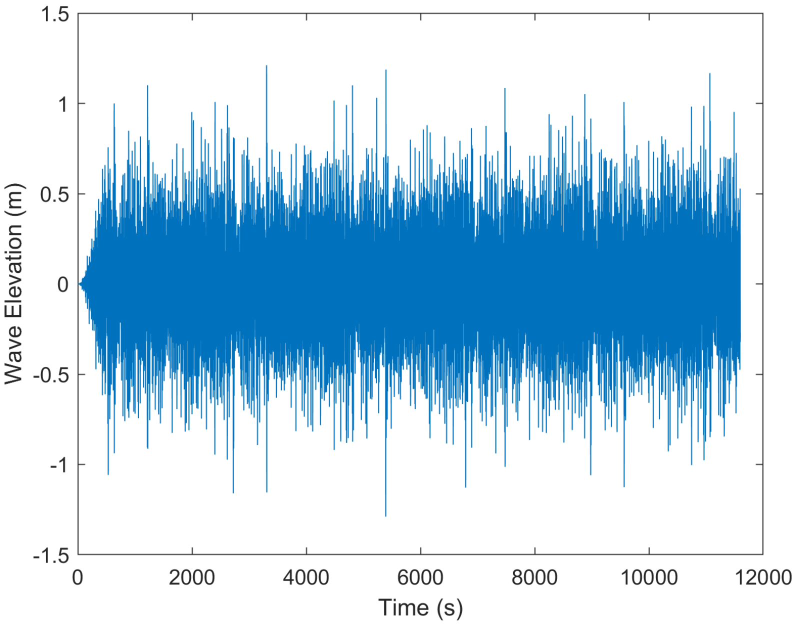

Figure B.4: Wave elevation time for sea state 1 with a discretisation of 1500 bins.

Based on these results, a discretization of 4500 frequency bins was selected as the optimal balance between computational efficiency and signal fidelity.

Appendix C

Wave Field Modelling Results

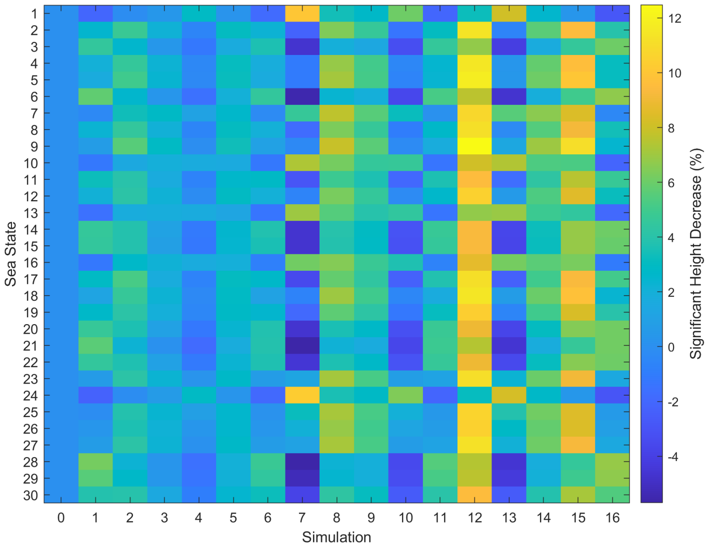

Figure C.1: Heat map of significant wave height decrease for all simulations and sea states.

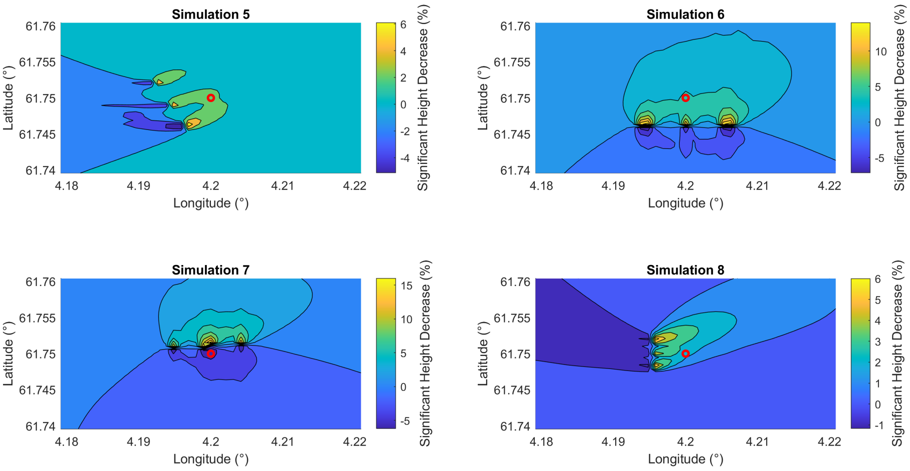

Figure C.2: Significant wave height decrease in simulations 5, 6, 7, and 8.

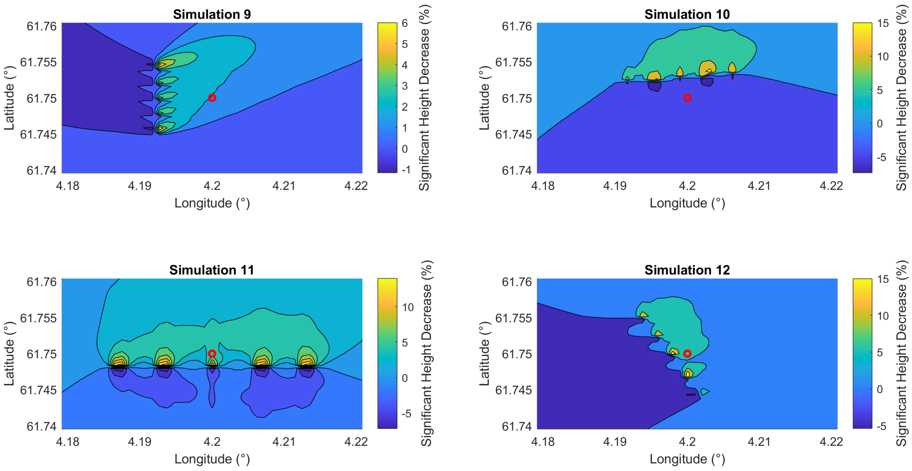

Figure C.3: Significant wave height decrease in simulations 9, 10, 11, and 12.

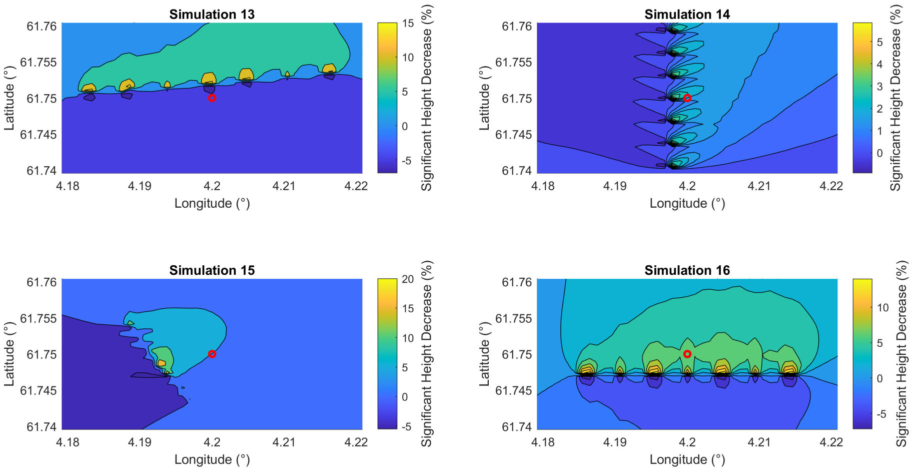

Figure C.4: Significant wave height decrease in simulations 13, 14, 15, and 16.

Appendix D

Motion, Forces and Tension in the FOWTs and Mooring Lines

Table D.1: Standard deviation of Heave, Surge and Pitch in the platform.

Simulation	Heave (m)	Surge (m)	Pitch (m)
1	0.02	0.03	0.0006
2	0.01	0.02	0.0004
3	0.02	0.01	0.0004
4	0.04	0.07	0.0014
5	0.01	0.02	0.0004
6	0.05	0.03	0.0007
7	0.03	0.07	0.0014
8	0.05	0.09	0.0017
9	0.09	0.14	0.0023
10	0.05	0.09	0.0018
11	0.60	0.19	0.0026
12	0.03	0.06	0.0015
13	0.06	0.10	0.0020
14	0.31	0.13	0.0019
15	0.07	0.08	0.0015
16	0.15	0.22	0.0036
17	0.65	0.25	0.0036
18	0.11	0.23	0.0041
19	0.09	0.16	0.0031
20	0.69	0.19	0.0027
21	0.08	0.08	0.0018
22	0.11	0.13	0.0024
23	1.17	0.54	0.0074
24	1.96	0.36	0.0040
25	0.40	0.44	0.0067
26	0.14	0.29	0.0056
27	1.67	0.73	0.0093
28	1.44	0.19	0.0028
29	0.23	0.15	0.0029
30	1.09	0.53	0.0075

Table D.2: Standard deviation of the tension in Cables 1, 2, and 3.

Simulation	Tension Cable 1 (kN)	Tension Cable 2/3 (kN)	Simulation	Tension Cable 1 (kN)	Tension Cable 2/3 (kN)
1	5.9	4.3	16	8.9	4.3
2	3.7	2.3	17	15.4	2.3
3	4.4	3.4	18	16.5	3.4
4	5.6	3.8	19	9.4	3.8
5	7.1	4.4	20	16.6	4.4
6	4.5	3.3	21	12.6	3.3
7	9.9	6.4	22	13.6	6.4
8	5.2	3.8	23	52.0	3.8
9	8.1	5.8	24	78.8	5.8
10	5.2	4.0	25	30.5	4.0
11	11.4	9.5	26	29.9	9.5
12	10.2	6.2	27	97.4	6.2
13	7.9	5.8	28	49.6	5.8
14	8.5	6.7	29	17.7	6.7
15	10.4	7.8	30	49.6	7.8

Appendix E

Fatigue Analysis

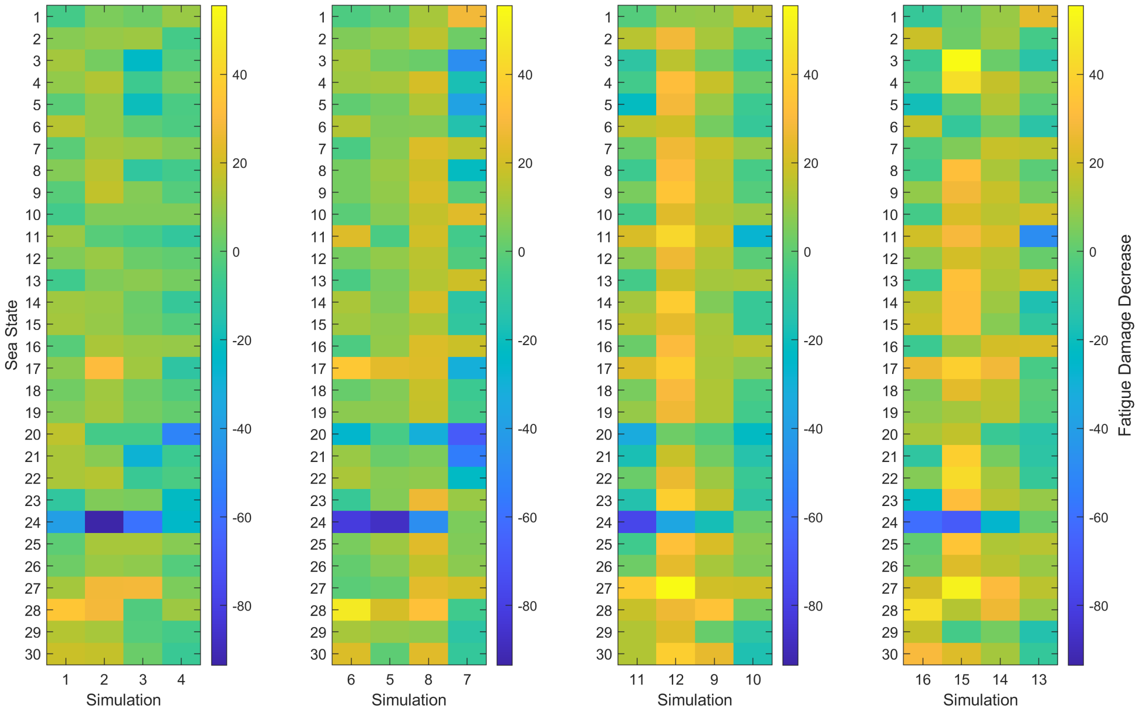

Figure E.1: Heat maps of year fatigue in Cables 2 and 3 grouped by number of WECs — 1, 3, 5, 7 from left to right.

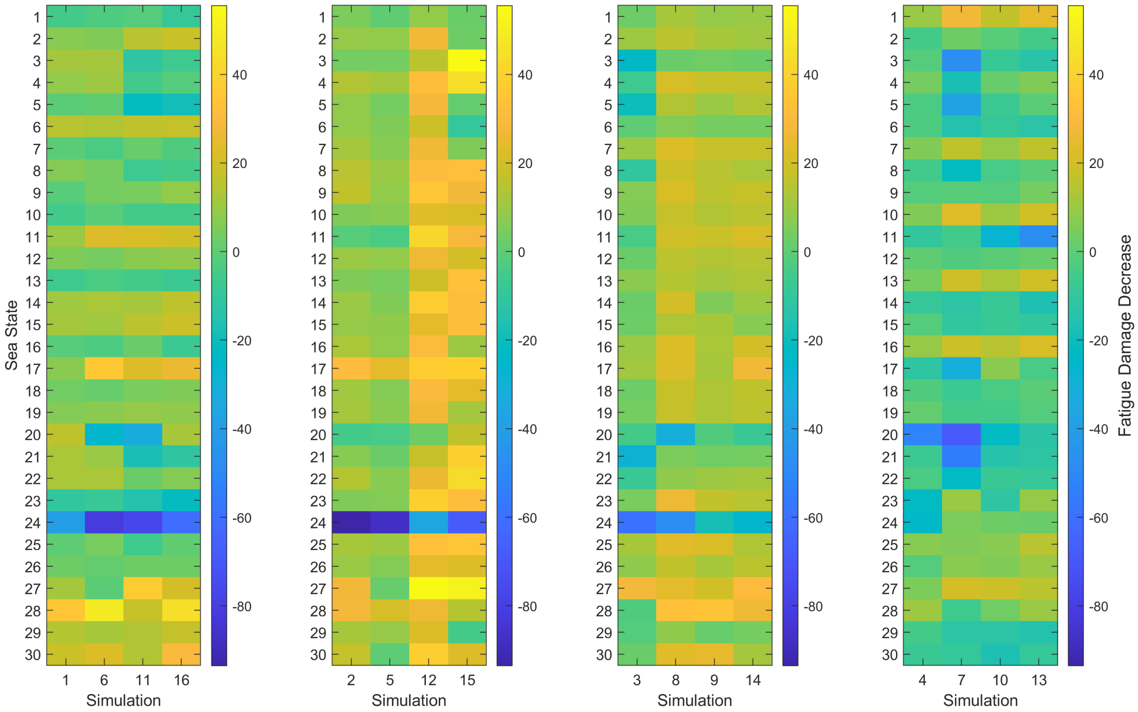

Figure E.2: Heat maps of year fatigue in Cables 2 and 3 grouped by alignment of the WEC array with the FOWT — 180º, 250º, 270º, 350º from left to right.

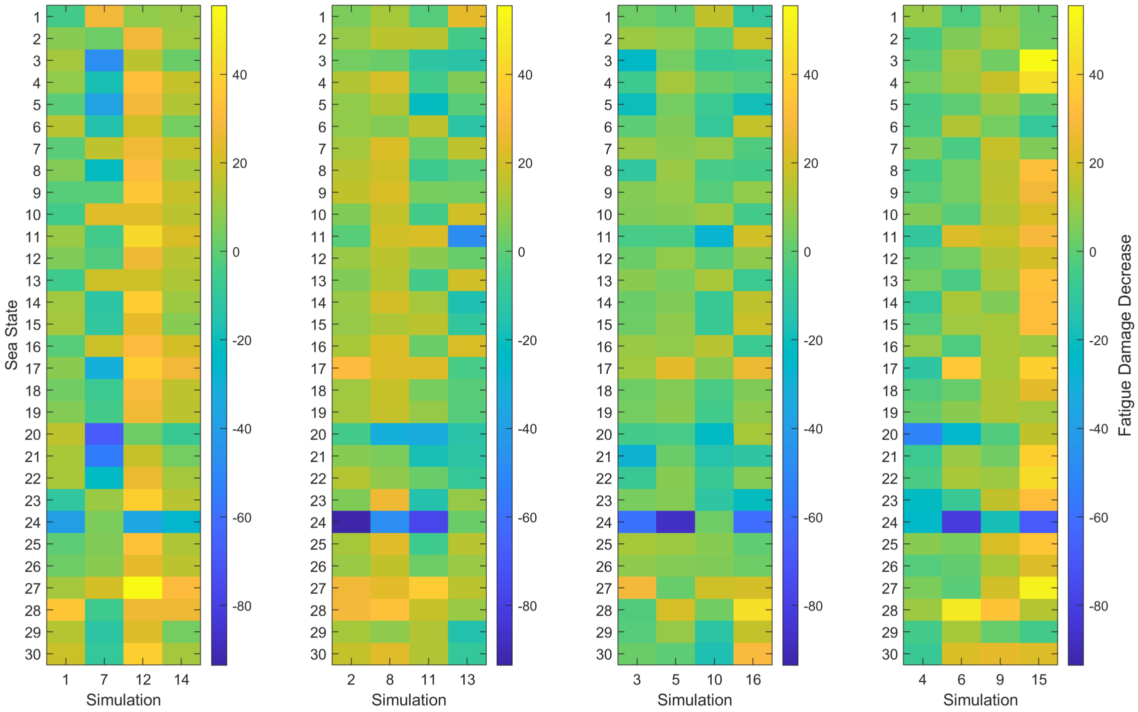

Figure E.3: Heat maps of year fatigue in Cables 2 and 3 grouped by distance between WEC array and FOWT — 120m, 220m, 320m, 420m from left to right.

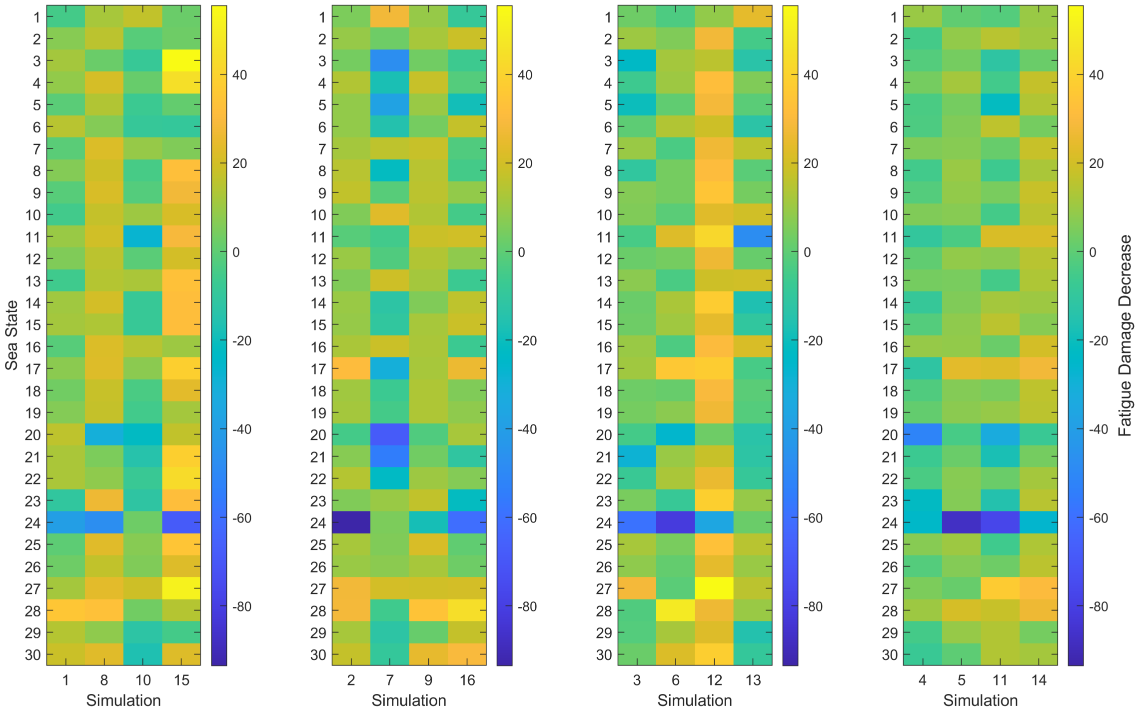

Figure E.4: Heat maps of year fatigue in Cables 2 and 3 grouped by distance between WECs — 198m, 248m, 298m, 348m from left to right.

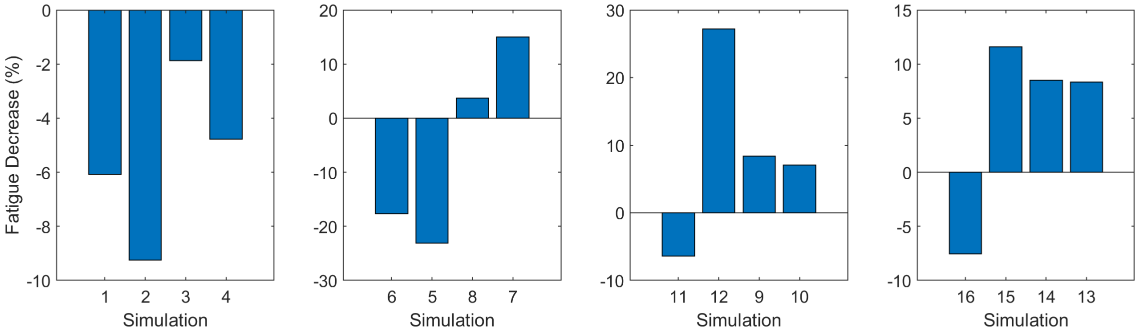

Figure E.5: Total fatigue decrease in Cable 1 grouped by number of WECs — 1, 3, 5, 7 from left to right.

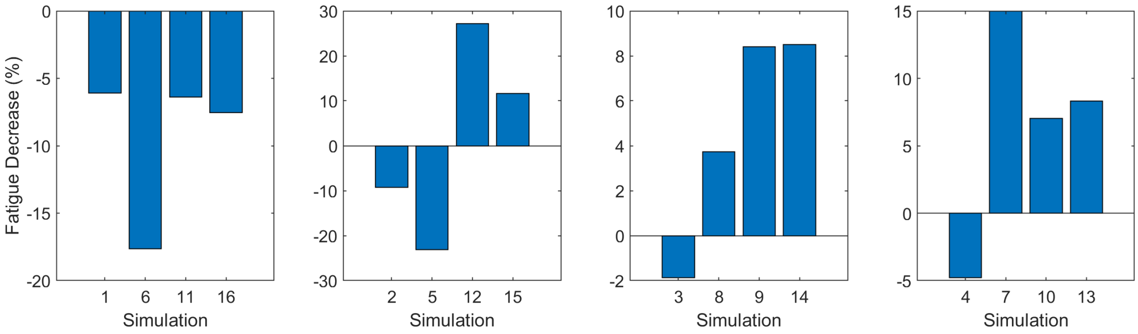

Figure E.6: Total fatigue decrease in Cable 1 grouped by alignment of the WEC array with the FOWT — 180º, 250º, 270º, 350º from left to right.

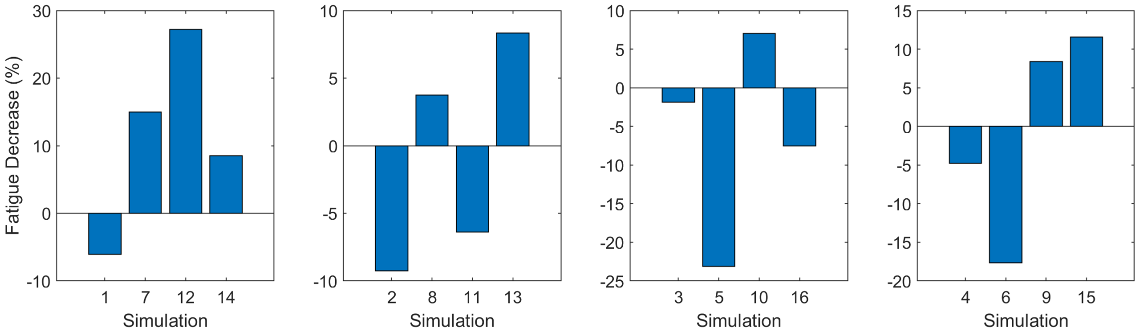

Figure E.7: Total fatigue decrease in Cable 1 grouped by distance between WEC array and FOWT — 120 m, 220 m, 320 m, 420 m from left to right.

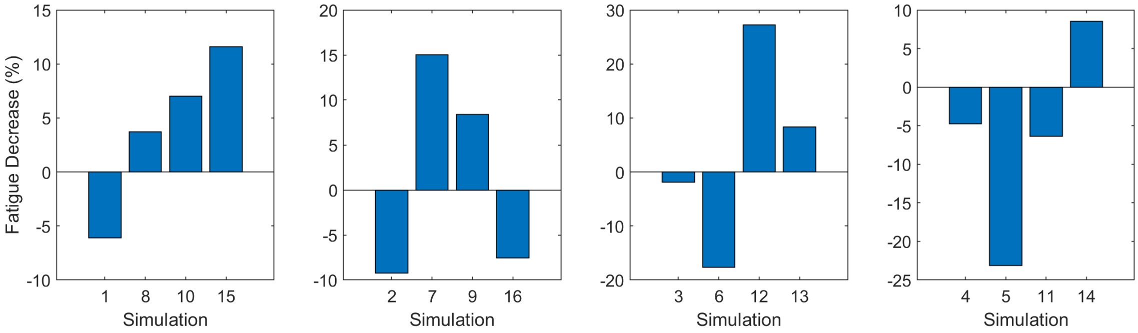

Figure E.8: Total fatigue decrease in Cable 1 grouped by distance between WECs — 198 m, 248 m, 298 m, 348 m from left to right.